The Fibonacci quasicrystal: Case study of hidden dimensions and multifractality

Anuradha Jagannathan

To cite this version:

Anuradha Jagannathan. The Fibonacci quasicrystal: Case study of hidden dimensions and multifractality. Reviews of Modern Physics, 2021, 93 (4), pp.045001. 10.1103/RevModPhys.93.045001 . hal-04064448

HAL Id: hal-04064448
https://hal.science/hal-04064448v1

Submitted on 11 Apr 2023

REVIEWS OF MODERN PHYSICS, VOLUME 93, OCTOBER–DECEMBER 2021

The Fibonacci quasicrystal: Case study of hidden dimensions and multifractality

Anuradha Jagannathan

Laboratoire de Physique des Solides,
Bâtiment 510, Université Paris–Saclay, 91405 Orsay, France

The distinctive electronic properties of quasicrystals stem from their long-range structural order, with invariance under rotations and under discrete scale change, but without translational invariance. d-dimensional quasicrystals can be described in terms of lattices of higher dimension ($D > d$), and many of their properties can be simply derived from analyses that take into account the extra "hidden" dimensions. In particular, as recent theoretical and experimental studies have shown, quasicrystals can have topological properties inherited from the parent crystals. These properties are discussed here for the simplest of quasicrystals, the one-dimensional (1D) Fibonacci chain. The Fibonacci noninteracting tight-binding Hamiltonians are characterized by the multifractality of the spectrum and states, which is manifested in many of its physical properties, most notably in transport. Perturbations due to disorder and reentrance phenomena are described, along with the crossover to strong Anderson localization. Perturbations due to boundary conditions also give information on the spatial and topological electronic properties, as is shown for the superconducting proximity effect. Related models including phonon and mixed Fibonacci models are discussed, as are generalizations to other quasiperiodic chains and higher-dimensional extensions. Interacting quasiperiodic systems and the case for many body localization are discussed. Some experimental realizations of the 1D quasicrystal and their potential applications are described.

DOI: 10.1103/RevModPhys.93.045001

CONTENTS

I. INTRODUCTION TO THE FIBONACCI CHAIN

The Fibonacci chain is a one-dimensional quasiperiodic structure that is closely related to the three-dimensional icosahedral quasicrystals discovered by Shechtman *et al.* (1984). The study of electronic properties of quasicrystals thus logically begins with the study of electrons in a 1D Fibonacci chain. This "fruit fly" of quasiperiodic studies not only is a theoretical construct but also can be experimentally realized in artificial atom chains or in heterostructures made from quasi-2D semiconducting layers, to give two examples. Tight-binding Hamiltonians for the Fibonacci chain have been extensively investigated. Properties of the energy spectra and critical states of the chain have been studied using a variety of methods, exact solutions, perturbation theory, and numerical analysis. Aperiodic Schrödinger operators in general, and quasiperiodic systems in particular, are an active subject of mathematical physics (Damanik, Embree, and Gorodetski, 2015), with a review having been devoted exclusively to the Fibonacci model (Damanik, Gorodetski, and Yessen, 2016).

Quasiperiodic Hamiltonians are of growing interest for their nontrivial topological properties (Verbin *et al.*, 2013; Huang and Liu, 2018, 2019). Like the well-known Aubry-André-Harper (AAH) model, to which it is often compared, the one-dimensional Fibonacci quasicrystal possesses a higher-dimensional "parent" system, from which it inherits topological characteristics. Thus, in the Fibonacci chain there appear to be topologically protected boundary states equivalent to the edge states of the two-dimensional integer quantum Hall effect (Verbin *et al.*, 2015). Unlike the quasiperiodic AAH model, which is critical at a single point in its parameter space, the Fibonacci models that we discuss here are critical for all values of the strength of the quasiperiodic modulation.

Multifractal states are omnipresent in the phase diagram of quasicrystals. Some recent works have given exact solutions for multifractal states in quasicrystals and, in particular, for the $E = 0$ central state of the off-diagonal model (Kalugin and Katz, 2014; Macé *et al.*, 2017). To our knowledge there have not been attempts to solve for arbitrary states on the Fibonacci chain using exact methods along the lines of the Bethe ansatz–based analysis presented by Abanov, Talstra, and Wiegmann (1998) for the quasiperiodic AAH model. Much valuable information can be obtained about the critical wave functions of the Fibonacci chain using a perturbative renormalization group treatment (Macé, Jagannathan, and Piéchon, 2016). Some of the physical manifestations of critical states have been discussed in relation to thermodynamic quantities such as those in interesting proximity effects (Rai, Haas, and Jagannathan, 2019), or in dynamical phenomena including the growth of entanglement (Macé, Laflorencie, and Alet, 2019).

Studies of hyperuniformity in complex systems including quasicrystals and glasses have received significant recent interest as a way to characterize spatial fluctuations in complex structures (Torquato, 2018). The Fibonacci chain, as indeed all quasicrystals, possesses the hyperuniformity property (Baake and Grimm, 2019). This should have consequences for the electronic wave functions since weaker geometric fluctuations can be expected to favor delocalization. The hyperuniformity should thus lead to distinctive spectral characteristics in the Fibonacci chain compared to generic aperiodic chains not having this property.

Some important conceptual, and experimentally pertinent, questions concern the role of perturbations. One can ask what the effects of disorder are in a quasicrystal, and how critical states are affected by randomness. Recent work on disorder and the approach to strong localization in the Fibonacci quasicrystal showed reentrant phenomena and the existence of a new crossover exponent (Jagannathan and Tarzia, 2020). These works concern single-particle properties. Interacting quasiperiodic systems have been considered in a number of studies. In particular, many body localization (MBL) due to quasiperiodic potentials (Iyer *et al.*, 2013) has been an active topic of recent research. One of the questions addressed concerns differences in the critical behavior, if any, from MBL due to random potentials (Khemani, Sheng, and Huse, 2017). It is becoming possible to study a number of models experimentally with cold atoms in optical potentials, possibly extending to realizations of generalized Fibonacci problems (Singh *et al.*, 2015). These could allow a new generation of experimental studies of interacting quasicrystals.

This outline of some of the interesting and not yet fully understood aspects of the Fibonacci model seeks to convince the reader that this "toy model" merits further study by both theory and experiment. This review restricts the discussion to this simplest one-dimensional case, allowing a reasonably detailed description of methods and presenting a state of the art that should be useful to those wishing to work on these or related systems. The outline of the review is as follows: It begins with certain important structural properties of Fibonacci chains included here for completeness, since they are essential for the ensuing discussions of the tight-binding Hamiltonians. Section II focuses on geometrical aspects, introducing useful notations and properties of the Fibonacci chain and its approximants. Section III presents the basic tight-binding models along with the principal spectral properties of the diagonal and off-diagonal Fibonacci models. Some important exact results are introduced in Sec. III, in particular, the well-known gap labeling theorem and an exact renormalization group (the trace map) method. Finally, an exact solution for the multifractal wave function in the diagonal model for $E = 0$ is given. Section IV takes up approximate methods that have proven to be extremely useful, yielding many valuable insights into spectral and wave-function properties. In particular, the section introduces the perturbative renormalization group technique and its qualitative predictions. Section V takes up the off-diagonal model in more detail in order to illustrate the use of the perturbative renormalization group (RG) technique in obtaining a quantitative description of spectrum and critical wave functions. Section VI is a first step in discussing physical observables. It introduces wave packet dynamics, time dependence of the correlation function, and log-periodic behavior. Section VII presents results for transmission coefficient and chain conductances using the Landauer formalism and the Kubo-Greenwood approach. Section VIII discusses effects due to disorder in the Fibonacci chain (FC) and describes reentrant phenomena and crossover to strong Anderson localization. The role of boundary conditions and the proximity effect when the FC is coupled to a superconductor are described. Section IX presents important generalizations of the simple models hitherto considered, including phonon modes on the Fibonacci chain. The so-called mixed models that combine diagonal and off-diagonal quasiperiodic modulations are discussed in the section. Section X outlines a few other frequently encountered 1D quasiperiodic systems related to the Fibonacci chain. The section also describes some extensions to higher dimensions. Section XI lists results for interacting quasiperiodic systems. Finally, Sec. XII gives some examples of experimental realizations of Fibonacci models in electronic, cold atom, phononic, and photonic systems. Section XIII concludes the review with a summary and outlook.

II. GEOMETRIC PROPERTIES OF THE FIBONACCI CHAIN

The Fibonacci chain is a 1D quasicrystal, according to the revised definition of the International Union of Crystallography (1992). The definition states that a quasicrystal, like a periodic crystal, is a material having a sharp diffraction pattern composed of Bragg peaks. The indexing of peaks proceeds as it does for crystals; however, it requires a set of D reciprocal lattice vectors where D is larger than the spatial dimension d. This distinguishes the quasicrystal from a periodic lattice, where the number of reciprocal lattice vectors is equal to d. This section describes how to generate the Fibonacci chain and reviews some of its geometrical and structural properties. We introduce several methods, each of which is helpful in its own way for a better understanding of electronic properties in this system.

A. Substitution method

The substitution method explicitly introduces the notion of scale invariance of the quasicrystal, which is later used in the renormalization group transformation. The Fibonacci substitution rule σ acts on the two letters A and B and transforms them as follows:

$$\sigma\colon \begin{cases} A \to AB, \\ B \to A. \end{cases} \tag{1}$$

Letting the substitution act repeatedly on the letter B generates a sequence of words $C_n = \sigma^n(B)$ of increasing length, as shown for the first few members in Table I. These chains are finite approximants of the Fibonacci chain, which is obtained in the limit $n \to \infty$. It is clear that the lengths of the words are equal to the Fibonacci numbers F_n, which are defined by the recursion relation $F_n = F_{n-1} + F_{n-2}$ with $F_0 = F_1 = 1$. The following ratio of two consecutive Fibonacci numbers tends to the golden mean as $n \to \infty$:

$$\frac{F_{n-1}}{F_{n-2}} = \tau_n, \qquad \lim_{n\to\infty} \tau_n = \tau, \tag{2}$$

where τ_n are the rational approximants of the golden mean $\tau = (1+\sqrt{5})/2$. The lengths of the chains are given by $F_n \sim \tau^n$ in the large n limit.

TABLE I. The first six approximants built using the substitution σ [defined in Eq. (1)].

n	C_n	F_n
0	B	1
1	A	1
2	AB	2
3	ABA	3
4	ABAAB	5
5	ABAABABA	8
6	ABAABABAABAAB	13

Inflation and deflation of tiles.—The substitution method shows the hierarchical relations between the chains and suggests that problems on the chain could be tackled using renormalization group methods. Consider a 1D tiling of A and B tiles such that the ratio of their lengths $l_A/l_B = \tau$. The approximant chains C_n correspond to a series of finite tilings that can be transformed into one another by so-called inflation and deflation operations. Using the substitution (1) in reverse, one goes from a chain of F_n tiles to a chain of F_{n-1} tiles. Note that this corresponds to a "site decimation" process that eliminates a certain subset of sites. Rescaling all the tiles by a factor of τ_n restores the length of the chain to its original value, as illustrated in Fig. 1. The infinite chain is invariant under inflation and deflation: i.e., the FC has a discrete scale invariance.

Concatenation.—From Fig. 1 (and Table I) one sees that the nth chain C_n can be obtained by the concatenation of two shorter chains C_{n-1} and C_{n-2}. This property is useful later for the transfer matrix method (Sec. III.D). Repeating this operation, one obtains a relation between the nth chain and the $(n-2)$th and $(n-3)$th chains as follows:

$$C_n = C_{n-2} \oplus C_{n-3} \oplus C_{n-2}, \tag{3}$$

where the circled plus sign denotes concatenation (joining the chains in the specified order from left to right). This recursive construction also holds for the energy spectrum in perturbative RG, as we see in Sec. V.

Inflation matrix.—Let $N_A^{(n)}$ and $N_B^{(n)}$ be the number of occurrences of A and B in an approximant chain C_n. From the substitution rule given in Eq. (1), it is clear that $N_A^{(n+1)} = N_A^{(n)} + N_B^{(n)}$ and $N_B^{(n+1)} = N_A^{(n)}$, with the initial condition $N_A^{(0)} = 0$ and $N_B^{(0)} = 1$. This relation can be put in the following matrix form:

$$\begin{bmatrix} N_A^{(n+1)} \\ N_B^{(n+1)} \end{bmatrix} = \begin{bmatrix} 1 & 1 \\ 1 & 0 \end{bmatrix} \begin{bmatrix} N_A^{(n)} \\ N_B^{(n)} \end{bmatrix}, \tag{4}$$

FIG. 1. Illustration of inflation transformations progressing from the C_5 (top panel) to the C_4 (middle panel) to the C_3 (bottom panel) chain. A (B) tiles are shown as gray (black) rectangles.

where the 2×2 matrix is called the substitution matrix M. The eigenvalues of M are $\lambda_1 = \tau$ and $\lambda_2 = -\tau^{-1}$. The corresponding eigenvectors are $\{\tau, 1\}$ and $\{1, -\tau\}$. The first eigenvector gives the relative frequencies of the A and B tiles by virtue of the Perron-Frobenius theorem. The ratio N_A/N_B tends to τ when $n \to \infty$. For more details on symbolic substitutions, see Baake and Grimm (2013).

At this point, we make a digression relating to other types of binary chains generated by the substitution method. Two different classes of problems arise, as exemplified below.

(1) The so-called silver mean chain can be obtained from repeated application of the following rule:

$$\sigma_{\mathrm{Ag}}: \begin{cases} A \to AAB, \\ B \to A. \end{cases} \tag{5}$$

One can easily check to see, by writing the inflation matrix for this case, that the eigenvalues satisfy the equation $\lambda^2 - 2\lambda - 1 = 0$. The Perron-Frobenius eigenvalue in this case is $\lambda_1 = (\sqrt{2} + 1)$. This type of rule can be generalized to yield a series of so-called metallic mean chains having the substitution rule $B \to A, A \to A^n B$ $(n \geq 1)$. Note that number theoretic properties enter crucially in aperiodic systems and lead to significantly different spatial and physical characteristics. Both the Fibonacci chain and the silver mean chain are based on irrational numbers that are Pisot numbers (a Pisot number is the root α of an nth degree monic polynomial equation with integer coefficients such that α is greater than 1, while all other roots are of a modulus less than 1).

(2) Next consider the substitution rule $B \to A, A \to ABBB$, which gives rise to a self-similar aperiodic structure that is, however, not a quasicrystal. This structure is non-Pisot: it can be checked to ensure that the two eigenvalues of the inflation $\lambda = (1 \pm \sqrt{13})/2$, which are both greater than 1 in absolute value. The spatial properties of this chain are significantly different than those of the golden and silver mean quasicrystals. In particular, the diffraction pattern of such a chain does not have Bragg peaks (Baake *et al.*, 2019), as we now explain by considering the nature of geometric fluctuations.

Fluctuations of geometry.—Consider a subsystem of N letters from the infinite Fibonacci chain. For values of N that are not Fibonacci numbers the number of A's and B's in the sample $\delta_N = N_A - N_B$ fluctuates around the mean value $\bar{\delta}$. The behavior of δ_N for large N is described in terms of η, the so-called wandering exponent defined (Luck, 1993) for a one-dimensional chain as

$$\delta_N - \bar{\delta} \sim N^{\eta}. \tag{6}$$

In periodic systems, fluctuations are subextensive (i.e., due to boundary effects) and $\eta = 0$. Fluctuations are similarly negligible in the thermodynamic limit for Pisot aperiodic chains, including the Fibonacci chain. For these structures $\eta = 0$, and as a consequence their diffraction spectrum is pure point; i.e., it consists solely of Bragg peaks (Godrèche and Luck, 1992).[1]

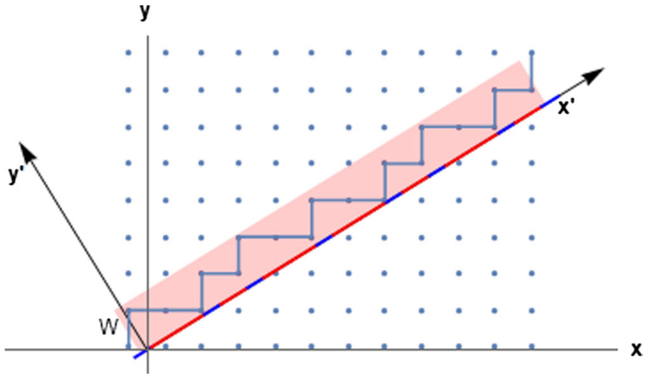

FIG. 2. Schema of the cut-and-project method. Selected points (joined by a broken line) of a 2D square lattice are projected onto the x' axis, giving the binary quasiperiodic sequence of short red (light gray) and long blue (dark gray) tiles. The infinite selection strip $\mathcal{S}$ is colored red (gray).

It is instructive to compare this with geometry fluctuations in random systems. Consider a random sequence of the letters A and B for some fixed probabilities p_{A} and $p_B = 1 - p_A$ of the letters. The law of large numbers leads to the exponent $\eta = 1/2$ in this case. The huge fluctuations, divergent in the thermodynamic limit, reflect the fact that there are rare regions in which the number of A's (for example) vastly exceeds the number of B's. For non-Pisot systems such as the "3B" aperiodic structure defined earlier, fluctuations diverge with the system size and the wandering exponent is given by $\eta = \ln|\lambda_2|/\ln\lambda_1$ (Godrèche and Luck, 1992; Luck, 1993).

This property of bounded geometrical fluctuations of the quasicrystal is the principal reason for electronic states in quasicrystals being relatively more extended than, for example, the critical states at the metal-insulator transition in disordered structures. This is also related to the hyperuniformity property, which is discussed in Sec. II.B.2.

B. Higher-dimensional representation of the FC

Quasicrystals can be generated by projection from a higher-dimensional periodic lattice by the cut-and-project method, as we illustrate here for the case of the Fibonacci chain.

1. Cut-and-project method

The parent system is a 2D square lattice, and the quasicrystal is obtained by projection onto the physical axis labeled x' in Fig. 2. To be selected, a point must lie within the red strip $\mathcal{S}$ of the slope given by

$$\tan\theta = \omega, \tag{7}$$

where the notation $\omega = 1/\tau = (\sqrt{5} - 1)/2$ is introduced for convenience. The width of the strip is chosen to span one unit

---

[1] This result holds as well in higher dimensions of deterministic tilings such as the well-known Penrose 2D and 3D tilings, the Ammann-Beenker tiling, etc.

cell of the 2D lattice. Upon projection onto the x' axis (the physical axis), horizontal bonds and vertical bonds project onto the red and blue intervals, respectively. The y' axis is called the perpendicular (or internal) space.

Expressing all lengths in units of the square lattice parameter a, vertices of the square lattice are located at $\vec{R}_{mn} = m\vec{x} + n\vec{y}$, where m and n are integers. The x' coordinate and the coordinate along the perpendicular direction y' are given by

$$\begin{aligned} x' &= m\cos\theta + n\sin\theta, \\ y' &= -m\sin\theta + n\cos\theta, \end{aligned} \tag{8}$$

up to an overall shift. To be selected, the point must satisfy the condition $0 \le y' < W$, where $W = \sin\theta + \cos\theta$ is the cross section of the strip $\mathcal{S}$.

After projection on the x' axis, the spacing between nearest neighbors can have two values, $\cos\theta = 1/\sqrt{1+\omega^2}$ or $\sin\theta = \omega/\sqrt{1+\omega^2}$, corresponding to the lengths of the A and B tiles of Sec. II.A.

Translational symmetries.—The origin of the $x'y'$ axes is arbitrary: i.e., shifting the strip perpendicularly to itself does not result in a new quasiperiodic structure. This statement requires a clarification of what is meant by equivalence between quasiperiodic tilings. Tilings are said to be equivalent (or locally isomorphic) if the same sequences of tiles (which may be of an arbitrarily large size) can be found in both structures, and with the same frequency of occurrence. In other words, one can make the two tilings overlap out to arbitrarily large distances by suitably translating one with respect to the other.

The higher-dimensional representation of the FC shows that the structure has a translational symmetry with respect to displacements parallel to the physical space, but also in the perpendicular direction. This leads theoretically to the possibility of having two kinds of Goldstone modes: phonons and phasons. Phonons are 1D vibrational modes in the usual sense. To visualize phason modes, see Fig. 3, which shows how the projected structure would change if the lattice were to be slightly displaced in the direction perpendicular to the strip. The vertex (m, n) in the figure moves out of the strip while, simultaneously, the vertex $(m-1, n+1)$ enters the strip. The net result is a small discontinuous jump of one site, while the other points in its neighborhood remain unaffected. This so-called phason jump corresponds to exchanging the A and B tiles around a given vertex AB → BA. The shift produces a new chain structure which is equivalent to the old one. In accepted terminology, a phason mode is a coherent excitation of the perfect Fibonacci chains corresponding to long wavelength fluctuations. In contrast, when phason flips are introduced in a random uncorrelated fashion all along a chain, this gives rise to a geometrically disordered chain. In practice, however, spontaneous phason flips presumably have a significant energy cost and are unlikely to be excited at low temperatures.

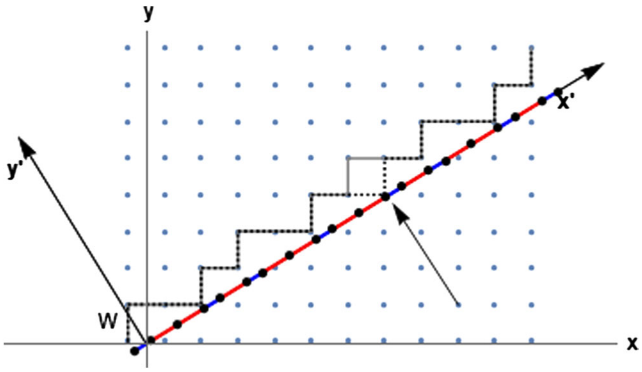

FIG. 3. Illustration of a phason flip or local rearrangement of the tiling when the lattice is slightly displaced with respect to the selection strip. The old (new) tilings are obtained by projecting the solid (dashed) lines. The arrow shows the location of the phason flip where a long-short tile ordering has become an short-long ordering.

Approximants.—Periodic approximants of the FC are generated by taking a rational slope for the strip S. If the slope is chosen to be the ratio of two successive Fibonacci numbers

$$\tan\theta_n = F_{n-2}/F_{n-1},$$

then the projected chain has a repeating structure consisting of F_{n-1} and F_{n-2} tiles of type A and B, respectively, and the total number of tiles is F_n. It is easy to ensure that one obtains the same approximant sequences already seen in Table I. For example, for $n = 3$ the strip has a slope equal to $1/2$ and one obtains a periodic repetition of the motif ABA.

2. Structure factor

As previously mentioned, the defining characteristic of a quasicrystal is that it has a pure point diffraction pattern, i.e., Dirac delta-function peaks of the structure factor. The peaks of the structure factor of the FC occur for q vectors given by linear combinations of two reciprocal lattice vectors.

It is clear that the structure factor of the perfect FC has only Bragg peaks in the higher-dimensional representation. The position of the peaks of the structure factor of the FC can be easily deduced from those of the square lattice. The reciprocal space of the square lattice is given by $\vec{G}_{hk} = 2\pi(h\vec{x} + k\vec{y})$. There are Bragg peaks of $S(q)$ (q is the reciprocal space coordinate) corresponding to each of the $\vec{G}_{hk}$. Projecting each of the points onto the q axis, one sees that all Bragg peak positions q are indexed by two integers h and k:

$$q = q(h,k) = 2\pi(h\cos\theta + k\sin\theta) = g(h + \omega k), \tag{9}$$

where $g = 2\pi/\sqrt{1+\omega^2}$. That is, there are Bragg peaks at positions given by all the integer linear combinations of two incommensurate wave vectors g and ωg.

Figure 4(a) shows some of the positions obtained by projecting the vertices of the reciprocal space lattice (shown in black) onto the q axis. In Eq. (9) note that h and k can take all possible integer values, which results in a dense distribution of peaks of the structure factor along the q axis. In practice, however, the observable peaks of the structure factor are far fewer, as most of the peaks have intensities that are too small to observe. This occurs because the intensities of the

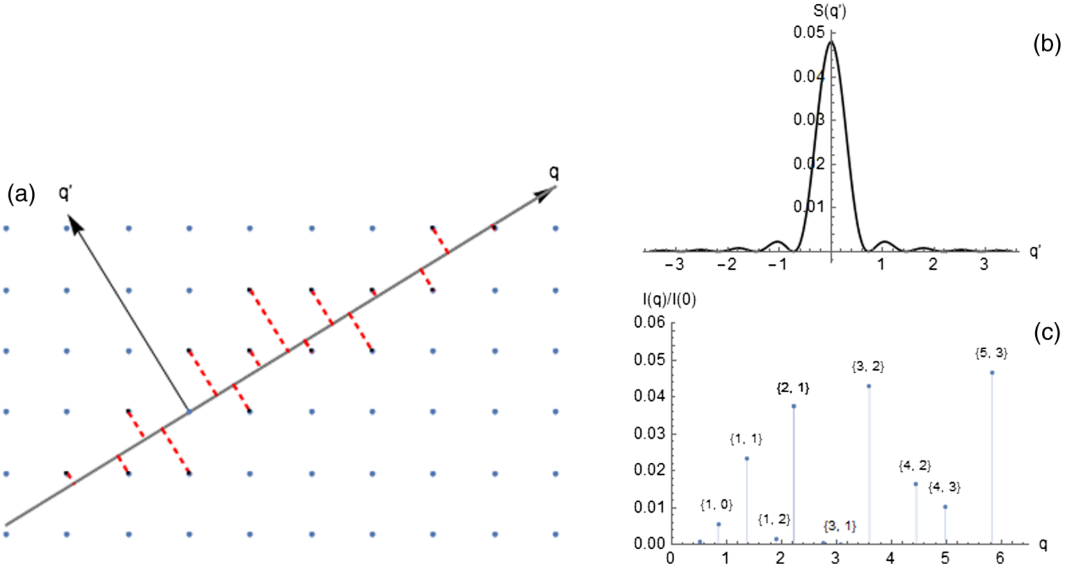

FIG. 4. (a) Reciprocal lattice of the square lattice showing the (q_x, q_y) and (q, q') axes and the projections of some representative points. (b) The form factor corresponding to the selection strip. (c) Relative intensities of the first few peaks for $q > 0$ corresponding to the points outlined in bold in (a). All q values are shown in units of $2\pi/a$.

peaks depend on a form factor, namely, the Fourier transform of the selection strip. The strip is described by the function $\mathcal{S}(y') = 1$ for $0 \le y' \le W$, and $\mathcal{S}(y') = 0$ elsewhere. As a result, peak intensities are modulated by the function

$$|\mathcal{S}(q')|^2 \propto \frac{\sin^2(Wq'/2)}{q'^2}, \tag{10}$$

where the perpendicular reciprocal space coordinate is defined by $q' = (2\pi/a)(-h\sin\theta + k\cos\theta)$. The $\mathcal{S}$ function is akin to the Airy function for diffraction through a slit in optics and is shown in Fig. 4(b). The resulting variation of the peak intensities of the FC is shown in Fig. 4(c).

To conclude this description of the structure factor, we point out one noteworthy characteristic of the FC related to the small q (large wavelength) behavior of $S(q)$. Notice that the Bragg peak intensities near the origin must correspond to large values of the perpendicular component q', and therefore have vanishingly small intensities due to Eq. (9). Excluding the peak at $q = 0$ for forward scattering, one concludes that the structure factor must tend to zero for small q: $\lim_{q\to 0} S(q) \to 0$. For a detailed discussion of this property see Baake and Grimm (2019). Structures with this property are said to be hyperuniform (Torquato, 2018). This is another way of expressing the fact that for the FC (as indeed for all quasicrystals, as previously mentioned) the spatial fluctuations are bounded. As counterexamples of chains not possessing this property one can mention binary 1D structures obtained for non-Pisot substitution rules (Godrèche and Luck, 1992). For a discussion of diffraction patterns of aperiodic systems from a mathematical perspective, see Baake and Grimm (2013).

On patterns and their probabilities.—The cut-and-project method provides a convenient way to compute the probability of a given pattern occurring in the FC. These probabilities are proportional to the length of a corresponding "acceptance zone" in perpendicular space. To illustrate the method, consider the probability of occurrence of a one-letter pattern: the B tile. To be selected, the corresponding vertical bond of the projected length $\cos\theta$ must lie within the window. The acceptance zone is $W - \cos\theta = \sin\theta$, and the probability of B is $\sin\theta/W$. The probability of finding an A tile is proportional, using a similar argument, to $\cos\theta/W$. The ratio of the probabilities is $p(A)/p(B) = \cot\theta = \tau$, as expected.

Consider a two-letter pattern such as AA. This pattern corresponds, in the 2D square lattice, to two consecutive horizontal bonds sandwiched between two vertical bonds. The probability of the pattern AA is given by $(\cos\theta - \sin\theta)/W \approx 0.238$. The configurations AB and BA have equal probabilities of ≈ 0.382.

3. Conumbering scheme

Sire and Mosseri (1990) showed that in approximant chains it can be advantageous to work with an alternative ordering of sites, rather than the usual real space ordering $i = 1, \ldots, N$. The so-called conumber of the site i depends on its perpendicular space coordinate, i.e., the distance along the y' axis. This is illustrated in Fig. 5 for a periodic approximant of 13 sites. The conumbers are given by $c(i) = \mathrm{mod}[i \pm F_{n-2}, F_n]$ up to a global cyclic permutation.

This numbering orders the sites according to their local environments as follows:

- Sites with conumbers $1 < c < F_{n-2}$ have an B tile to the left and an A tile to their right.
- Sites with $F_{n-2} + 1 < c < F_{n-1}$ have A tiles both on the left and on the right.
- The remaining F_{n-2} sites have an A tile to the left and a B tile to their right.

As we saw in Sec. II.A the FC is a self-similar structure. Its inflation symmetry is coded using a hierarchical structure of the conumbering indices. Each of the previously listed three groups of sites is, in turn, composed of three subgroups having

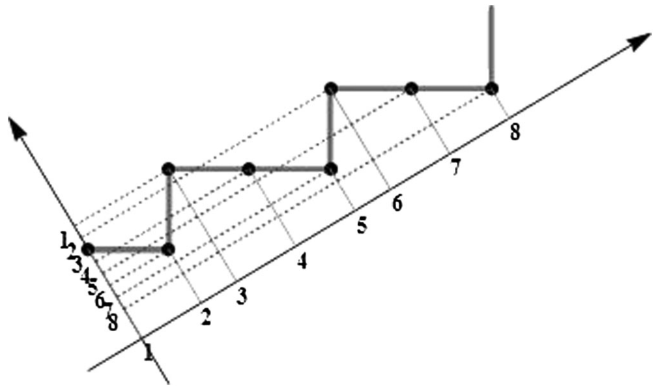

FIG. 5. The $n = 5$ ($N = 8$) approximant showing the real space labels of sites (along the chain) as well as their alternative labeling using their conumbers (along the axis perpendicular to the chain).

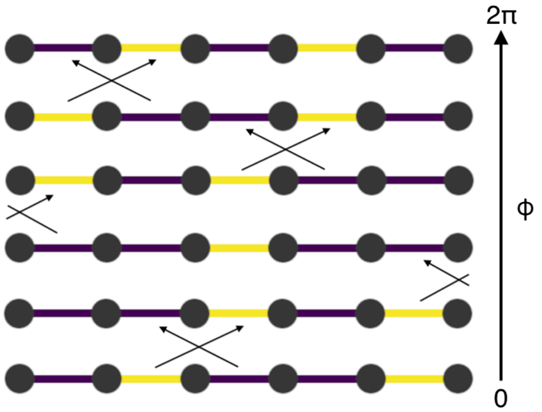

FIG. 6. Successive phason flips in the $n = 4$ approximant ($N = 5$; the first and last sites are equivalent under a translation) as ϕ is varied in Eq. (11).

the same properties but on a larger length scale. In particular, consider the central site, according to the conumber scheme, for an approximant for which n is a multiple of 3. This site always has the same local environment (A tiles on both sides) under inflation of $n \to n - 3$, all the way down to $n = 1$. The conumbering scheme will be useful in Sec. V for a compact representation of the spectrum and states of the hopping model.

We have discussed the cut-and-project method to obtain the FC by projection from a two-dimensional lattice. More generally, projections from higher-dimensional lattices can yield Fibonacci chains as part of higher-dimensional quasiperiodic structures. For example, 2D planes composed of parallel FC can be found in certain three-dimensional structures generated by cut-and-projection from a 4D lattice (Ben-Abraham and Quandt, 2007). In those examples the projections involve the golden mean τ, which is intimately linked to the Fibonacci sequence. The well-known 3D icosahedral tilings also depend on the golden mean, which is why Fibonacci modulation of atomic density can be seen in experimental studies of surfaces of 3D icosahedral quasicrystals, as seen in Fig. 45, taken from Ledieu *et al.* (2004).

C. The characteristic function method

The Fibonacci quasicrystal corresponds to a special case of the family of Sturmian potentials defined by $V(n) = \chi_{[1-\omega,1)}(n\omega + \varphi \bmod 1)$, where φ is an arbitrary phase. Here the characteristic function χ, say, 1 and 0. The value 1, corresponding to the letter A, is obtained when the argument lies in the interval $[1 - \alpha, 1)$, and the value 0, corresponding to the letter B, is obtained otherwise.[2] The characteristic function can, for example, be written explicitly as $\chi_j = 2\{[(j+1)\omega] - [j\omega]\} - 1$, where $[X]$ stands for the integer part of X. In this formulation $\chi_j = -1$ stands for A and $\chi_j = 1$ represents B. The preceding form was modified to an alternative form using a cosine function by Kraus and Zilberberg (2012) as a way to connect the Fibonacci and AAH models. The jth letter of the Fibonacci chain is obtained via the characteristic function χ_j defined by

$$\chi_j = \mathrm{sgn}[\cos(2\pi j\omega + \varphi) - \cos(\pi\omega)], \tag{11}$$

where φ is an arbitrary constant that one can term a phason angle. This function also serves to generate approximants by using a rational approximant of the golden mean in Eq. (39). The approximants C_n defined earlier are found by making suitable choices of $0 \leq \varphi < 2\pi$. The important feature to note is that, when the angle φ is varied, phason flips occur (a single flip at a time). In this way, one can generate a family of F_{n+1} chains of length F_n, corresponding to different values of φ (see Fig. 6). The phason angle will later become a tuning parameter to control the edge modes in open finite approximant chains.

III. TIGHT-BINDING MODELS: EXACT RESULTS

Much of the extensive literature on electronic properties of the FC is devoted to the study of tight-binding models of the form

$$H = \sum_n \epsilon_n c_n^\dagger c_n - (t_n c_{n+1}^\dagger c_n + \mathrm{H.c.}), \tag{12}$$

where ϵ_n represent the site energy at the nth site, while t_n is the hopping amplitude between the sites n and $n + 1$. We assume that these parameters are defined by local rules, i.e., that the values depend on the environment of each site. The first papers on this family of Hamiltonians appeared shortly before the discovery of quasicrystals (Kohmoto, Kadanoff, and Tang, 1983; Ostlund *et al.*, 1983) and were followed by many other groundbreaking papers in the next few years (Kohmoto and Oono, 1984; Ostlund and Pandit, 1984; Kalugin, Kitaev, and Levitov, 1986; Tang and Kohmoto, 1986; Evangelou, 1987; Kohmoto, Sutherland, and Tang, 1987; Sutherland and Kohmoto, 1987; Luck, 1989). When written for approximant chains with periodic boundary

---

[2] More generally, Sturmian potentials can be written in terms of two parameters α and an interval Δ. For generic values of these, it has been shown that the resulting model is not integrable and has large unbounded fluctuations, in contrast to the Fibonacci chain (Godrèche, 1990).

conditions, the Hamiltonian (12) is invariant with respect to translations of the selection strip in the 2D space (Sec. II.B).

A. Diagonal and off-diagonal Fibonacci models

The Hamiltonian of Eq. (12) is termed mixed, as there can be spatial modulations in both diagonal and off-diagonal terms. However, the following simple cases contain all the essential new physics:

(1) *Off-diagonal case*.—Site energies are assumed to be constant, i.e., $\epsilon_n = \epsilon$, while the hopping amplitudes t_n can take the value t_A or t_B, according to a Fibonacci sequence. This is also referred to as the pure-hopping Fibonacci Hamiltonian since the constant energy term can be dropped by using the following suitable redefinition of the energy:

$$H = -\sum_n t_n c^\dagger_{n+1} c_n + \mathrm{H.c.} \tag{13}$$

Absorbing t_B into the definition of the units of energy leaves as a sole parameter the ratio $\rho = t_A/t_B$, which controls all the properties of the chain. Without loss of generality, we henceforth assume both amplitudes to be positive since these signs can be changed by a gauge transformation.

(2) *Diagonal case*.—Here the quasiperiodicity is assumed to be present in the diagonal term, while the hopping amplitudes are assumed to be uniform ($t_{n,n+1} = t$) for all values of n:

$$H = \sum_n \epsilon_n c^\dagger_n c_n - t\sum_n c^\dagger_{n+1} c_n + \mathrm{H.c.}, \tag{14}$$

where the on-site potentials ϵ_n take on two discrete values ϵ_A and ϵ_B according to a Fibonacci sequence. As in model (1), there is only one nontrivial parameter in this model, and it depends on the energy difference $\varepsilon = (\epsilon_A - \epsilon_B)/t$.

The previous models are often compared to those of a particular quasiperiodic Aubry-André-Harper model (Harper, 1955; Aubry and André, 1980; Gordon *et al.*, 1997) hereafter simply called the AAH model. The AAH model is equivalent to a tight-binding problem of an electron hopping in a 2D square lattice and subjected to a uniform magnetic field, with a flux per plaquette $\Phi = \omega\Phi_0$, where $\Phi_0 = h/2e$ is the flux quantum. The resulting quasiperiodic AAH Hamiltonian is of the form

$$H = \sum_n t(c^\dagger_{n+1} c_n + \mathrm{H.c.}) + 2V\cos(2\pi n\omega + \phi) c^\dagger_n c_n, \tag{15}$$

where the strength of the on-site potential energy $2V$ depends on the hopping amplitude along the direction transverse to the chain and ϕ is a phase. A well-known duality transformation takes Eq. (15) into a Hamiltonian of the same form but with the exchange $t \leftrightarrow V$. When $V = t$ the model is self-dual. This is the critical AAH model since it has many properties in common with the Fibonacci model, as described next.

B. Multifractal energy spectra

Spectra can be classified into three types: continuous spectra associated with extended states (as in periodic solids), pure point spectra associated with localized states (as in disordered solids), and singular continuous spectra associated with multifractal states. If one defines the scaling of the integrated density of states $N(E)$ (defined as the fraction of states of energy equal to or less than E) in the vicinity of the energy E by

$$N(E + \Delta E) - N(E) \sim \Delta E^\alpha, \tag{16}$$

then the three cases correspond to $\alpha = 1$, $\alpha = 0$, and $0 < \alpha < 1$. The wave functions typically associated with the last type of fractal spectrum are "critical" states: neither extended nor localized. This intermediate type of state appears to be rather generically found in quasiperiodic structures not only in 1D but in higher dimensions as well, as can be seen in the review of quasiperiodic tight-binding Hamiltonians by Grimm and Schreiber (2003).

For the AAH model, the nature of the spectrum depends on the parameter V/t: the spectrum is continuous for $V/t < 1$, pure point for $V/t > 1$, and singular continuous for $V/t = 1$.

For the Fibonacci models in Eqs. (12) and (13) the energy spectrum is singular continuous as soon as there is aperiodicity, however small (Delyon, Lévy, and Souillard, 1985; Bellissard *et al.*, 1989; Süto, 1989). The situation is analogous to that of the Anderson model for 1D disordered metals, where the critical value for localization in one dimension for disorder strength is zero.

It is noteworthy that the spectra in all three cases are pure spectra, meaning purely singular continuous, pure point, or absolutely continuous. In general, however, models may have spectra with several different components, and there may be one or more mobility edges separating different regions. This is the case for the Anderson model in three dimensions for disorder strengths that are smaller than the critical value. In one dimension there can also be mobility edges. This occurs in generalized Harper models, where the potential energy depends on two incommensurate wave vectors, as discussed by Hiramoto and Kohmoto (1989, 1992) and reconsidered recently by Das Sarma and Xie (1988), Ganeshan, Pixley, and Das Sarma (2015), and Liu, Ghosh, and Chong (2015).

Figure 7 shows three typical forms of the densities of states for the three models. Figure 7(a) shows the DOS for the off-diagonal model for the case $t_A = 0.6$, $t_B = 1$, and periodic boundary conditions. This model has a chiral symmetry: for each solution $|\psi\rangle$ of energy E, one has a solution $|\psi'\rangle$ of energy $-E$ such that $\langle n|\psi'\rangle = (-)^n\langle n|\psi\rangle$. The spectrum is therefore symmetric around 0, as can be seen in Fig. 7. The horizontal axis represents the dimensionless energy E/t_B. The band structure is seen to be composed of three main clusters, each of which comprises three subclusters, etc. Each level broadens into a band when periodic boundary conditions are assumed. The process of subdivision into smaller bands continues as one considers larger and larger approximant chains.

The spectrum for the diagonal model for $\epsilon_A \neq \epsilon_B$ is similar. Figure 7(b) shows the DOS computed numerically for an

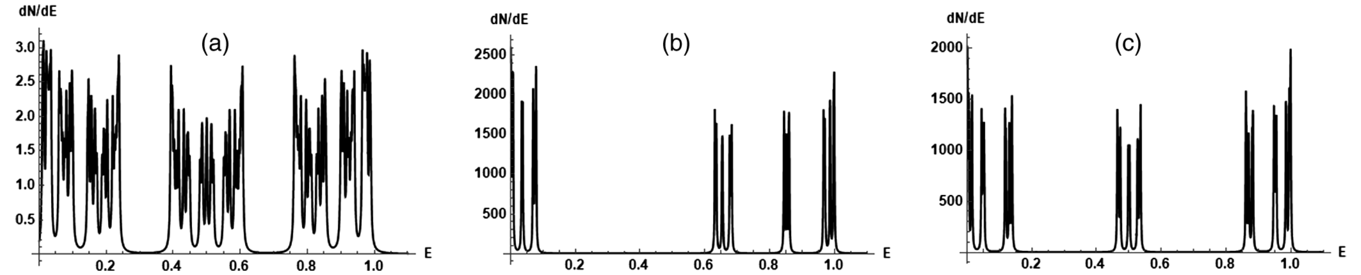

FIG. 7. Densities of states dN/dE for three models. (a) Off-diagonal Fibonacci model [Eq. (13)] with $t_A/t_B = 0.6$. (b) Diagonal Fibonacci model [Eq. (14)] with $\varepsilon = 4$. (c) AAH model [Eq. (15)] at criticality.

approximant chain of $N = 144$ sites. The parameters were taken to be $\epsilon_A = -\epsilon_B = 2t$, with periodic boundary conditions. The spectrum, which is asymmetric, has two main clusters. These clusters are in turn composed of three subclusters that trifurcate into three clusters, etc.

Finally, in Fig. 7(c) we show the DOS for the AAH model computed at criticality $V = 1$, with $\tau = \tau_n$ in the cosine term, for a system of $N = 144$ sites with periodic boundary conditions. For the AAH model at criticality as for the off-diagonal model, the bands divide into three subbands when one goes from one approximant to the next (Hiramoto and Kohmoto, 1989).

Figures 7(a)–7(c) each correspond to a given system size. When the size is increased, one observes a characteristic feature of multifractal structures, namely, local power-law singularities of the DOS, $N(E + \Delta E) - N(E) \sim \Delta E^{-\alpha(E)}$. As the system size gets larger, bandwidths shrink, with each one scaling with a different exponent α. To fully describe this multifractal spectrum, one needs the full set of exponents α and their densities $f(\alpha)$. This can be done using standard methods of multifractal analysis (Halsey *et al.*, 1986). The method consists of defining the "partition function" as

$$\Gamma_n(q, \tau) = \sum_E \frac{(1/F_n)^q}{[\Delta_n(E)]^\tau}, \tag{17}$$

where $\Delta_n(E)$ is taken to be the width of the energy band associated with the energy level labeled E. One determines τ as a function of q by requiring that $\Gamma \sim 1$ as $n \to \infty$. The function $f(\alpha)$ is the Legendre transform of $\tau(q)$ given by

$$\alpha_q = \frac{d(q-1)d_q}{dq} \tag{18}$$

and

$$f(\alpha_q) = q\alpha_q - \tau_q. \tag{19}$$

The function $f(\alpha)$ gives the fraction of sites around which the DOS scales with the power α. $f(\alpha)$ is typically a convex curve extending between the extremal values $\alpha_{\min}$ and $\alpha_{\max}$. For the periodic crystal when the spectrum is continuous, this curve reduces to only two points, $\alpha = 1$ describing the interior of the band and $\alpha = 1/2$, due to van Hove singularities at the band edges, as at the bottom of the band where $dN(E) \sim (E - E_{\min})^{1/2}$. In the quasiperiodic case, singularity strengths vary throughout the energy spectrum. Figure 8, from Rüdinger and Piéchon (1998), shows $f(\alpha)$ values (indicated by crosses) computed numerically for $t_A/t_B = 0.2$. Exact expressions can be obtained for scaling exponents $\alpha(E)$ for two special energies, as we later explain using the trace map method, as we explain in Sec. III.D.

C. Gap labeling and topological indices

In one-dimensional problems, the integrated density of states (IDOS) $N(E)$, defined as the fraction of states of energy less than E, is also equal to the number of changes of sign (nodes) of the wave function per unit length. One can thus introduce a wave number $k(E) = N(E)/2$ corresponding to a state of energy E. For the nth periodic approximant, the spectrum consists of F_n bands, each corresponding to wave vectors k_j, such that the IDOS between two bands j and $j + 1$ has the value j/F_n. Note that the IDOS is a more tractable quantity than the DOS, which fluctuates violently as a function of the given energy when the system size is increased. The IDOS, in contrast, has plateaus whose positions are well defined as system sizes are increased. This has its importance for calculations in which the chemical potential enters as a parameter. The IDOS curve approaches the devil's staircase form in the limit of infinite size.

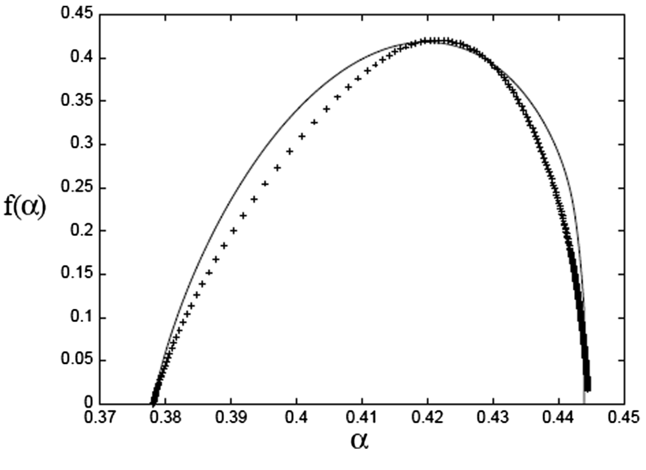

FIG. 8. $f(\alpha)$ computed numerically (crosses) for the off-diagonal Fibonacci model for $\rho = 0.2$. The solid line corresponds to an analytic expression obtained using the trace map (see the text). From Rüdinger and Piéchon, 1998.

The gap labeling theorem (Bellissard *et al.*, 1989; Bellissard, Bovier, and Ghez, 1992) states that, of the class of models given by Eq. (12), the IDOS $N(E)$ within the gaps must take values given by

$$N(E) = \mathbf{p} + \frac{\mathbf{q}}{\tau}, \tag{20}$$

where $\mathbf{p}$ and $\mathbf{q}$ [not to be confused with the reciprocal space vector or the multifractal parameter q defined in Eq. (17)] are integers. The pair of indices $(\mathbf{p}, \mathbf{q})$ label all of the possible gaps, but the gap labeling theorem does not specify whether or not a given gap is actually opened. It suffices to specify only one integer $(\mathbf{q})$, as $\mathbf{p}$ is then fixed by the condition $0 \leq N(E) \leq 1$.

The mapping between the FC quasicrystal and a 2D quantum Hall system has been discussed by Zilberberg and collaborators (Kraus and Zilberberg, 2012; Kraus *et al.*, 2012; Kraus, Ringel, and Zilberberg 2013). This mapping shows that $\mathbf{q}$ is a topological quantity, a Chern number inherited from the 2D parent model. As expected for a topological invariant, it is robust under local perturbations due to disorder or other scattering that preserves symmetry. The gap label $\mathbf{q}$ represents a winding number that describes the variations of the edge modes in a system that has interfaces. This bulk-edge correspondence is discussed in more detail in Sec. III.F.

Figure 9 shows the IDOS for each of the three models plotted as a function of the dimensionless energy E/t. The horizontal lines indicate values of IDOS given by Eq. (20) for gaps corresponding to values of $-3 \leq \mathbf{q} \leq 3$. For the three cases, Figs. 9(a)–9(c) show that they have identical gap positions, as given by the gap labeling theorem. This topological equivalence can be shown with an explicit mapping between models (Kraus *et al.*, 2012; Verbin *et al.*, 2013). In an experiment using a photonic waveguide array, the topological equivalence of the Fibonacci and Harper models was explicitly shown by Verbin *et al.* (2015).

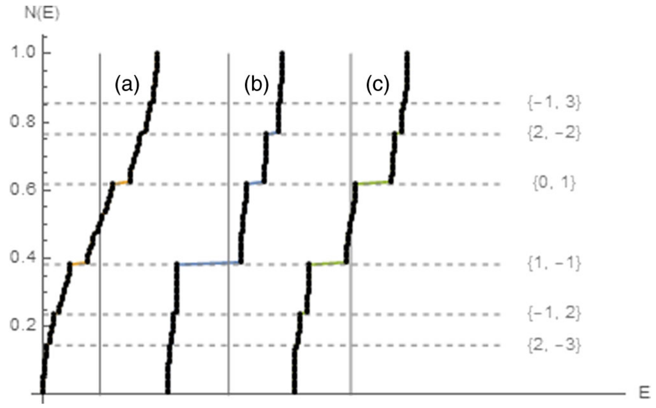

FIG. 9. Integrated DOS $N(E)$ vs the energy E (in dimensionless units) for three topologically equivalent models. (a) Off-diagonal model [Eq. (13)] ($\rho = 0.7$). (b) Diagonal model [Eq. (14)] ($\varepsilon = 4$). (c) Critical AAH model [Eq. (15)]. In all the plots, energies were shifted and normalized such that the total bandwidths are equal to 1 (system size $N = 144$, periodic boundary conditions).

D. Trace map method

The trace map analysis is a powerful technique that has led to an exact renormalization group scheme, producing many important results for scaling properties. The starting point is the definition of transfer matrices relating the wave-function amplitudes on the $(n+1)$th site to the amplitudes on sites n and $n-1$. From Eq. (12) one has the tight-binding equations

$$(E - \epsilon_n)\psi_n + t_n\psi_{n+1} + +t_{n-1}\psi_{n-1} = 0. \tag{21}$$

This relation can be reexpressed in terms of a 2×2 matrix equation as follows:

$$\begin{aligned} \begin{bmatrix} \psi_{n+1} \\ \psi_n \end{bmatrix} &= \begin{bmatrix} (E - \epsilon_n)/t_n & -(t_{n-1}/t_n) \\ 1 & 0 \end{bmatrix} \begin{bmatrix} \psi_n \\ \psi_{n-1} \end{bmatrix} \\ &= \left(\prod_{k=2}^{n} T_{k,k+1} \right) \begin{bmatrix} \psi_1 \\ \psi_0 \end{bmatrix} \\ &= M_n \begin{bmatrix} \psi_1 \\ \psi_0 \end{bmatrix}, \end{aligned} \tag{22}$$

where we have introduced the local transfer matrix $T_{k,k+1}$ and the global transfer matrix M_n that is a product of $n-1$ such transfer matrices, with the order of multiplication of the matrices given by $M_n = \ldots T_{2,3}T_{1,2}$.

(1) *Diagonal model*.—The local transfer matrix depends on the on-site energy ϵ_n and the amplitudes for hopping onto the sites to the left and to the right of site n. For the diagonal model, there are only two possible transfer matrices, namely,

$$\begin{aligned} T_A &= \begin{bmatrix} (E - \epsilon_A)/t & -1 \\ 1 & 0 \end{bmatrix}, \\ T_B &= \begin{bmatrix} (E - \epsilon_B)/t & -1 \\ 1 & 0 \end{bmatrix}. \end{aligned} \tag{23}$$

We now consider the approximant chain of length $N = F_n$ and let $x_n = (1/2)\mathrm{Tr}M_n$ be the half trace of the transfer matrix. For an energy E to correspond to an allowed (normalizable) wave function, the half trace of M_N must satisfy the condition $|x_n| \leq 1$. Thanks to the concatenation property of chains mentioned in Sec. II.A, namely, $C_{n+1} = C_n \oplus C_{n-1}$, the global transfer matrices for successive approximants satisfy (Kohmoto, Kadanoff, and Tang, 1983; Ostlund *et al.*, 1983)

$$M_{n+1} = M_{n-1}M_n. \tag{24}$$

Given Eq. (24), it can be shown that the half traces satisfy the following three term recursion relation (Kohmoto, Kadanoff, and Tang, 1983):

$$x_{n+1} = 2x_nx_{n-1} - x_{n-2}, \tag{25}$$

with the initial conditions

$$x_{-1} = 1, \qquad x_0 = \frac{(E - \epsilon_B)}{2}, \qquad x_1 = \frac{(E - \epsilon_A)}{2}. \tag{26}$$

To determine which energies belong in the spectrum, one computes the iterates x_n using Eq. (25) and checks to see whether they remain bounded and within the interval $(-1, 1)$.

(2) *Off-diagonal model.*—A similar set of relations can be obtained in the case of the off-diagonal model. One starts by introducing three different transfer matrices (T_{AA}, T_{AB}, and T_{BA}) for the three bond configurations AA, AB, and BA that are possible in the FC. These matrices are defined by

$$T_{AA} = \begin{bmatrix} E/t & -1 \\ 1 & 0 \end{bmatrix},$$
$$T_{AB} = \begin{bmatrix} E/t & -t_B/t_A \\ 1 & 0 \end{bmatrix},$$
$$T_{BA} = \begin{bmatrix} E/t & -t_A/t_B \\ 1 & 0 \end{bmatrix}. \tag{27}$$

The problem of writing the global transfer matrix can be simplified (Kohmoto, Sutherland, and Tang, 1987), as the hopping on Fibonacci chains can be described with only two matrices: T_{AA} and $T_{AB}T_{BA}$. If we rename these transfer matrices as T_B and T_A, respectively, the global transfer matrices for approximant chains can be written exactly as in the diagonal case.

The recursion relations (24) and (25) therefore also hold for the off-diagonal model. The initial conditions for the half traces in the off-diagonal case are

$$x_{-1} = \frac{1}{2}\left(\frac{t_B}{t_A} + \frac{t_A}{t_B}\right),$$
$$x_0 = \frac{E}{2t_B}, \qquad x_1 = \frac{E}{2t_A}. \tag{28}$$

The recursion relation for the traces [Eq. (25)] constitutes a dynamical system in a three-dimensional space. Defining the variables $x = x_{n-1}$, $y = x_n$, and $z = x_{n+1}$ [Eq. (25)] maps a given point as follows:

$$x \to x' = y,$$
$$y \to y' = z,$$
$$z \to z' = 2yz - x. \tag{29}$$

One of the invariants of the dynamical system [Eq. (29)] is the quantity (Kohmoto, Kadanoff, and Tang, 1983; Kohmoto and Oono, 1984; Kohmoto, Sutherland, and Tang, 1987)

$$\begin{aligned} I &= x^2 + y^2 + z^2 - 2xyz - 1 \\ &= \tfrac{1}{4}(\epsilon_A - \epsilon_B)^2 \quad \text{(diagonal model)} \\ &= \frac{1}{4}\left(\frac{t_A}{t_B} - \frac{t_B}{t_A}\right) \quad \text{(off-diagonal model)}, \end{aligned} \tag{30}$$

where the last two lines were written using the initial conditions for the diagonal and off-diagonal model, respectively. For a proof of the invariance of I, a so-called Fricke character, see Baake, Grimm, and Joseph (1993). Under the dynamical map, points move on the surface $I = \text{const}$ in the three-dimensional space. Details of the form of these surfaces for different values of the parameters and of different kinds of orbits were given by Kalugin, Kitaev, and Levitov (1986). Orbits that escape to infinity, such that $\lim_{n\to\infty} x_n$ is infinite, correspond to energies that are not in the spectrum. Numerically, this is found to be the case for almost all energies, which is consistent with the fact that the spectrum has a Lebesgue measure of zero. Periodic orbits with $\lim_{n\to\infty} x_n \leq 1$ correspond to allowed energies.[3] It can be shown, by tracing orbits for successive periodic approximants, that the band structure has a self-similar structure, i.e., is a Cantor set.

Kohmoto, Kadanoff, and Tang obtained exact results for two cases where the trace map leads to a periodic orbit (Ostlund *et al.*, 1983; Kohmoto and Oono, 1984; Kohmoto and Banavar, 1986; Kohmoto, Sutherland, and Tang, 1987). By considering the linearized map around these special points of the spectrum, they found the scaling exponents for the corresponding bands in terms of the escape rates of the dynamical map. The bandwidths are given by $\Delta \sim \omega^\epsilon$, where ϵ is the minimal eigenvalue of the linearized map as given for the following two special cases.

(1) Solution for the band center. The trace map has a periodic orbit consisting of the six cycle $(0, 0, a) \to (-a, 0, 0) \to (0, -a, 0) \to (0, 0, -a) \to (a, 0, 0) \to (0, a, 0) \to (0, 0, a)$, where $a = \sqrt{I + 1}$. The scaling exponent for this band can be expressed in terms of the eigenvalue ϵ_6 of the linearized equation around this six cycle. The result thus obtained for α_{ctr} (Kohmoto and Oono, 1984) is

$$\alpha_{\mathrm{ctr}} = \ln \tau^6 / \ln \epsilon_6,$$
$$\epsilon_6 = \left[\sqrt{1 + 4(1 + I)^2} + 2(1 + I)\right]^2. \tag{31}$$

(2) Solution for band edges. These correspond to two cycles of the trace map $(a, b, b) \to (b, a, a) \to (a, b, b)$, where $a = J + \sqrt{J^2 - J}$ and $b = J - \sqrt{J^2 - J}$, with $J = (1/8)[3 + \sqrt{25 + 16I}]$. The scaling exponent for these bands is expressed in terms of ϵ_2, the eigenvalue of the linearized map, as follows:

$$\alpha_{\mathrm{edge}} = \ln \tau^2 / \ln \epsilon_2,$$
$$\epsilon_2 = \left[8J - 1 + \sqrt{(8J - 1)^2 - 4}\right]/2. \tag{32}$$

Kohmoto, Sutherland, and Tang (1987) conjectured that the α_{ctr} and α_{edge} values correspond to the extremal values, namely, $\alpha_{\min}$ and $\alpha_{\max}$. In fact, however, Rüdinger and

---

[3] There are in principle two other more "exotic" possibilities (iii) aperiodic and bounded orbits, and (iv) recurrent orbits where the point returns to the allowed region and for which $\lim_{n\to\infty} x_n \leq 1$.

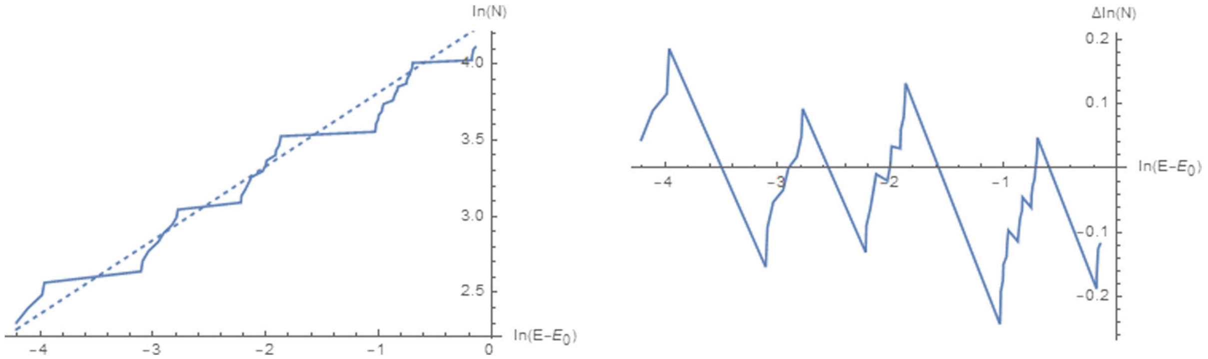

FIG. 10. Left panel: log-log plot showing the numerically computed IDOS vs energy for the hopping model in the vicinity of $E = E_{\min}$ (for $\rho = 0.4$). The dashed line indicates an averaged behavior. Right panel: expanded plot of the fluctuations around the dashed line $[\Delta \ln(N)]$ showing the main period of the oscillation and some smaller periods.

Piéchon (1998) showed that this is not always the case by analyzing the trace map in the vicinity of a four cycle that governs scaling for the IDOS values $N(E) = 1/3$ and $2/3$. Their analysis showed that the maximal value of α occurs at these points when ρ is small. Another conjecture concerned the possibility that the spectrum becomes monofractal when $\rho = \rho_c$ (Zhong, Bellissard, and Mosseri, 1995). This conjecture was based on the fact that α_{ctr} is equal to α_{edge} for the hopping ratio $\rho_c \approx 0.0944$ [as deduced from Eqs. (31) and (32)]. However, Rüdinger and Pièchon's calculation showed that for $\rho = \rho_c$ $\alpha_{1/3}$ is different from (more precisely, is larger than) the other two exponents. Thus, the spectrum is not a monofractal. An approximate analytical expression for $f(\alpha)$ derived by Rüdinger and Piéchon (1998) is shown in Fig. 8, along with the numerical data for $\rho = 0.2$.

The fractal exponent for the self-similar $E = 0$ wave function in the hopping model is found by the trace map calculation to be $|\ln \rho|/\ln \tau^3$, which is in good agreement with numerical calculations of the wave function (Kohmoto and Banavar, 1986).

Discussions of trace maps and their dynamical properties were given in the reviews by Baake, Grimm, and Joseph (1993) and Damanik, Embree, and Gorodetski (2015). Generalizations of the trace map for mixed Hamiltonians with two or more parameters are discussed in Sec. IX. These generalized models have a larger parameter space with more possibilities for the spectra. They can admit extended states for special energies.

E. Log-periodic oscillations

Systems with discrete scale invariances can display log-periodic oscillations in thermodynamic properties, as noticed in early treatments of critical phenomena (Nauenberg, 1975; Derrida, Itzykson, and Luck, 1984). To cite a more recent study, Gluzman and Sornette (2002) considered an observable $f(x)$ in a system close to criticality, where $f(x) = \mu^{-1} f(\gamma x)$ under a renormalization transformation. They showed that $f(x)$ has a power-law scaling "decorated" by a log-periodic function $f(x) = x^m P(\ln x/\ln \gamma)$. The power is given by $m = \ln \mu/\ln \gamma$ and the period of the oscillations is $\log \gamma$. This is indeed what one observes for the IDOS $N(E)$ in the Fibonacci model. Figure 10(a) shows in a log-log plot the IDOS versus energy in the bottom of the band. The points are obtained by numerical diagonalization, and the straight dashed line indicates the average IDOS. Figure 10(b) shows the fluctuations of $\ln(N)$ around the average value. The period of the oscillations corresponds to the inflation factor, which in this case is $\gamma = \tau^2$ for the sidebands; for a description of the renormalization transformation of the Hamiltonian, see Sec. IV. The main period and some smaller ones indicating a fractal structure can be seen.

F. The wave function for $E = 0$

We discuss here an exact solution for one of the wave functions of the hopping model. It provides a rare example of a nontrivial case where multifractal properties can be computed analytically as a function of ρ.

The wave function at the band center $E = 0$ (shown in Fig. 11 for a finite approximant) can be determined exactly using a recursive construction. It turns out to be a particularly simple form of the critical states proposed by Kalugin and Katz (KK) for the ground state of tilings (Kalugin and Katz, 2014). They argued that, for a family of quasiperiodic Hamiltonians that includes all the standard ones, the ground state $|\psi\rangle$ can be written as a product of two factors. The amplitude on site i is given by

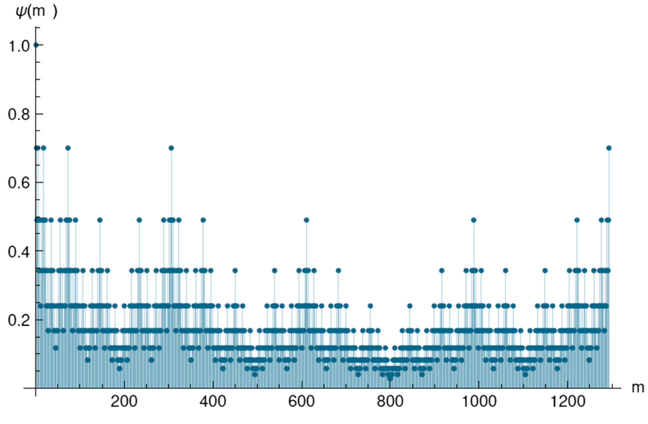

FIG. 11. Center state on-site probabilities $|\psi_i(E = 0)|^2$ vs site index i (numerically computed for an $n = 12$ chain with $\rho = 0.6$ and periodic boundary conditions).

$$\langle i|\psi\rangle = C(i)e^{\kappa h(i)}, \tag{33}$$

where κ is a real constant. The prefactors $C(i)$ depend on the local configuration of the atoms around site i. Long-range correlations between sites are given by the exponent h, called the *height field*, which is the integral of a quasiperiodic function.[4] The $E = 0$ wave function of the Fibonacci chain has the form of Eq. (33), with the particular choice $C(i) = \pm 1$ depending on the sublattice to which the site i belongs. This solution for the 1D chain is a relatively tractable case study to illustrate some of the properties of the KK eigenstates, which are more complex in higher-dimensional quasicrystals.

From the Hamiltonian (13), one obtains the following relation for the $E = 0$ wave-function amplitudes on i and $i + 2$:

$$t_{i+1}\psi_{i+2} + t_i\psi_i = 0. \tag{34}$$

There are two independent $E = 0$ solutions, one for each sublattice. With the two being equivalent in the limit of the infinite FC, we henceforth consider the even sublattice solution for sites $i = 2m$. There are three possibilities for the bond configurations between sites i and $i + 1$, namely, AA, AB, and BA. The three cases are given by

$$\psi_{m+1} = -\rho^{A(m)}\psi_m, \tag{35}$$

where $\rho = t_A/t_B$ and the A (for *arrow*) function is defined locally according to the configuration of the bonds between the two sites

$$A(m) = \begin{cases} +1 & (\mathrm{AB}), \\ -1 & (\mathrm{BA}), \\ 0 & (\mathrm{AA}). \end{cases} \tag{36}$$

Figure 12 shows the arrow function for the even sites of a small chain segment. The figure shows the arrows corresponding to the three bond configurations that are possible using the conventions: a right arrow for the bond sequence AB, a left arrow for the bond sequence BA, and no arrow for the bond sequence AA.

Repeating the recursion relation (35), one obtains

$$\begin{aligned}\psi_m &= (-1)^m\rho^{h(m)}\psi_0 \\ &= (-1)^m e^{\kappa h(m)},\end{aligned} \tag{37}$$

where $h(m) = \sum_0^m A(j)$, $\kappa = \ln\rho$, and ψ_0 was set at 1. This expression is of the KK form [Eq. (33)], with a constant prefactor on all sites. The function h in the exponent is an integral of a quasiperiodic function $A(m)$. Figure 12 shows the height function for the first few even sites. As the length of the chain gets larger, the height function fluctuates more and more. Figure 13 shows the height function calculated for a long segment of the Fibonacci chain. The properties of the wave function can be determined when the distribution of heights is known. One can show by explicit calculation that the wave function is multifractal and can express all of its generalized dimensions D_q^ϕ in terms of ρ. This can be done by introducing inflation matrices to relate the heights in the C_n and C_{n-2} chains. In the large n limit, the height distribution $P(h)$ satisfies a diffusion equation as a function of t (the number of inflations) as follows:

$$P^{(t)}(h) \sim \frac{1}{\sqrt{4\pi Dt}}\exp\left(-\frac{h^2}{4Dt}\right), \tag{38}$$

where the diffusion coefficient is given by $D = 1/2\sqrt{5}$. See Macé *et al.* (2017) for details.

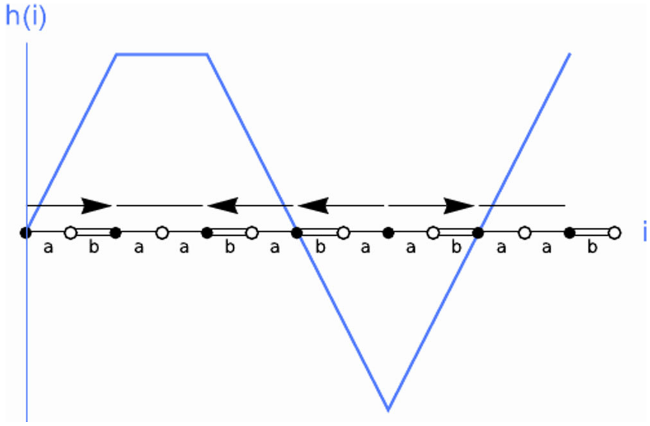

FIG. 12. Definition of the local arrow function and its integral, the height function. From Macé *et al.*, 2017.

Since $P(h)$ is a symmetric distribution around $h = 0$, the resulting form of the wave function has a symmetry between peaks and valleys, as seen in Fig. 11. The typical value of h in a chain of $N = \tau^n$ sites is given by the standard deviation of the Gaussian after a time $t = n$, $h_{\mathrm{typ}} \sim \sqrt{2Dn}$. This leads to a typical value of ψ that falls off with the chain length $N = \tau^n$ as $\psi(2N) \sim e^{-cst\sqrt{2D\ln N}}$. The spatial decay of the wave function is thus faster than power-law decay but slower than

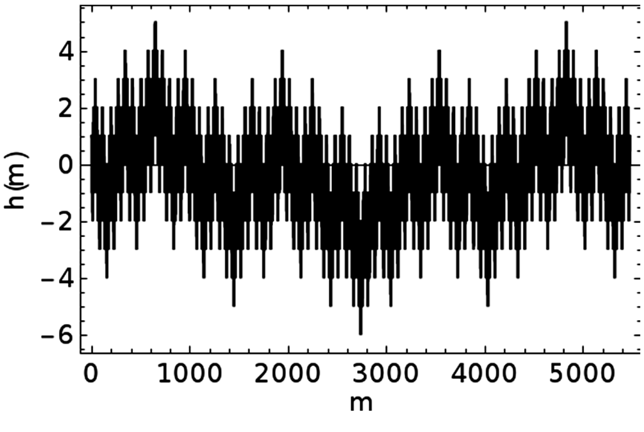

FIG. 13. Height function for a long chain showing its fluctuations at large distances. From Macé *et al.*, 2017.

---

[4] Note that Eq. (33) can be considered a generalization of the usual Bloch form for the wave functions in a periodic lattice, which can be written as a product of a periodic function $u_n(x)$ (in one dimension) and an exponential $e^{ih(x)}$, where $h(x) = kx$ is the integral of the Bloch wave vector k.

exponential decay. In contrast, note that, for the randomly disordered off-diagonal model, a similar argument gives the wave function at $E = 0$ as $\psi(2N) \sim e^{-cst\sqrt{2DN}}$ (Theodorou and Cohen, 1976; Economou and Soukoulis, 1981; Inui, Trugman, and Abrahams, 1994). This is a stretched exponential function that decays much faster than the $E = 0$ wave function of the Fibonacci chain.

The fractal dimensions of ψ can be exactly computed. These quantities are deduced from the scaling of the moments of the wave functions, which are defined as follows. Let the q weight of the wave function ψ be defined by

$$\chi_q(\psi, \mathcal{R}) = \frac{\sum_{i \in \mathcal{R}} |\psi_i|^{2q}}{(\sum_{i \in \mathcal{R}} |\psi_i|^2)^q}, \tag{39}$$

where the sums run over all sites in a given region $\mathcal{R}$. The q weight is a measure of the fraction of the presence probability contained inside region $\mathcal{R}$.

Consider a sequence of regions $\mathcal{R}_n$ whose radius grows to infinity as $n \to \infty$. Defined as follows, the qth fractal dimension $D^{\psi}{}_q(\psi)$ is the scaling of the q weight with the volume of the region:

$$D_q^{\psi}(\psi) = \lim_{n \to \infty} \frac{-1}{q-1} \frac{\log \chi_q(\psi, \mathcal{R}_t)}{\log \Omega(\mathcal{R}_n)}, \tag{40}$$

where Ω is the number of sites inside region $\mathcal{R}$. As we have already seen for the DOS in Sec. V.A, one can then compute the Legendre transform of the fractal dimensions $f_{E=0}(\alpha)$. This function gives the fraction of sites for which the wave function scales with the power α.

$f_{E=0}(\alpha)$ curves obtained using the exact calculation for different values of ρ are plotted in Fig. 14. As the figure shows, in each case the α values lie within a finite interval, indicating that ψ is multifractal. As ρ approaches 1, the support of the function shrinks to a single point, $\alpha = 1$, corresponding to the extended state. Another point to note: thanks to the symmetry of the height distribution, the function $f_{E=0}(\alpha)$ is symmetric around its maximum, as was observed in numerical studies of this wave function (Evangelou, 1987; Fujiwara, Kohmoto, and Tokihiro, 1989). In other words, as the system size increases, the minima (maxima) of ψ scale to zero (infinity) in the same manner.

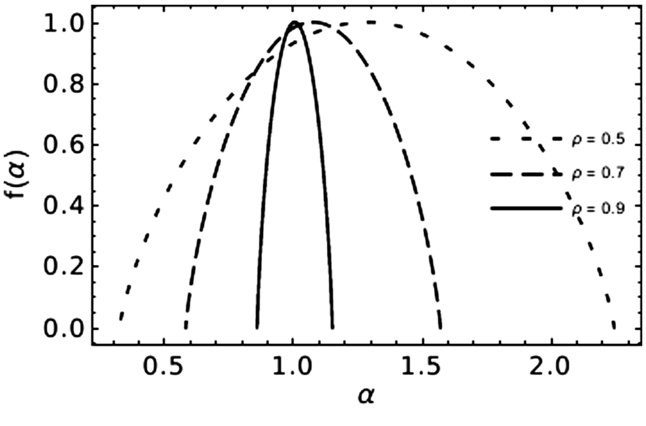

FIG. 14. $f_{E=0}(\alpha)$ spectrum as given by Eq. (40) for the $E = 0$ wave function for different values of the hopping ratio ρ. Note the symmetry of $f_{E=0}$ around its maximum value. From Macé *et al.*, 2017.

The transmission coefficient for this $E = 0$ wave function can also be calculated exactly. Note that this quantity (which is discussed in Sec. VII) has the exact value of 1 (i.e., transmission is perfect) for certain well-defined distances along the chain out to arbitrarily large distances.

G. Chern numbers: Bulk-edge correspondence

The close connection between topological phases and quasicrystals that are described in a higher-dimensional space has been pointed out by many (Kraus *et al.*, 2012; Verbin *et al.*, 2013; Huang and Liu, 2018, 2019). These show that, for 1D quasicrystals, there are 2D Chern numbers and topologically protected boundary states similar to those in a 2D quantum Hall system.

Edge modes are expected to be present in the quasicrystal, in analogy with those in the AAH model. Just as changing the arbitrary phase ϕ in the AAH model [Eq. (15)] leads to tuning the edge mode energy, one can tune edge modes in FC approximants by varying the arbitrary phase φ in Eq. (11). This is seen in Fig. 15, which shows for an 89-site chain the energy levels as a function of the parameter $0 \le \varphi \le 2\pi$ [the figure was rendered symmetric with respect to π by shifting the angle by $\varphi_0 = -\omega\pi(N+1)$]. It can be seen that the levels remain flat as ϕ is varied until a sudden phason flip occurs somewhere along the chain. There are in all N such flips in the interval. The label of the gap q gives the number of gap crossings of the states, which are seen most clearly in the main gaps of the spectrum in Fig. 15.

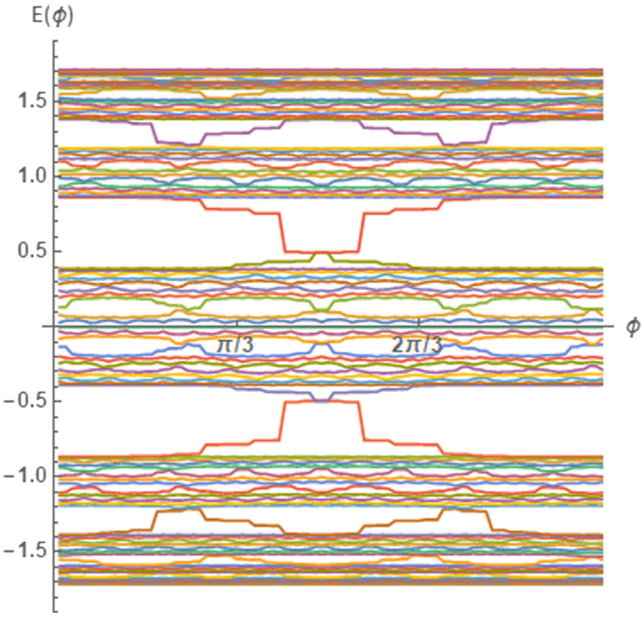

FIG. 15. Energy spectrum vs ϕ for energy levels of the off-diagonal model in an open 89-site chain ($\rho = 0.7$). The number of gap crossings of states is most easily counted for the largest gaps ($|\mathbf{q}| \le 4$).

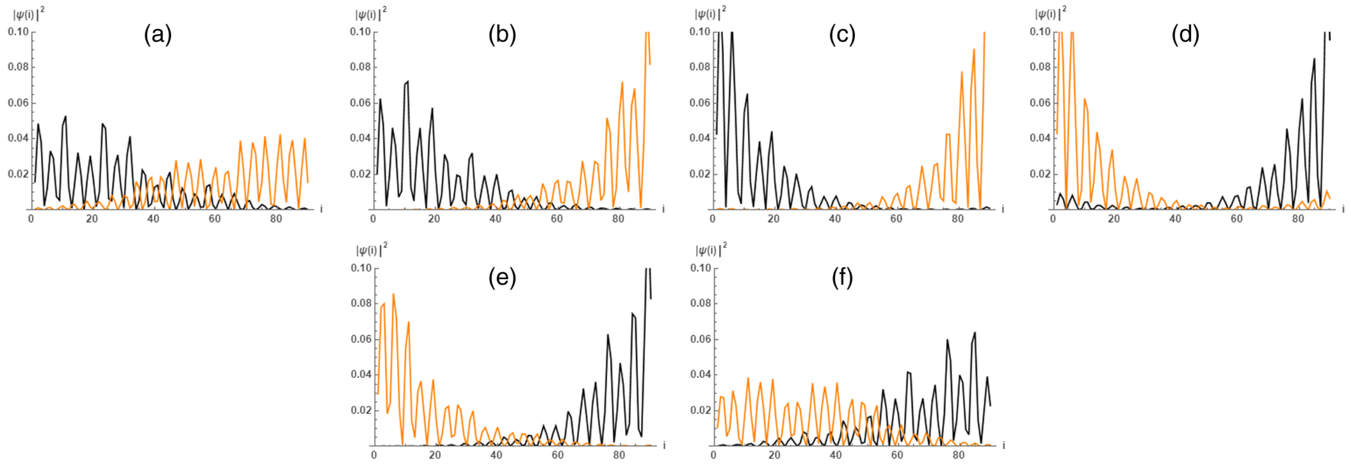

FIG. 16. Evolution of eigenstates on either side of the $\mathbf{q} = 2$ gap showing the changes as ϕ is varied. In this series of panels the upper band edge state probability, shaded orange (light gray), and the lower edge state probability, shown in black, evolve progressively from extended in-band states to localized edge states, which then exchange positions (hop between the edges in opposite directions) and finally become in-band states again. In (a)–(f) the values of ϕ are equal to 0.22π, 0.33π, 0.44π, 0.51π, 0.62π, and 0.71π.

Experimental studies of the hopping Hamiltonian using polaritonic cavity modes to detect eigenmodes and their energies can be performed, as shown by Tanese *et al.* (2014) and Baboux *et al.* (2017). In the experiments, nearest neighbor cavities were spaced so as to be linked by a strong or a weak coupling, following the Fibonacci sequence. Chains of given length N, one for each ϕ value, were fabricated in a Fabry-Perot geometry, resulting in edge modes located at the central mirror symmetric position. For a given gap of label $\mathbf{q}$, the corresponding edge mode was observed to cross the gap $\mathbf{q}$ times, confirming that this is indeed a winding number. The sign of $\mathbf{q}$ determines the sense of the gap crossing (from the upper to the lower edge, or vice versa).

One can use the winding property of states to “pump” charge adiabatically across the chain, as was done in experiments with photonic quasicrystals by Kraus *et al.* (2012) and Verbin *et al.* (2013). The “jumping” of states from one edge to the other as the ϕ parameter is changed is shown in Fig. 16 for the $\mathbf{q} = 2$ gap states (where there are two such jumps in the 2π interval). This topological pumping of charge can have consequences for physical properties. We discuss one consequence for the proximity effect in a chain coupled to a superconductor in Sec. VIII.

Röntgen *et al.* (2019) studied real space bond configurations for the appearance of edge modes. They showed that the edge modes are linked to local “resonators”: the term they used to denote clusters of bonds that are symmetric under reflection. The localization length and energy of the edge state depend on the resonator size (i.e., the distance out to which they possess reflection symmetry).

Chern numbers were also observed in a light diffraction experiment (Dareau *et al.*, 2017). In the experiment, a digital micromirror device was used to realize a set of approximant chains of fixed length and different values of ϕ in Eq. (11). The behavior of the diffraction peak at different wave vectors k was shown to depend on the associated topological number $\mathbf{q}$.

IV. APPROXIMATE METHODS

A. Perturbation theories

Many different kinds of perturbative calculations have been done to study electronic properties of the FC, in both real and reciprocal space.

Luck (1989) carried out a perturbation expansion for the diagonal model in terms of the Fourier components of the potential. Taking the on-site energies to be $\epsilon_A = V$ and $\epsilon_B = -V$ using a suitable shift of the origin, one can compute the Fourier transform of the potential $VG_N(k)$ and the structure factor $S_N(k) = V^2|G_N(k)|^2$. In the thermodynamic limit the structure factor can be shown to have power-law singularities at a dense set of reciprocal space vectors k_0 (as seen in Sec. II.B). In the vicinity of each of the peaks, one has

$$S(k)dk \sim |k - k_0|^{\alpha}. \tag{41}$$

For a general potential the singularity strength α can vary depending on the peak, whereas for the quasicrystal $\alpha = 1$ for all peaks according to the arguments that we presented in Sec. II. Luck (1989) showed for the general case that the width of the gap that opens at the unperturbed energy $\epsilon(K = k_0/2)$ is related to α, the singularity at $k = k_0$. Specifically, for the gap where the IDOS $N(E) = k_0/2\pi$, the gap width is given by

$$\Delta \sim V^{\beta}, \tag{42}$$

where $\beta = 2/(2 - \alpha)$. In the case of the quasicrystal, $\beta = 1$ for all the gaps. This analysis shows that, for weak quasiperiodic potentials, the plateaus of the IDOS are related in a natural way to the module of wave vectors. This perturbation theory does not converge, even for arbitrarily weak potentials, as pointed out by Kalugin, Kitaev, and Levitov (1986), because of the nature of the Fourier module of the quasicrystal, which consists of a dense distribution of peaks. Nevertheless, the indexing of gaps using this method is robust. The gap labeling theorem (Bellissard *et al.*, 1989) provides the rigorous justification that the indexing continues to hold for arbitrarily strong potentials. Many other perturbative approaches have been proposed for the off-diagonal model, including a real space perturbation theory starting with the periodic limit (Sire and Mosseri, 1989; Rüdinger and Sire, 1996). The method of Sire and Mosseri (1989), when applied to the Fibonacci chain, yields exact expressions for positions of the gaps and associated gap labels, as well as perturbative results for gap widths. The latter hold well for the main gaps even for a moderately large perturbation, but not for small gaps. For the diagonal model, Barache and Luck (1994) introduced a perturbation theory that starts with a strong atomic limit $V_i = \pm V$, where the on-site potential strength V is large relative to the hopping amplitude t. The spectrum and density of states were computed in degenerate perturbation theory, and the gap structure deduced for this case was shown to be consistent with the gap labeling theorem.

B. Approximate renormalization group

Here we describe the main ideas behind a perturbative real space RG method attributed to Niu and Nori (1986, 1990) and Kalugin, Kitaev, and Levitov (1986) and Levitov (1989). This approach has been extremely fruitful for describing a large number of static and dynamic properties of the FC. In this section we describe the basic notions of this RG for the off-diagonal and diagonal models.

RG for off-diagonal model (1).—We begin with details of the RG for the off-diagonal model [Eq. (13)], where $t_B > t_A$. The hopping ratio $\rho = t_A/t_B$ lies in the range $0 \leq \rho \leq 1$. Recall that one can assume that both t_A and t_B are positive, because if they are not the solutions can be found from our model using a suitable mapping (or local gauge transformation) of the wave functions. The goal of this RG is to obtain a description of the spectrum and states perturbatively in ρ.

For $\rho = 0$, the chain breaks up into disconnected groups of sites that can be classified as follows: atom sites are the sites sandwiched between A bonds, while molecule sites are pairs of sites linked by a B bond. The spectrum, in this limit, consists of only three discrete degenerate levels: the $E = 0$ level of the atoms, and $E = \pm t_B$ for the molecular bonding and antibonding levels. For a chain of $N = F_n$ sites, the degeneracy of the $E = 0$ level is given by the number of atoms F_{n-3}. The degeneracy of the $E = \pm t_B$ levels is given by the number of molecules F_{n-2} in the chain. For small nonzero $\rho \ll 1$, these three levels split into three clusters of levels, the molecular bonding $(+m)$ and antibonding $(-m)$ bands and the atomic (0) cluster. The separations between these three clusters for small ρ are roughly t_B. In perturbation theory, the three clusters do not mix and can be treated as three independent systems for the calculation of the effective Hamiltonians.

Molecular RG.—Consider the Hamiltonian H for a Fibonacci chain of length F_n and consider the lowest molecular bonding level located at the energy $-t_B$ and having a wave function that is nonzero on the molecule sites. It is easy to check to see that the chain formed by molecules is precisely the $(n-2)$th approximant chain. It can be shown using degenerate perturbation theory (Kalugin, Kitaev, and Levitov, 1986; Niu and Nori, 1986, 1990) that, up to an overall constant shift, the new effective Hamiltonian H' is again a Fibonacci hopping Hamiltonian, with the renormalized hopping amplitudes t'_A and t'_B. The old chain and the new chain after decimation of atoms are indicated in Fig. 17, along with the two new hopping amplitudes. The renormalized hopping amplitudes are given to lowest order in ρ by

$$t'_A = z t_A, \qquad t'_B = z t_B, \tag{43}$$

where $z = \rho/2$. Note that the hopping ratio is unchanged to lowest order under RG, as the new weak and strong hopping amplitudes satisfy $t'_A/t'_B = \rho' = \rho$. To summarize, the effective Hamiltonian for the bonding set of levels is, up to a global shift, that of the $n-2$ approximant chain with renormalized hoppings. The original level located at $E = -t_B$ is split into three levels, which can be labeled $-+$, -0, and $--$, separated by gaps of width t'_B.

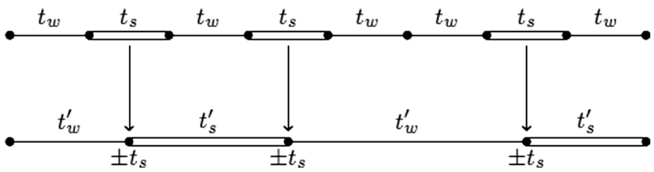

FIG. 17. Illustration of the molecular deflation rule: the fifth approximant is transformed to the third. From Macé, Jagannathan, and Piéchon, 2016.

A similar analysis shows that the effective Hamiltonian for the antibonding levels "+" is a FC identical to F_{n-2} sites with hopping amplitudes given by $t'_A = z t_A$ (weak) and $t'_B = -z t_B$ (strong). The original level located at $E = -t_B$ is split into three levels, labeled $++$ $+0$ and $+-$.

Atomic RG.—Consider the central band located around $E = 0$. The levels around $E = 0$ correspond to the wave functions that are the largest on the atom sites, of which there are F_{n-3}. It is easy to ensure that the new chain formed by these atom sites is simply the $(n-3)$th approximant chain. Degenerate perturbation theory shows that the effective Hamiltonian H' depends on two new renormalized hopping amplitudes. Figure 18 shows the old chain and the new chain obtained after a decimation of atoms, along with the two new hopping amplitudes. The new strong and weak bonds t''_A and t''_B are given to lowest order in ρ by

$$t''_A = \bar{z} t_A, \qquad t''_B = \bar{z} t_B, \tag{44}$$

where $\bar{z} = \rho^2$. As for the molecular RG, the hopping ratio is preserved since the new weak and strong hopping amplitudes satisfy $\rho'' = t''_A/t''_B = \rho$. To summarize, the effective Hamiltonian for the atom set of levels is the Hamiltonian of a chain of F_{n-3} sites and with renormalized hoppings. The original level is therefore split into three levels, labeled $0+$, 00, and $0-$. These are separated by gaps of width t''_B.

This process can be repeated until one reaches the three first chains. The result for the clustering structure is a succession of trifurcations, as illustrated in Fig. 19(a). One can reverse the process, alternatively, and track each band as it splits into three subbands when n increases by 2 or 3. Doing this, one sees that each of the F_n levels of the spectrum follows a unique path under successive renormalizations (termed the

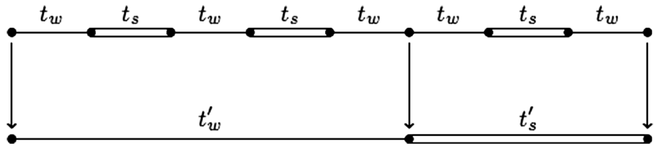

FIG. 18. Illustration of the atomic deflation rule: here the fifth approximant is transformed to the second. From Macé, Jagannathan, and Piéchon, 2016.

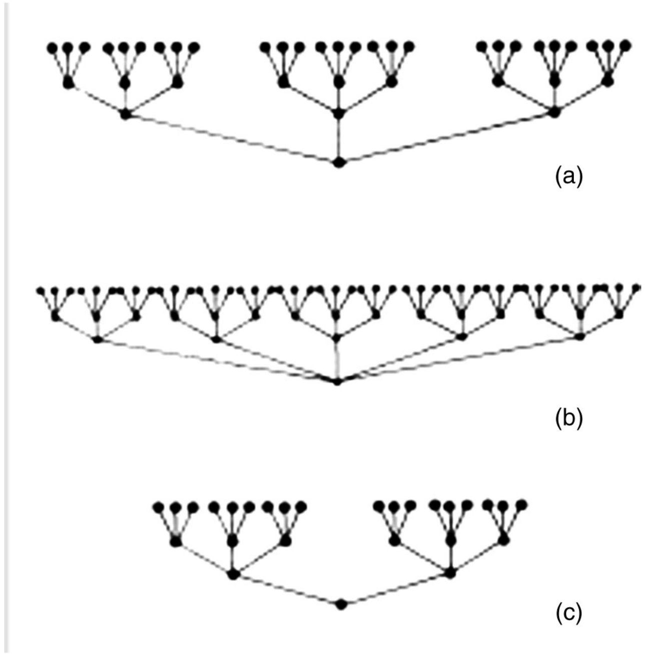

FIG. 19. Clustering and subclustering structures for the three different models described in Sec. IV. From Niu and Nori, 1990.

renormalization path) of the form $\{c_1c_2c_3\ldots\}$, where c_i can take the three values $0, \pm 1$. Note that this trifurcation scheme also holds for the critical AAH model (Hiramoto and Kohmoto, 1989).

RG for off-diagonal model (2).—Consider the FC in which the strong bond corresponds to A bonds. One can again assume, as in the preceding model, that the amplitudes are positive, without loss of generality, with $t_A \ll t_B$. The perturbation theory is now carried out in powers of t_B/t_A. Inspection of the FC shows that in the limit $t_B = 0$ the chain breaks up into diatomic and triatomic molecules. These molecules give rise to five energy levels $E/t_A = \pm\sqrt{2}, \pm 1, 0$. It can be shown that the new effective Hamiltonians within each of the five bands is a Fibonacci hopping Hamiltonian (Niu and Nori, 1990) of the type discussed previously for the off-diagonal model (1). Thus, each of the five levels trifurcates, and continue thereafter to trifurcate under successive RG steps. This is illustrated in Fig. 19(b).

RG for diagonal model.—For the diagonal model [Eq. (14)], a perturbation theory in $t/(\epsilon_A - \epsilon_B)$ once again shows the recursive structure of the energy spectrum. For $t = 0$, one has two isolated levels, $E = \epsilon_A$ (degeneracy F_{n-1}) and $E = \epsilon_B$ (degeneracy F_{n-2}). For small nonzero t, one can compute the new effective Hamiltonians in perturbation theory. It is found that these are given by two hopping parameters, one strong and one weak. Thus, after one RG step we are led back to the Fibonacci hopping model, leading to a splitting into three levels, and thereafter, with each successive RG step, trifurcations. This is illustrated in Fig. 19(c).

V. MULTIFRACTAL SPECTRUM AND STATES OF THE OFF-DIAGONAL MODEL

In this section we review the use of the previously described perturbative RG method to obtain a variety of multifractal properties of the diagonal (pure-hopping) model. Section V.A shows how the RG methods introduced in Sec. IV.B can be applied to this case to compute spectral properties as done by Zheng (1987) and Piéchon, Benakli, and Jagannathan (1995). Gap structures are taken up in Sec. V.B. Wave functions are considered in Sec. V.C.

A. Multifractality of the energy spectrum

The approximate RG method described in Sec. IV.B showed that the spectrum of a chain of number of sites equal to F_n can be mapped, after one RG step, to the spectra of two shorter chains F_{n-2} and F_{n-3}. We now apply this to obtain quantitative information on the spectral properties, following Zheng (1987) and Piéchon, Benakli, and Jagannathan (1995). The perturbative RG transformation can be formally written as

$$H_n = \underbrace{(zH_{n-2} - t_s)}_{\text{bonding levels}} \oplus \underbrace{(\bar{z}H_{n-3})}_{\text{atomic levels}} \oplus \underbrace{(zH_{n-2} + t_s)}_{\text{antibonding levels}} + \mathcal{O}(\rho^4) \tag{45}$$

to lowest order in ρ. Thus, given the first three spectra $W^{(n)}$ corresponding to $n = 0, 1, 2$, one can construct all the $(n > 2)$ th generation spectra. The spectra of the first three chains are simple to obtain. For $n = 0$ and 1, the approximant chains have only one hopping amplitude (t_B or t_A). Applying periodic boundary conditions the spectrum for $n = 0$ is the band $-2t_B < E < t_B$, with a bandwidth of $\Delta^{(0)} = 2t_B$. The spectrum of the $n = 1$ chain is a narrower band $-2t_A < E < t_A$. The $n = 2$ chain is an alternating sequence of t_A and t_B; thus, the spectrum has two bands separated by a gap, as shown in Fig. 20. One can now proceed to construct the spectrum for $n = 3$. $W^{(3)}$ is composed of two (bonding and antibonding) lateral bands and one central (atom) band. The sidebands are simply $W^{(1)}$ multiplied by the factor z and translated in energy by $\pm t_B$. The central band is $W^{(0)}$ multiplied by the factor $\bar{z}$. This procedure can be used to construct all the spectra shown in Fig. 20.

In each RG step, the bandwidths are reduced by the factor z or $\bar{z}$. The resulting bandwidth Δ of a given level in the nth approximant depends on the sequence of RG steps that were taken. A simple example is the two bands at the top and bottom edges of the spectrum, which always remain molecular throughout successive RG transformations. They have the RG paths $111\ldots$ and $\bar{1}\,\bar{1}\,\bar{1}\ldots$ having $\sim n/2$ steps. Thus, the bandwidth of the first level and its scaling exponent α_{edge}, defined through $\Delta_{\text{edge}} \sim F_n^{-1/\alpha} = \omega^{n/\alpha}$, are given by

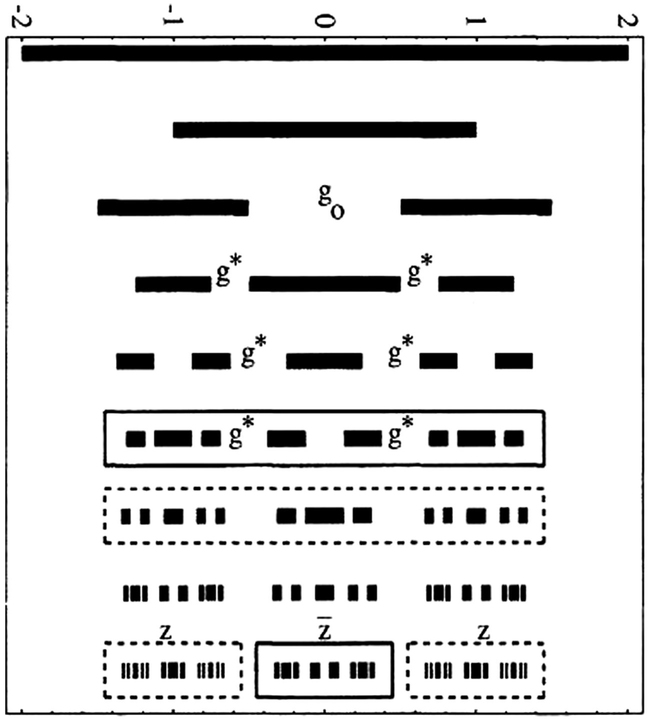

FIG. 20. Schematic view of the recursive construction of spectra using RG. The first three spectra for $n = 1, 2$ (single band) and $n = 3$ (two bands) are shown at the top. The nth spectrum is obtained by the union of the $(n-2)$th and $(n-3)$th spectra multiplied by the RG factors z and $\bar{z}$ and shifted as described in Eq. (45). The labels g_0 and g^* refer to transient and stable gaps (see the text). From Piéchon, Benakli, and Jagannathan, 1995.

$$\Delta_{\text{edge}} = z^{n/2} t_A,$$
$$\alpha_{\text{edge}} = \log(\omega^2)/\log(z) \tag{46}$$

to lowest order in ρ. The second simple case concerns the atomic level at $E = 0$, which has a RG path of 000… having $n/3$ steps (taking n as a multiple of 3). Thus, its bandwidth and its scaling exponent α_{ctr} are given by

$$\Delta_{\text{ctr}} = \bar{z}^{n/3} t_A,$$
$$\alpha_{\text{ctr}} = \log(\omega^3)/\log(\bar{z}). \tag{47}$$

Upon making a comparison with the exact results of Kohmoto, Sutherland, and Tang (1987) for the two exponents obtained using the trace map, one sees that these values of α represent the first terms of an expansion in ρ. Other levels have a mixture of atomic and molecular RG, so the scaling is given in general by $z^{n_m} \bar{z}^{n_a}$, where n_m (n_a) is the number of molecular (atomic) RG steps in its RG path. These numbers are not independent, as they must satisfy the condition $n \sim 2n_m + 3n_a$. It is useful now to introduce the variable $x = n_m/n$ as a measure of the degree to which a given RG path has molecular character. For long chains, x is a continuous variable in the interval $(0, 1/2)$. The smallest value of a purely atom state $(x = 0)$ corresponds to the energy in the middle of the spectrum. The maximum value $(x = 1/2)$ corresponds to the levels at band edges that are molecular states at every stage of the RG. Figure 21 shows the values of x versus the level index for the $n = 12$ approximant. Note that in general many different levels can share a given value of $x \neq 0$, whereas the value $x = 0$ corresponds to a single state that occurs only in every third chain (n is a multiple of 3).

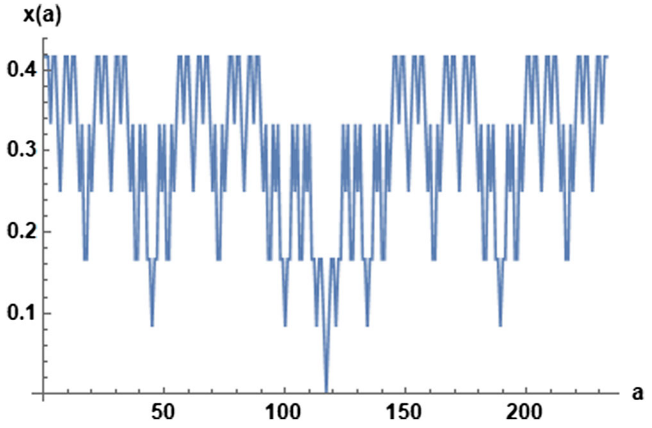

FIG. 21. $x(a)$ vs the level index a for each of the energy levels E_a of the $n = 12$ chain. Lines are drawn as a guide for the eye.

The exponent α can be computed for a given value of x and is given by

$$\begin{aligned}\alpha &= -\frac{\log F_n}{\log \Delta} \\ &= \frac{n \log \omega}{(n_m \log z + n_a \log \bar{z})} \\ &= \frac{\log \omega}{x \log z/\bar{z}^{2/3} + \log \bar{z}^{1/3}}.\end{aligned} \tag{48}$$

Let the number of levels scaling with a power α be $N \sim F_n^{f(\alpha)}$, thus defining the function $f(\alpha)$. This is simply the number of levels corresponding to a given value of n_a and n_m, which is $2^{n_m} n_m!/(n_m + n_a)!$. With the use of Stirling's approximation this leads to $N(x) \sim F_n^{g(x)}$, with

$$\begin{aligned}g(x) = \frac{1}{\log \omega}\bigg(&\frac{x}{2}\log 3x + \frac{1+x}{3}\log(1+x) \\ &+ \frac{1-2x}{3}\log(1-2x)\bigg).\end{aligned} \tag{49}$$

Equations (48) and (49) determine the function $f(\alpha)$ and describe the multifractal scaling of the spectrum. The exponent for any band can be computed if its RG path is specified. The expressions for α_{ctr} and α_{edge} are the leading terms in an expansion in small ρ of the exact formulas (31) and (32) obtained by Kohmoto, Sutherland, and Tang (1987). We note finally that according to the results in Eqs. (48) and (49) there is a special point at which $\rho = 1/8$. At this point $z = \bar{z}^{2/3}$, and the spectrum becomes monofractal because all bands scale in the same way according to our perturbation theory. However, in fact, as we mentioned in the discussion at the end of Sec. III.D, the exact results show that the spectrum is not monofractal for any ρ. Higher order terms must be considered in order to resolve the apparent discrepancy. A similar observation holds for the wave functions (Sec. III.C), where the lowest order calculation yields an ordinary fractal, with multifractality appearing only at the next order in the perturbative RG.

The scaling of the total bandwidth, $B^{(n)} = \sum_j^{F_n} \Delta_j^{(n)}$, with the system size can now be determined. From Eq. (45), one can deduce a recursion equation relating the total bandwidth of the nth chain to those of the $n-2$ and $n-3$ chains as follows:

$$B^{(n)} = 2zB^{(n-2)} + \bar{z}B^{(n-3)}. \tag{50}$$

Defining the exponent b by $B^{(n)} \sim F_n^{-b}$ for large n, from Eq. (50) one sees that b must satisfy the equation

$$1 = 2z\omega^{-2b} + \bar{z}\omega^{-3b}. \tag{51}$$

Recursive relations can be written likewise for all of the moments of the density of states (i.e., the inverse bandwidth Δ_j^{-1}). Recall that the generalized dimensions for the spectrum are the exponents corresponding to the qth moment of the DOS. Following the thermodynamical formalism introduced before, one defines the partition function $\Gamma^{(n)}(q,\tau) = F_n{}^{-q} \sum_j^{F_n} \Delta_j^{-\tau}$, where $\tau_q = D_q(q-1)$. This partition function obeys the recursion relation

$$\Gamma^{(n)}(q,\tau) = 2\frac{\omega_n^{2q}}{z^\tau}\Gamma^{(n-2)}(q,\tau) + \frac{\omega_n^{3q}}{\bar{z}^\tau}\Gamma^{(n-3)}(q,\tau). \tag{52}$$

For each q, the corresponding τ value is obtained by requiring Γ to be stationary. This results in the condition

$$1 = 2\omega^{2q}z^{(1-q)D_q} + \omega^{3q}\bar{z}^{(1-q)D_q}. \tag{53}$$

Relations for generalized dimensions.—The Hausdorff dimension D_F of the spectrum is given by D_0, which satisfies the equation

$$2z^{D_F} + \bar{z}^{D_F} = 1. \tag{54}$$

Although derived in the limit of small values $\rho \ll 1$, Eq. (54) nevertheless gives a rather good value even for relatively large values of ρ: one obtains $D_F = 0.76$ for $\rho = 0.5$.[5] The information dimension D_1 enters in an inequality for the diffusion exponent, which is discussed in Sec. VI.A. The exponent D_2 is also of special interest, in particular, for dynamics, as is also shown in Sec. VI.A. One sees in Eqs. (53) and (51) that the bandwidth exponent b is related to the D_q via $D_\delta = 1/(1+\delta)$.

FIG. 22. Recursive construction of the spectra of approximant chains showing the gap structure. Labels display the values of **q** determined according to Eq. (20) in red for transient gaps and in black for stable gaps (overbars indicate a negative sign). From Macé, Jagannathan, and Piéchon (2017).

B. Gaps, stable gaps, and topological numbers

In the construction of spectra with the RG recursion scheme, it becomes apparent that two kinds of gaps appear in the spectra of approximant chains: transient gaps and stable gaps. To understand these notions consider the spectra of the first few approximants shown in Fig. 20: one sees that the spectrum for $n=2$ has a gap labeled g_0 that disappears for $n=3$ and 4, reappears as a smaller gap for $n=5$, and goes to zero as n tends to infinity. This is an example of a so-called transient gap. Stable gaps are descendants of the gaps marked g^* whose widths remain finite. Writing recursion relations for the stable gap distribution $P(g)$, one can show that it has a power-law form

$$P(g) \sim g^{-(1+D_F)}. \tag{55}$$

The limiting value as n tends to infinity of the two main gaps g^* and the width of the spectrum Δ^* have also been computed in terms of ρ; see Piéchon, Benakli, and Jagannathan (1995) for details.

Gap labeling.—Given the recursive structure of the spectrum, it is easy to determine the labels for each of the gaps of the system for the $N = F_n$ levels. For the jth plateau of the IDOS $N(E) = N_j/N$, one must solve the relation $N_j = \mathrm{mod}[\mathbf{q}F_{n-1}, F_n]$ to obtain $\mathbf{q}$. Stable gaps and transient gaps are indicated by different colors for their $\mathbf{q}$ labels in Fig. 22 (black for stable and red for transient). Stable gaps have the lowest values of $\mathbf{q}$, and these are stable gap labels regardless of system size. In contrast, transient gaps have large values of $\mathbf{q}$ that depend on the system size, and these gaps vanish in the infinite size limit.

The gap widths tend to decrease with $\mathbf{q}$, although not monotonically. This is shown in Fig. 23, which provides the result of gap widths plotted against $\mathbf{q}$ for the $n=16$ approximant. These were computed for the pure-hopping model using an approximate renormalization group, as

---

[5] Strictly speaking, this approach is valid only for strong quasiperiodic modulations. However, these results remain pertinent even for moderate to weak quasiperiodicity, and calculations on finite chains show that when the gaps are opened they persist for all ρ, closing only in the periodic case.

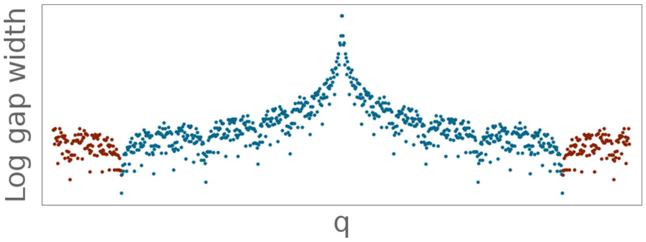

FIG. 23. Gap widths on a log scale vs the topological index **q** for the $n = 16$ approximant in the off-diagonal model. Red (darker gray) data points stand for transient gaps (see the text). From Macé, Jagannathan, and Piéchon, 2017.

outlined in Sec. IV. The black (red) data points correspond to stable (transient) gaps [these are gaps that tend to finite (zero) width as n tends to infinity]. The gap widths have log-periodic oscillations in **q**, and one sees a self-similar structure. Note that the smallest values of **q** up to a certain maximum correspond to stable gaps. For **q** above a certain value, there are only transient gaps.

C. Multifractality of wave functions

The RG construction of the energy spectrum in Sec. V.A has its parallel for the construction of wave functions, as was noticed by Niu and Nori (1986). Consider the wave function $\psi(E)$ for an allowed energy E. If the energy is located in a sideband, the support of $\psi(E)$ is concentrated on the molecular sites. If the energy is located in the middle band, the support of $\psi(E)$ is concentrated on atom sites. Under RG, the initial chain is transformed to a shorter chain, and the site i maps to site i' of the new chain. One can introduce, as we did for the energy recursion relations, wave-function renormalization factors λ and $\bar{\lambda}$ and write

$$\begin{aligned} |\psi_i^{(n)}(E)|^2 &= \bar{\lambda}|\psi_{i'}^{(n-3)}(E')|^2 \quad \text{if } E \text{ is atomic}, \\ |\psi_{l,r}^{(n)}(E)|^2 &= \lambda|\psi_{i'}^{(n-2)}(E')|^2 \quad \text{if } E \text{ is molecular}, \end{aligned} \tag{56}$$

where E' denotes the energy after renormalization. In the case of molecular RG (second line), there are two sites l (left) and r (right) forming the molecule corresponding to the site i'. The wave-function renormalization factors are given by $\lambda \approx 1/2$ and $\bar{\lambda} \approx 1$, to lowest order in ρ. The higher order corrections are important to keep for a correct description of multifractality, as shown by Macé, Jagannathan, and Piéchon (2016). Given the RG path of a state, with the help of Eqs. (56) one can reconstruct the corresponding $\psi(E)$.

To illustrate the different structures that are obtained, we now consider some examples. The RG path of the lowest level of the spectrum is $\{1111\ldots\}$, and the wave function constructed recursively has the largest amplitudes on pairs of sites that derive from molecules on a larger length scale, which derive from still larger molecules, etc. Figure 24(a) shows the wave function for a chain of 144 sites ($n = 11$) that were computed numerically for a value of $\rho = 0.2$. One sees here the characteristic double peak composed of double-peak structure on several scales. The figure shows deviations from the RG construction that we outlined: there are, for example, small peaks that we ignored in our lowest order approximation. There are asymmetries in the amplitudes of the double peaks. These are due to higher order terms in ρ, which in our example is not particularly small. Figure 24(b) shows the wave function in the same chain for the energy $E = 0$, whose RG path is $\{0, 0, 0, \ldots\}$. The peaks this time are primarily localized on two atom sites. Finally, Fig. 24(c) shows an example of a randomly chosen mixed wave function that has both atomic and molecular components in its construction.

Hamiltonian in the conumber basis.—In preparation for the discussion of wave functions, we first discuss the representation of the Hamiltonian in the conumbering basis introduced in Sec. II.B.3. In this basis, the hopping Hamiltonian takes the form of a Töplitz matrix, where the nonzero elements lie at distances of F_{n-2} and F_{n-1} from the principal diagonal (Sire and Mosseri, 1990). For example, the Hamiltonian for the $n = 5$ chain ($N_n = 8$) can be written as follows:

$$H = \begin{bmatrix} \cdot & \cdot & \cdot & t_A & \cdot & t_B & \cdot & \cdot \\ \cdot & \cdot & \cdot & \cdot & t_A & \cdot & t_B & \cdot \\ \cdot & \cdot & \cdot & \cdot & \cdot & .t_A & \cdot & t_B \\ t_A & \cdot & \cdot & \cdot & \cdot & \cdot & t_A & \cdot \\ \cdot & t_A & \cdot & \cdot & \cdot & \cdot & \cdot & t_A \\ t_B. & \cdot & t_A & \cdot & \cdot & \cdot & \cdot & \cdot \\ \cdot & t_B. & \cdot & t_A & \cdot & \cdot & \cdot & \cdot \\ \cdot & \cdot & t_B. & \cdot & t_A & \cdot & \cdot & \cdot \end{bmatrix}.$$

As can be read off directly from the matrix, sites numbered 1–3 and 6–9 have a strong bond t_B and thus form molecules in

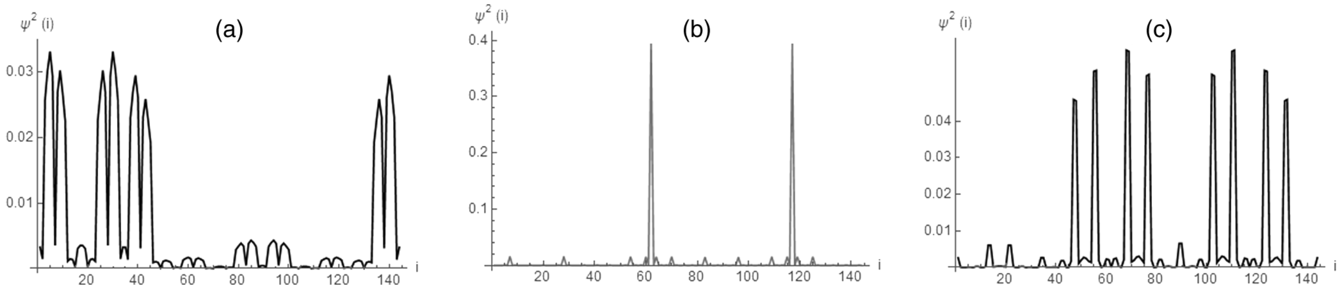

FIG. 24. (a) Ground state probabilities ψ_i^2 vs site index i. (b) $E = 0$ state probabilities ψ_i^2 vs site index i. (c) Probabilities ψ_i^2 vs site index i for state $a = 34$. The data were obtained by diagonalization for an $N = 144$ chain using periodic boundary conditions for $\rho = 0.2$.

the first RG step, while sites 4 and 5 have weak bonds to either side and are atom sites. Within the two groups of F_{n-2} molecular sites, under a second RG step one further has a subgrouping into F_{n-4} molecules and F_{n-5} atoms of "second generation." This subgrouping occurs in the middle block as well. The conumbering scheme thus automatically classifies sites according to the same rules as the band structure. This remark is important to the following discussion of wave functions.

Energy-position symmetry.—As we have discussed, the construction of states and of the spectrum follow the same schema. Classifying sites according to their conumber corresponds exactly to the way that energies are ordered. This leads to a noteworthy approximate symmetry between states and energies. The top panel of Fig. 25 shows an intensity plot of the numerically calculated values (for an 89-site chain with periodic boundary conditions) of $\psi(E_a)j^2$ plotted against the conumber j for each allowed energy E_a. The lower panel of Fig. 25 shows the result for the wave functions after four RG steps. The following two observations can be made: (i) the similarity of the RG-constructed and numerical data is manifest, and (ii) the figure shows a reflection symmetry with respect to the diagonal, i.e., if i and a represent the position and the energy, then

$$|\psi_{i,a}|^2 = |\psi_{a,i}|^2 \tag{57}$$

to lowest order in ρ. This striking symmetry between spatial and spectral variables holds for sufficiently small ρ.

Multifractal exponents for wave functions.—The recursion relations for wave functions are analogous to those presented for the spectrum. These relations involve the two different rescaling factors in the recursion formulas (λ and $\bar{\lambda}$). Thus, all the wave functions are multifractal, in the same way that the spectrum is multifractal due to the presence of two distinct shrinking factors (z and $\bar{z}$). We define the fractal dimensions $D^{\psi}{}_q$ for the wave function $\psi(E)$ by

$$\chi_q^n(E) = \sum_i |\psi_i^n(E)|^{2q} \sim \left(\frac{1}{F_n}\right)^{(q-1)D_q^{\psi}(E)}. \tag{58}$$

For $q = 2$ the quantity $\chi_2(E)$ is also termed the inverse participation ratio (IPR), well known in the literature of Anderson localization, where it serves as a diagnostic for the metal-insulator transition. For a given system size, the inverse of the IPR provides an indication of the spatial spread of the wave function. The scaling of the IPR as a function of the system size determines whether or not a state is localized. The exponent $D_2^{\psi}(E)$ is an often used indicator helping to locate the metal-insulator transition in the 3D Anderson model. Recall that the value $D_2^{\psi}(E) = 1$ indicates that the state E is extended, while $D_2^{\psi}(E) = 0$ characterizes a localized state. Intermediate values $0 < D_2^{\psi}(E) < 1$ are a signature of a critical state. Figure 26 shows the IPR computed numerically for $\rho = 0.5$ for the $n = 12$ approximant (blue curve). The gray curve is obtained by reflecting Fig. 21 with respect to a horizontal axis and translating up. The IPR curve clearly tracks the curve corresponding to inversed x values. This anticorrelation can be qualitatively explained for sufficiently small ρ by the observation that, first, molecular states are more delocalized (have a lower IPR) than atom states and, second, the number of molecular RG steps is given by the variable x. Therefore, the higher the x value, the lower the IPR of the state.

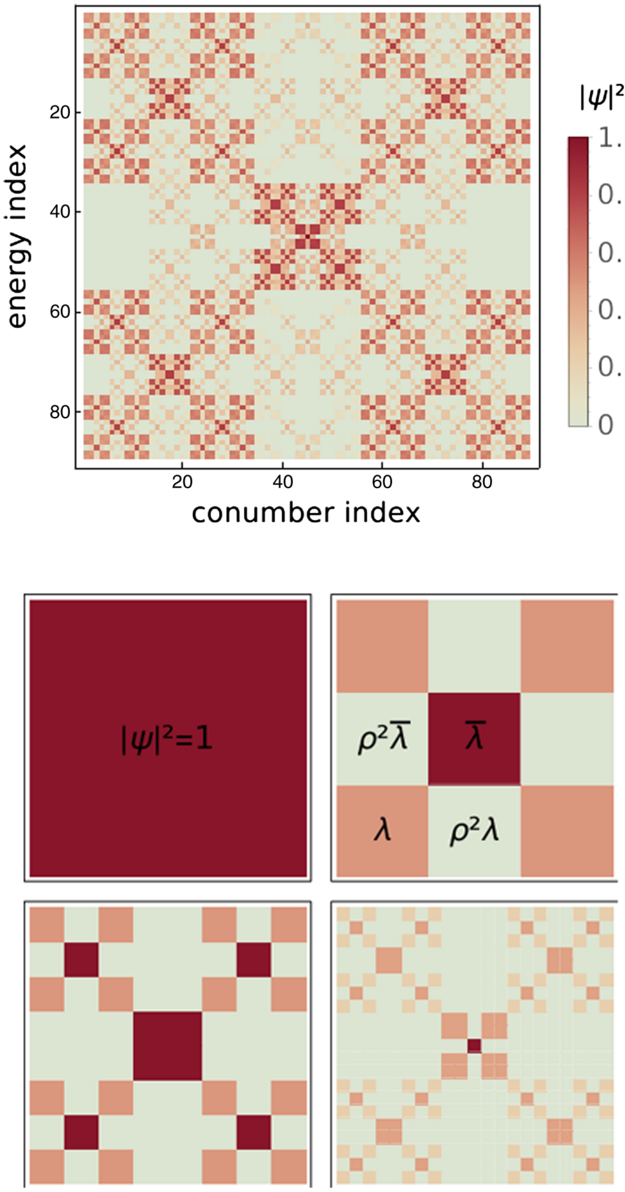

FIG. 25. Upper panel: the numerically computed intensity plot of wave functions for the $N = 89$ approximant. Intensities are shown for each of the sites in the conumber basis (x axis) and for every level (y axis). Lower panel: the first few steps of the geometrical construction of the wave functions according to perturbation theory [Eq. (56)]. Note the symmetry under reflection with respect to the diagonal, which holds only for our simplified RG treatment. From Macé, Jagannathan, and Piéchon, 2016.

On the quantitative level, the full set of exponents $D_q^{\psi}(E)$ can be computed in the perturbative RG scheme (Macé, Jagannathan, and Piéchon, 2016). To lowest order, these are given by the value of x (which measures the extent to which a given state is of the molecular type) as follows:

$$D_{q,0}^{\psi}(E) = -x(E)\frac{\log 2}{\log \omega} + \mathcal{O}(\rho^2). \tag{59}$$

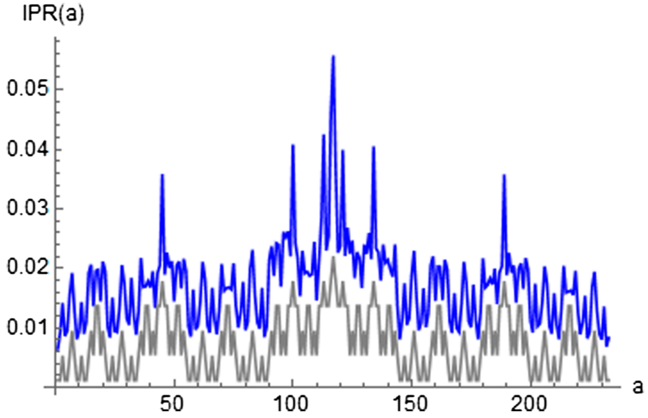

FIG. 26. Values of the IPR (χ_2) shown in blue (dark gray) computed for all states of the hopping model for an $n = 12$ chain ($\rho = 0.25$). The light gray line is obtained by reflecting the plot of x values shown in Fig. 21. An arbitrary scale factor and shift were applied to the gray curve to facilitate a comparison with the IPR.

This simple result for small ρ gives a monofractal since the fractal dimensions do not depend on q at leading order. For larger ρ, however, the higher order corrections show that the wave functions are indeed multifractal; see Macé, Jagannathan, and Piéchon (2016). For small ρ, Eq. (59) shows that the smaller the x, the smaller the fractal dimension.The most extended states according to Eq. (59) are those at the spectrum edges, where $x = 1/2$. Equation (59) also predicts that $D^{\psi}_{q,0}(E) = 0$ up to higher order corrections for the level in the center of the band where $x = 0$. This indicates that the state is localized or close to being localized. However, as the exact calculations in Sec. III.F showed, it is in fact a critical state. The discrepancy is corrected by including the higher order corrections, which are lacking in Eq. (59), as was shown by Macé, Jagannathan, and Piéchon (2016).

Spectrally averaged dimensions.—In certain contexts, one may need to know not the behavior of a single eigenstate but the average behavior of wave functions close to a certain energy (such as the Fermi energy). One may want to determine the average value of the fractal dimension $D^{\psi}_2(E)$ within some energy interval ΔE. This averaged exponent occurs in some rigorous inequalities for dynamical quantities, as described in Sec. VI.A. The averaged wave-function exponents could also be relevant for other physical properties, such as the Kondo screening of impurities. Averaged exponents $\bar{\Delta}^{\psi}_q$ (obtained by averaging over the entire spectrum) were computed by Macé, Jagannathan, and Piéchon (2016). These exponents can be calculated by considering a generalization of the χ_q function in Eq. (58) to include a sum over all energies. The results for the averaged dimensions $\bar{D}^{\psi}_2(E)$ for two different values of ρ are shown in Fig. 27 [from Macé, Jagannathan, and Piéchon (2016)].

VI. DYNAMICAL PROPERTIES

The quantum diffusion of a wave packet is determined by the spectral properties of the underlying Hamiltonian. Extended wave functions and continuous spectra typically lead to ballistic motion where the particle moves with a well-defined group velocity. Singular continuous spectra such as that of the FC result in more complex behaviors. Some of the characteristics of wave packet diffusion are discussed in this section.

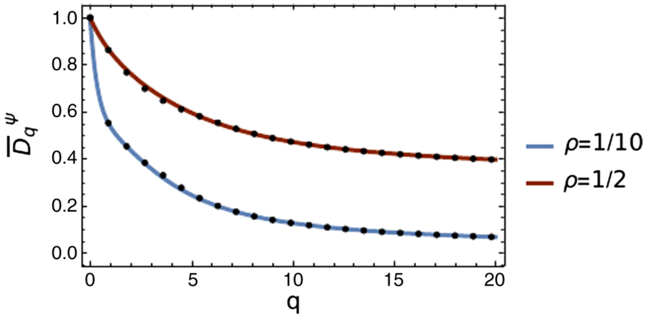

FIG. 27. The averaged fractal dimensions of the wave functions $\bar{D}^{\psi}_q$ as a function of q for $\rho = 0.1, 0.5$. Dots, numerical results; solid line, theoretical predictions. From Macé, Jagannathan, and Piéchon, 2016.

A. The diffusion exponent

The mean square displacement in a time t of an electron starting from the site i_0 of the chain is given by

$$d^2(i_0, t) = \sum_j (i - i_0)^2 p(i, i_0, t), \tag{60}$$

where $p(i, i_0, t)$ is the probability of being on site i at time t for a given starting position i_0, normalized such that $\sum_i p(i, i_0, t) = 1$. The time dependence of $d^2(i_0, t)$ is in principle extremely complex due to the multifractality of both the density of states and the wave functions. The exponent β, which can depend on the initial position i_0, describes its leading long time behavior after one smoothes out the fluctuations, i.e.,

$$d(i_0, t) \sim t^{\beta(i_0)} \tag{61}$$

for sufficiently long times t. In the simplest cases, values of the exponent are well known: for electrons in a periodic crystal there is ballistic propagation with a constant group velocity. The system has translational invariance and $\beta(i_0) = \beta$ regardless of the initial position. For localized electrons, $d(t)$ tends to a constant at long times and $\beta = 0$. For standard diffusion, as in the case of electrons in a moderately disordered crystal, $\beta = 1/2$.

For quasicrystals that are invariant under translations, the β values depend on the choice of origin i_0 of the wave packet. One can define an effective averaged diffusion exponent β by considering the averaged quantity $d(t) = \langle d(i_0, t) \rangle$, where the angle brackets denote the average over initial positions i_0. $d(t) \sim t^{\beta}$ defines the globally averaged value of the diffusion exponent β.

Numerical results for the values of β in the FC for different values of $w = t_A/t_B$ are shown as circular symbols in Fig. 28 [from Thiem and Schreiber (2013)]. One sees that the diffusion exponent increases in value monotonically with t_A/t_B and reaches the expected value of 1 in the limit of the periodic chain. Data for d-dimensional product lattices

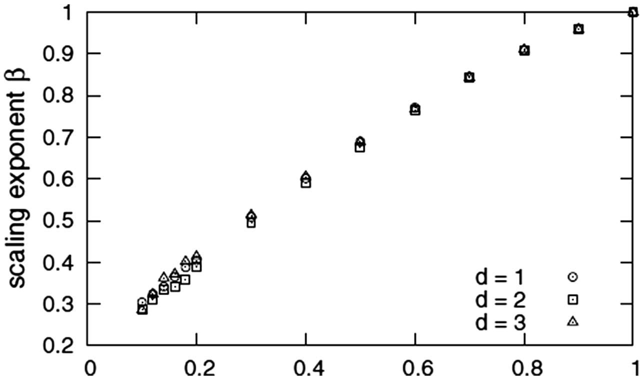

FIG. 28. Diffusion exponent β as a function of the hopping ratio for the Fibonacci chain and its d-dimensional generalizations, as described in Sec. X. From Thiem and Schreiber, 2012.

(see Sec. X) included in the figure show that the exponent β does not depend on the dimensionality in this class of models.

Note that this exponent enters into many phenomenological theories of transport in quasicrystals. From a dimensional analysis the diffusivity $D \sim d^2(\tau)/\tau$, as well as the conductivity σ that is proportional to D by the Einstein relation, should scale as $\tau^{2\beta-1}$, where τ is some characteristic cutoff time for diffusion. For subdiffusive motion, i.e., $\beta < 1/2$, the electrical conductivity σ would then decrease with increasing τ. This behavior is the opposite of what one would observe in metals, where conductivity increases linearly with τ according to the Drude formula. In real quasicrystals, experiments show that conductivity decreases when the structural quality of the sample is improved, for example, by annealing (Mayou *et al.*, 1993), which could be interpreted to mean that β is smaller than 1/2.

RG method for diffusion.—Studies of dynamics using the approximate RG scheme were carried out by Abe and Hiramoto (1987), Piéchon (1996), and Thiem and Schreiber (2012). These studies use a recursive approach to computing $d(i_0, t)$, as well as all of the generalized moments of the displacement,

$$d_q(i_0, t) = (1/N)\sum_j (i - i_0)^q p(i, i_0, t). \qquad (62)$$

To lowest order, one can write two different recursive relations for the probability $p^{(n)}$, depending on whether the initial site is an atomic or a molecular site. Following the approach used by Piéchon (1996), we label the initial site i_0 and have i refer to a site of the nth chain. In the renormalized chain, similarly, the initial site has the label i'_0 and i' refers to a site of the new chain; see Fig. 29. The length scale renormalization factor is either ω^3 or ω^2 depending on the type of RG transformation (atom or molecule), while the corresponding energy-time renormalization factors are z and $\bar{z}$. The relations between probabilities defined on the old and new chains can be stated as follows:

$$p^{(n)}(i, i_0, t)|_{\text{ato}} \approx \omega_n^3 p^{(n-3)}(i', i'_0, \bar{z}t),$$
$$p^{(n)}(i, i_0^{\pm}, t)|_{\text{mol}} \approx \omega_n^2 p^{(n-2)}(i', i'_0, zt). \qquad (63)$$

In the second relation of Eq. (63), the initial site in the case of the molecule is further labeled with a ± standing for the left and right atoms of that molecule. The first of these relations says that the probability to go from site i_0 to site i in a time t in the nth chain is reduced by a factor of ω^3 with respect to the probability to go from site i'_0 to site i' (a distance shorter by ω^3) in a time $\bar{z}t$ in the $(n-3)$th chain. For molecules, a similar statement applies, with the additional assumption that the left and right atoms play a symmetric role in the propagation.

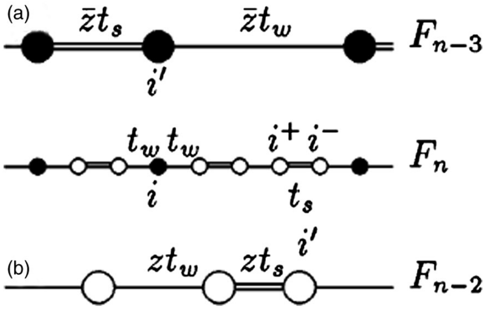

FIG. 29. (a) Relation between atom i of F_n and atom i' of F_{n-3}. (b) Relation between a molecule (i^+, i^-) of F_n and its corresponding site i' of F_{n-2}. t_s and t_w refer to t_B and t_A, respectively, in the notation used in this review. From Piéchon, 1996.

Note the following two simple extreme cases:

(1) If the origin of the wave packet is chosen such that one obtains a purely atomic-type diffusion at every RG step, then the result would be a power law $d(t) \sim t^{\beta_{\text{ato}}}$ with

$$\beta_{\text{ato}} = \ln \omega^3 / \ln \bar{z}.$$

(2) In the opposite situation of a pure molecular diffusion process, one obtains another exponent,

$$\beta_{\text{mol}} = \ln \omega^2 / \ln z.$$

Thiem and Schreiber (2013) defined an average value of β using the relative fraction of atom and molecular sites as follows:

$$\bar{\beta} = \frac{\tau - 1}{\tau + 1}\beta_{\text{ato}} + \frac{2}{\tau + 1}\beta_{\text{mol}}. \qquad (64)$$

They noted that this value fits the dynamics well for small ρ, up to about $\rho = 0.02$ (when the approximations made for the wave functions become inadequate).

Using the recursion relations in Eq. (63), Piéchon (1996) derived recursion formulas for the moments $d_q(i_0, t)$ and their averages $d_q(t) = \langle d_q(i_0, t)\rangle$ as follows:

$$d_q^n(t) = \omega_n^{3(1-q)} d_q^{n-3}(\bar{z}t) + 2\omega_n^{2(1-q)} d_q^{n-2}(zt). \qquad (65)$$

Suppose that there is a fixed point solution of the probability p^* in the limit $n \to \infty$. Equation (65) implies the following self-consistency condition:

$$p^*(r, t) = \omega^6 p^*(\omega^3 r, \bar{z}t) + 2\omega^4 p^*(\omega^2 r, zt). \qquad (66)$$

Note that the probability depends on two scaling factors leading to a multiscaling property: the function $p^*(r,t)$ cannot be written as a function of a single variable. Consider the probability $p(r=0,t)$. Letting $p(0,t)^* \sim t^{-\gamma}$ and comparing Eq. (66) to Eq. (53), one sees that $\gamma = D_2$, one of the spectral dimensions introduced earlier.

More generally, if one assumes that higher moments of the diffusion distance scale as $d_q(t) \sim t^{q\sigma_q}$, then one finds that $\sigma_q = D_{1-q}$. This result shows that the diffusion exponents $\sigma_q \geq D_1$, thus satisfying the Guarneri inequalities (Guarneri, 1993) for all values of q. This formalism and similar conclusions are applicable to other quasiperiodic chains such as the AAH model studied by Evangelou and Katsanos (1993) and Ketzmerick *et al.* (1997).

We saw in Sec. V.A that in perturbation theory the spectrum was approximately monofractal for $z = \bar{z}^{2/3}$. This simplification occurs for the wave packet dynamics as well: the exponent $\sigma_q = D_F$ for all q, where $D_F = \ln\omega^2/\ln z$. In this case, the dynamics can be expected to be simple diffusion with a single exponent. However, this is true only to the extent of the approximations made; see the caveat based on the trace map analysis Sec. III.

Exponent relations and inequalities.—Guarneri (1993) derived an inequality stating that $\beta \geq D_1$, where D_1 is the previously mentioned information dimension of the spectrum. Another inequality, derived by Ketzmerick *et al.* (1997), involves the average wave-function exponent D_2^ψ and states that $\beta \geq D_2/D_2^\psi$. Both these inequalities are satisfied in the FC, as can be seen in Fig. 30. For the diagonal Fibonacci model, Damanik (2006) and Damanik and Tcheremchantsev (2007) showed that β must satisfy certain bounds that depend on the on-site energies ϵ_A and ϵ_B.

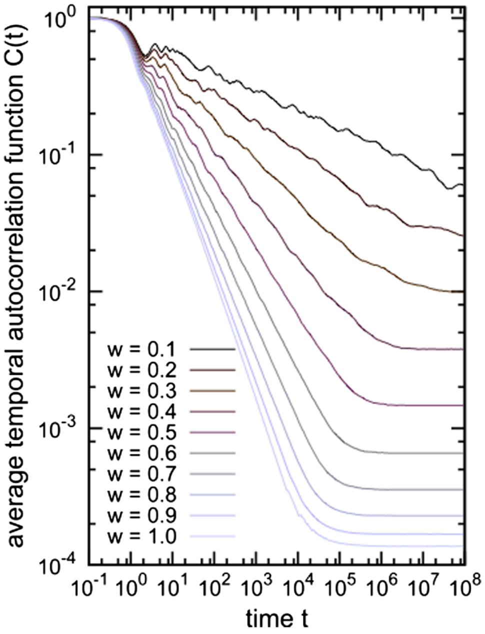

FIG. 31. Log-log plot of the smoothed autocorrelation function for different values of the hopping ratio ($w = t_A/t_B$) showing the fit to the power law. From Thiem and Schreiber, 2013.

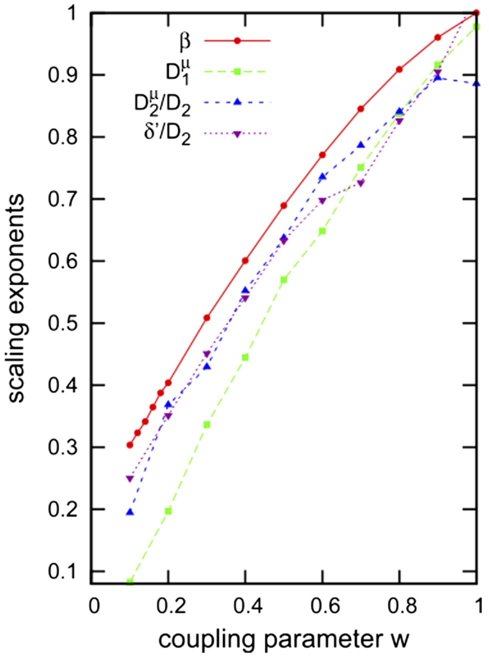

FIG. 30. Comparative plot of diffusion exponent and theoretical lower bounds involving generalized spectral dimensions and wave-function dimensions. Exponents were computed numerically for different values of the hopping ratio $w = t_A/t_B$. From Thiem and Schreiber, 2013.

B. Autocorrelation function

As for the mean square distance, the time-dependent correlation function in quantum systems with Cantor spectra is expected to have a power-law decay that falls off as $t^{-\delta}$ at long times. Ketzmerick, Petschel, and Geisel (1992) argued that the exponent δ should be equal to D_2. Ketzmerick, Petschel, and Geisel (1992), Zhong and Mosseri (1995), Thiem, Schreiber, and Grimm (2009), and Thiem and Schreiber (2012) studied the behavior of the smoothed autocorrelation function given by

$$C(i_0,t) = \frac{1}{t}\int_0^t P(i_0,i_0,t')dt', \tag{67}$$

which gives the integrated probability up to time t for the particle to be found at the initial position. Averaging over all initial positions, one obtains $C(t) = (1/N)\sum_i C(i,t) \sim t^{-\delta'}$. This quantity is easier to fit than the autocorrelation function. Note that δ' may be different from δ due to logarithmic corrections coming from the integral in Eq. (67). Figure 31, from Thiem and Schreiber (2013), shows the smoothed autocorrelation function for different values of t_A/t_B (the variable w in the figure). The exponent should tend to the expected value 1 in the periodic limit when the spectrum becomes continuous ($t_A = t_B$ or $\epsilon_A = \epsilon_B$).[6]

---

[6] In practice, however, as pointed out in by Yuan *et al.* (2000), it is hard to get convergence in numerical studies. Thus, some early numerical works obtained incorrect values that were smaller than the expected value of 1 for a periodic system.

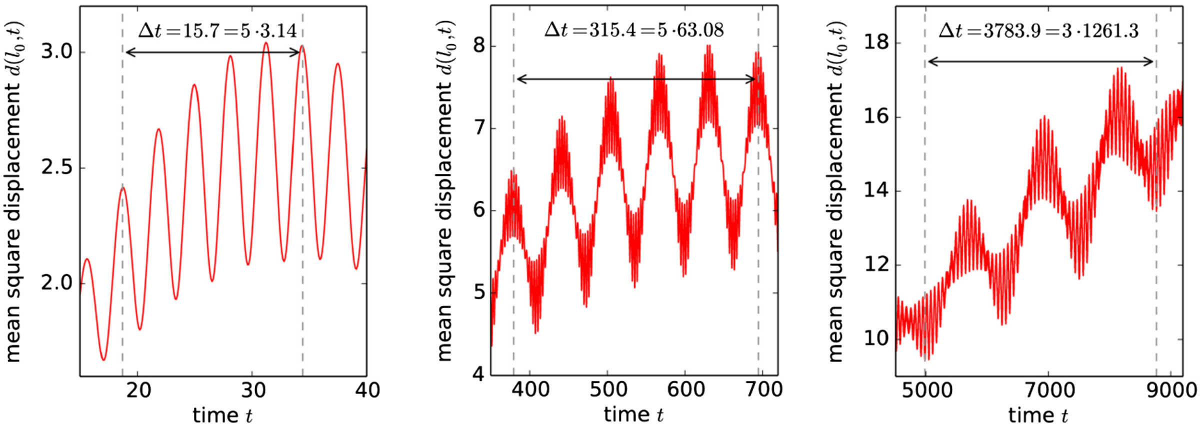

FIG. 32. Log-log plots of $d(t)$ vs time for short timescales (left panel) and intermediate timescales (center panel) showing the two shortest periods in the oscillations. A third period (right panel) governs still larger timescales. Data correspond to diffusion from a fixed molecular site of the $n = 14$ approximant chain, with $t_A = 0.1$ and $t_B = 1$. From Thiem, 2015.

C. Log-periodic oscillations

Abe and Hiramoto (1987) observed that there are oscillations superposed on top of the average power-law behavior of the rms distance $d(i_0, t)$. These oscillations were studied in more detail by Lifshitz and Even-Dar Mandel (2011). A similar oscillatory behavior is seen for the return probability $p(0, t)$. Figure 32, from Thiem (2015), shows $\ln d(t)$ plotted versus $\ln t/t_B$ for a wave packet diffusing from an initial site chosen to be of molecule type. The two shortest periods, corresponding to short times and intermediate times, can be clearly seen in these plots. The system size considered was large enough (an $n = 14$ approximant chain) that a third period was observed for even longer times; see Thiem (2015).

The empirical form that was used to fit these data is $d(i_0, t) \sim t^{\beta(i_0)}(1 + \alpha e^{if \ln t})$. The frequencies f are different, depending on the timescale that is considered, and they follow a hierarchical rule. The shortest times correspond to the fastest oscillations, and the frequency depends on the nature of the initial site i_0, i.e., whether it is an atom or a molecule. At the shortest timescale the oscillations have a period (in dimensionless units) of 2π for an initial site of the atom type, and π when the initial site is of the molecule type. Going to longer times the oscillations have frequencies that are smaller by factors of $\bar{z}$ and z, respectively. Thiem (2015) gave a quantitative account of these oscillations in terms of the perturbative RG theory and argued that they stem, at each length scale of the RG process, from resonances due to the molecular energy level splitting. Thiem (2015) noted that such oscillations are not observed for the quasiperiodic critical AAH model. This may be attributed to an essential difference between the two potentials: since the potential energy is a continuous-valued function in the AAH model, there are no molecular clusters in its RG scheme, and thus no characteristic resonance frequencies.

VII. TRANSPORT PROPERTIES

Some frequently asked questions concern the resistivity of a quasicrystal. Are these materials intrinsically metallic or insulating ? How does transport depend on the sample size, disorder, temperature, external magnetic fields, etc.? The following studies of transport properties of 1D Fibonacci chains attempt to shed light on these questions.

A. An exact result for $E = 0$ transmission

The $E = 0$ state transmission coefficient in the hopping model can be calculated from the exact solution given in Sec. III.F. This transmission coefficient is proportional to the zero temperature conductivity at half filling, when the Fermi energy of the system is $E_F = 0$. We now consider a FC of length $L = 2n$ attached to periodic chains (input and output chains) at either end. The transmission coefficient is given by (Economou and Soukoulis, 1981; Beenakker, 1997)

$$\mathcal{T}_n = \frac{4}{(x_n + x_n^{-1})^2}, \tag{68}$$

where $x_n = |\psi(2n)/\psi(0)|$. Using Eq. (37) one obtains (Macé et al., 2017)

$$\mathcal{T}_n = \frac{1}{\cosh^2\{\kappa[h(n) - h(0)]\}}, \tag{69}$$

where the height function h, it is recalled, depends solely on the geometry. Equation (69) shows that the transmission $\mathcal{T}_n = 1$ (there is perfect transmission) when the heights $h(n)$ and $h(0)$ are equal. This type of "intermittent" transparency occurs for sites separated by distances that can tend to infinity.

One can also compute the harmonic mean of the transmission over a chain of $L + 1$ sites. The harmonic mean, which is more adapted than the arithmetic mean for systems with large fluctuations, is defined by

$$\langle \mathcal{T} \rangle_L = \left(L^{-1} \sum_i^L \mathcal{T}_i^{-1} \right)^{-1}. \tag{70}$$

The scaling of $\langle \mathcal{T} \rangle_L$ with system size L can be expressed analytically using the height distribution in Eq. (38), which yields

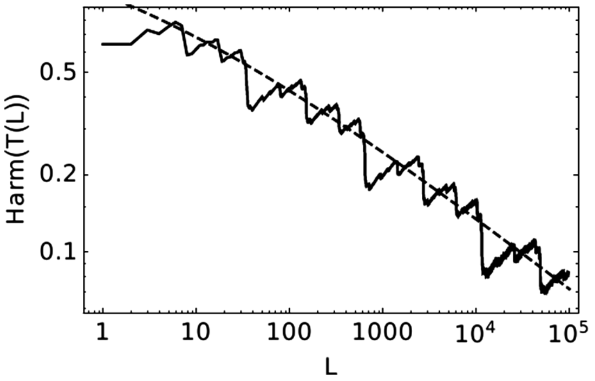

FIG. 33. Mean $E = 0$ transmission coefficient as a function of length L of the Fibonacci chain. The dashed and solid lines show the analytical prediction of Eq. (71) and numerical results for $n = 27$ ($N = 196\,418$ atoms), respectively. From Macé *et al.*, 2017.

$$\langle \mathcal{T} \rangle_L \sim 2\left(1 + \frac{L^{\phi}}{L_0}\right)^{-1}, \tag{71}$$

where the exponent ϕ can be expressed in terms of κ, the golden mean τ, and the maximal eigenvalue of a certain product of generalized inflation matrices; see Macé *et al.* (2017) for details. Equation (71) predicts a power-law decay of the mean transmission as a function of distance L, which is in accord with the numerical data, as seen in Fig. 33. Note that there is no contradiction between this power law and the fact that the chain can be transparent for long distances. The apparent paradox is explained by noting that the power law represents an average behavior, while for a given system there are large fluctuations around the mean [as observed by Sutherland and Kohmoto (1987)], whereas in a given chain, the transmission coefficient can be (and is) equal to 1 for certain sites.

B. Landauer approach

The Landauer formula relates the resistivity $\rho(n)$ to the transfer matrix T_n of a system of n sites as follows:

$$\rho_n = \tfrac{1}{4}(T_n^T T_n - 2), \tag{72}$$

where T^T denotes the transpose of the transfer matrix. Using the trace map techniques described in Sec. III, Sutherland and Kohmoto (1987) studied the behaviors near the band edge and the band center. They showed that the resistance grows no faster than a power law of the system size. They pointed out as well that there is a wide distribution of powers governing its growth with system size, and this leads to large fluctuations of the resistance. They speculated, finally, that this behavior is also qualitatively to be expected for other energies in the band. Their conjecture as to power-law behavior of the resistivity was proven by Iochum and Testard (1991).

For a comparison with measurements, it is pertinent to consider the average resistance where the average is taken over states lying within a certain energy interval. The energy interval chosen should depend on factors such as the temperature or the energy scale corresponding to inelastic scattering, disorder conditions, etc. For a system of length L and an appropriately chosen ΔE,

$$\bar{\rho}(L) = \frac{1}{n(E)\Delta E}\sum_E \rho(L, E_i) \tag{73}$$

defines an average resistance that was studied for the FC by Das Sarma and Xie (1988) using the Landauer formalism. The result is a power-law behavior for the resistivity, $\bar{\rho} \sim L^{-a}$. They noted that the power law holds for other fillings provided that the Fermi level is not close to a large gap.

C. Kubo-Greenwood approach

Sánchez *et al.* (2001) and Sánchez and Wang (2004) developed a RG approach for the conductivity starting with the following Kubo-Greenwood formula:

$$\sigma(\mu, \omega, T) = \frac{2e^2\hbar}{\pi m^2 V}\int dE \frac{f(E) - f(E + \hbar\omega)}{\hbar\omega} \times \mathrm{Tr}[\mathrm{Im}G^+(E + \hbar\omega)\mathrm{Im}G^+(E)], \tag{74}$$

where V is the volume of the system, $G^+(E)$ is the retarded one-particle Green's function, and f is the Fermi-Dirac distribution with Fermi energy μ for temperature T. Applying the RG method to the Kubo-Greenwood formula, Sánchez and Wang (2004) could study the ac and dc conductivities for large systems. In the hopping problem, for half filling, they found that the scaling exponents of the conductivity and the density of states have a similar dependence. Figure 34 shows the parameter b (defined by $\sigma \sim b^{-n/6}$) and the parameter d (defined by DOS $\sim d^{-n/6}$) plotted against t_A/t_B. They concluded that these results show the existence of an Einstein relation $\sigma \sim (dN/dE)D$, wherein the conductivity and density of states are related by the diffusivity D.

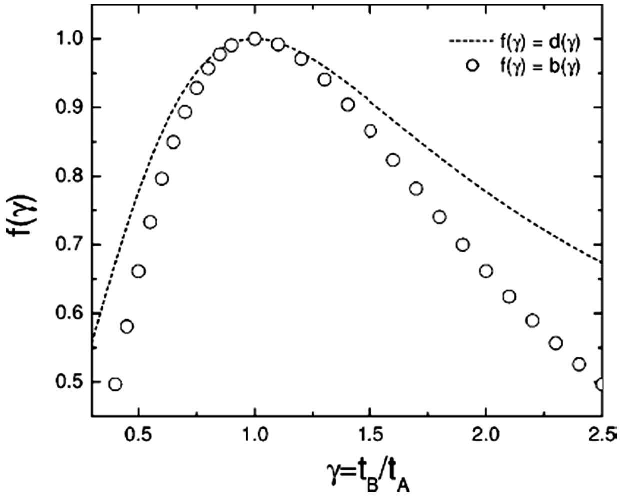

FIG. 34. The conductivity exponent b (circles; see the text for the definition) and the density of states exponent d [following the analytic formula given by Kohmoto, Sutherland, and Tang (1987); dashed line] as a function of the hopping ratio $\gamma = t_A/t_B$. From Sánchez and Wang, 2004.

D. Noninteracting many body metallic and insulating states

Even in the absence of electron-electron interactions, many body effects can play an important role in quasicrystals. Varma, Pilati, and Kravtsov (2016) considered such many body effects (which are due solely to the Pauli principle) on the conductance of Fibonacci chains. They computed the effective localization length Λ for various band fillings using a formalism developed by Kohn (1964) for his theory of the insulating state. This localization length, which is related to the real part of the conductivity tensor, is more sensitive to spectral gaps and to transport properties than the more familiar single-particle localization length defined in terms of the decay of the envelope of a given wave function. In a conductor this many body localization length scales to infinity, while in an insulator this quantity saturates with the system size. Varma, Pilati, and Kravtsov (2016) showed that in the hopping model there are special values of the band filling corresponding to an insulating state. These fillings correspond to values of the IDOS of ω^2, and the ω^3 values correspond to the positions of the large gaps. This is shown in Fig. 35, where Λ^{-2} is plotted versus the inverse system size $1/L$. The fillings 1/2 and 1/4 for which the trend is decreasing with increasing system size most likely correspond to a metallic state.

VIII. DISORDER AND BOUNDARY EFFECTS

Perturbations and their effects on critical states have been thoroughly discussed. The interesting conceptual problem raised has experimental implications. Disorder can be expected to play an important role in the electronic transport of real quasicrystals for the following reason. We saw in Sec. VII that, for a perfect FC, transport at $T = 0$ can be described by different power laws and can scale either toward an insulating state or to a metallic state in the thermodynamic limit, depending on the Fermi energy. Adding disorder of any form (be it structural defects or chemical substitutions or phonons) introduces a cutoff timescale τ whose value depends on disorder. One can therefore have a conductance that is finite in a quasicrystal that is weakly disordered. For increasing disorder, one would expect the quantum interference phenomena that lead, in a perfect quasicrystal, to the multifractality of the density of states and the multifractality of states to be progressively suppressed. Combined, these effects might contribute to improving transport as disorder increases; however, these are still open questions.

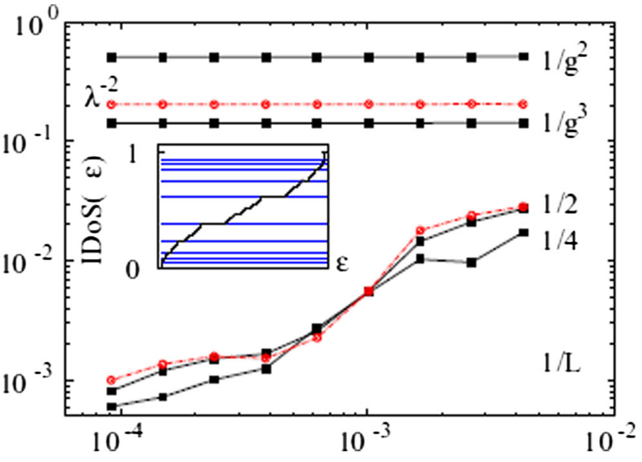

FIG. 35. Scalings of the many body localization length Λ with system size L for different band fillings. One sees a metallic trend (Λ decreasing with L) for fillings of 1/2 and 1/4, and an insulating behavior (Λ constant with L) for fillings g^{-2} and g^{-3}, where g is the golden mean. Red (gray) and black symbols correspond to curves for hopping ratios equal to 0.5 and ω, respectively. From Varma, Pilati, and Kravtsov, 2016.

The problem of a single impurity in a FC was studied by several researchers. The trace map method was used to compute localization lengths of an impurity state represented by a delta-function potential by Naumis (1999). The effect of structural defects, namely, a single phason defect (in which a pair of bonds is locally exchanged, as in the case of AB → BA), has been studied (Naumis and Aragón, 1996). This study concluded that the presence of a single impurity affects all of the states and leads to an increase of the fractal dimension of the spectrum. A weak form of structural disorder was considered by Velhinho and Pimentel (2000), who allowed randomness in the substitution rules for building chains. The conclusion reached in this and a later study (Huang and Huang, 2004) is that this type of disorder is irrelevant in that the Lyapunov exponents of states were not changed. To modify the critical states of the pure system, the disorder must break some symmetries of the Fibonacci Hamiltonian, as in the models that we discuss in Sec. VIII.A.

A. Finite systems and approach to Anderson localization

We now focus on the effects of adding a finite bulk disorder to the two models under discussion, Eqs. (13) and (14). General rigorous arguments show that in one-dimensional models an infinitesimal disorder leads to localized states (Delyon, Lévy, and Souillard, 1985). This has been confirmed in a variety of numerical studies (Liu and Riklund, 1987; Naumis, 1999). Das Sarma and Xie (1988) studied the effect of randomness in a Fibonacci quasicrystal using a scattering model for a system in which the scatterers of constant height were placed in a Fibonacci sequence of two distances a and b. The system was coupled to leads and conductance computed using the Landauer formula $G = [(2e^2/\hbar)T]/(1 - T)$, where T is the transmission coefficient of the F_n-site system. Das Sarma and Xie (1988) reported that, while disorder (in the positions of the scatterers) eventually localizes all states, small disorder does not change the physics qualitatively. Introducing a shuffling of the sequence of Kronig-Penney-type scatterers also leads to localization of states, and consequently to an exponential decay of the conductance.

There is no doubt that sufficiently large disorder strength leads to strong localization. However, the approach to localization can be complicated and state dependent. Jagannathan, Jeena, and Tarzia (2019) showed that there are interesting crossover phenomena going from the pure system to the localized system as the strength of disorder is increased. They studied the change of critical states of the pure-hopping model when hopping amplitudes are randomly perturbed from their initial values t_B and $t_A = \rho t_B$. While most states tend to

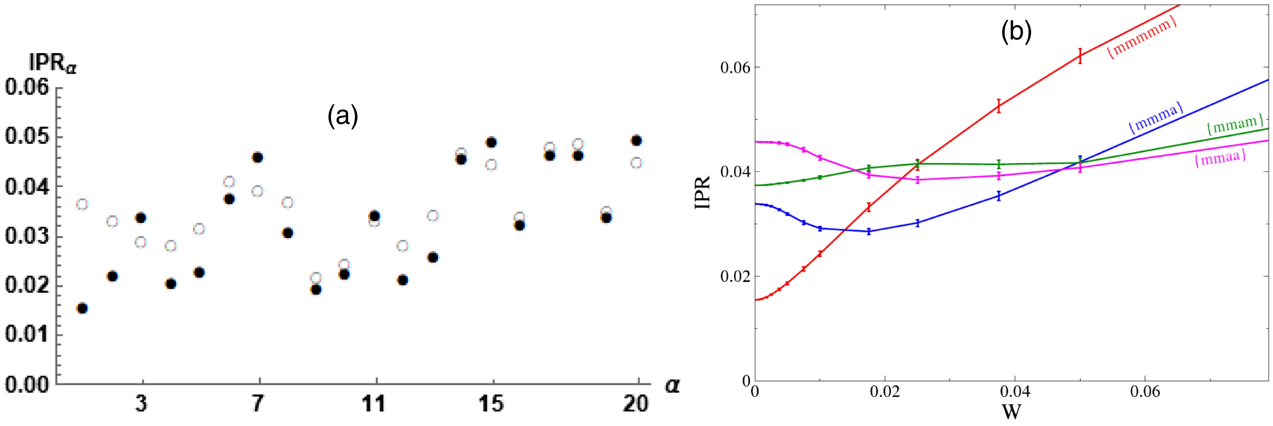

FIG. 36. (a) IPRs plotted for the lowest 20 states of an $n = 10$ Fibonacci chain for $\rho = 0.5$. Filled circles give IPR values of the pure chain, while open circles give the sample averaged IPR values for weak disorder ($W = 0.05t_B$). States with $\alpha = 3, 7, \ldots$ indicated are those showing an anomalous behavior. (b) The averaged IPRs vs disorder strength W for four low-lying states of an $n = 10$ approximant. The RG path is indicated next to each curve. From Jagannathan, Jeena, and Tarzia, 2019.

become more and more localized as the disorder strength is increased, some states go the other way initially, becoming delocalized before turning over and localizing like the other states. This is seen in Fig. 36(a), which shows the change of the IPR for the 20 lowest lying states $\alpha = 1, \ldots, 20$ of the $n = 10$ approximant taking a hopping ratio of 0.5. The IPR values for the pure chain are shown as filled circles, while the disorder averaged values for weak disorder $W = 0.05t$ are shown as open circles. It can be seen that, for most of the states, disorder results in increased IPR, as expected. However, some states behave anomalously: these states are indicated as $\alpha = 3, 7, 11, 15, \ldots$ in Fig. 36. The anomalous behavior is observed for an arbitrarily large system size, albeit for weaker disorder for longer approximants.

When the averaged IPR of each state is plotted versus disorder strength W, as shown for four low-lying states in Fig. 36(b), the anomalous states in Fig. 36(a) show a marked initial decrease of IPR followed by an upturn. The perturbative RG method provides an explanation of the observed behaviors in terms of the renormalization path of the states. Figure 36(b) shows the RG path of each of the states, and one sees that the band edge state $\alpha = 1$ (shown in red; RG path *mmmmm*) has a monotonic increase of the IPR. In contrast, the state $\alpha = 3$ (shown in blue; RG path *mmma*) has a minimum of the IPR: the state first delocalizes under weak disorder before the upturn sets in. One can show that the states that have "atomic" character in the final step of RG have such reentrant localization behavior and that they occur all through the spectrum. In simple terms, when using the picture for small values of ρ, the IPR for atomic states tends to decrease since disorder acts to "smear" the wave function onto neighboring sites. In contrast, for a wave function composed of molecular states, the change of IPR has the opposite sign; for details see Jagannathan and Tarzia (2020).

The changes in the IPRs can be described in terms of scaling functions: i.e., for a given state one can collapse the data for different system sizes L and different disorder strengths W onto a single curve. The finite size analysis given by Jagannathan, Jeena, and Tarzia (2019) showed that, despite their different approaches to localization, all states are described by a single critical exponent ν. The value of ϕ depends on the ratio t_A/t_B and was found numerically in finite size scaling plots such as those in Fig. 37: $\nu = 0.53$ for $\rho = 0.33$. The reentrant behavior of the IPR can be explained in terms of the perturbative RG theory; see Jagannathan, Jeena, and Tarzia (2019) and Jagannathan and Tarzia (2020) for details. However, the phenomenon seems to be more generic, and the reentrance behavior is observed for the diagonal model, as well as for other types of generalizations of the Hamiltonian.

B. The proximity effect

It is well known that it is possible to induce superconducting correlations in a noninteracting conducting system (N) by coupling it to a superconductor (S), the so-called proximity effect. The proximity effect provides a way to experimentally

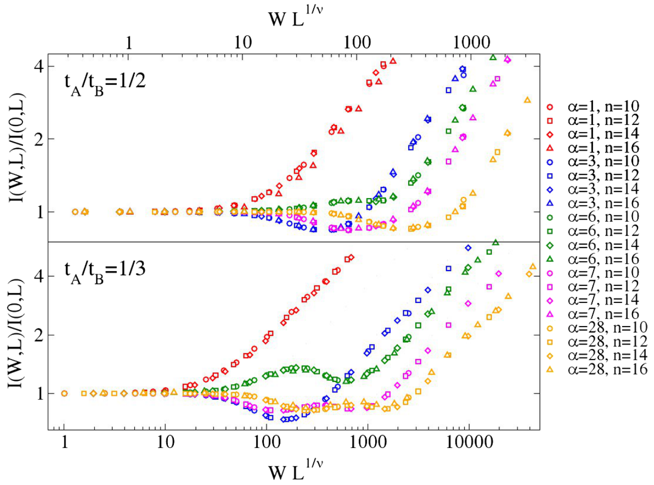

FIG. 37. Data for the normalized IPR of several low-lying states plotted vs the scaling variable $WL^{1/\nu}$ showing the data collapse for different disorder and system sizes. The two panels show results for two values of the hopping ratio t_A/t_B. Note the changes in the scaling functions, which are nonuniversal. From Jagannathan and Tarzia, 2020.

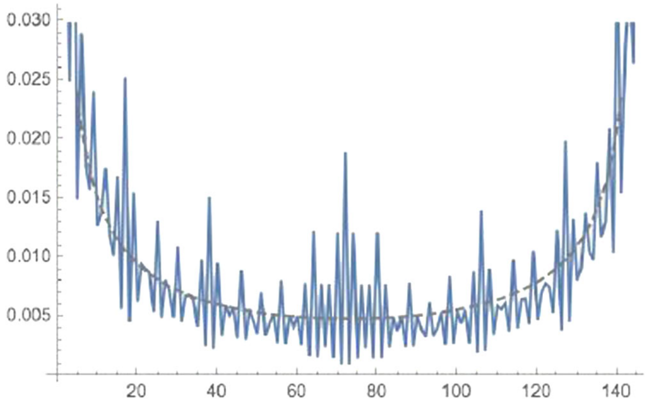

FIG. 38. The superconducting order parameter $\Delta(i)$ in a Fibonacci chain placed in contact with a BCS superconductor at both ends, plotted vs the position showing the power-law decay ($t_A/t_B = 0.8$; decay exponent = 0.6).

observe the unique properties of critical states in the FC. The first step consists of examining the proximity induced local pairing order parameter (OP) as a function of distance from the N-S interface.

Connecting the FC to a bulk superconductor and using a mean field theory, Rai, Haas, and Jagannathan (2019) computed the distribution of Δ_i, the induced local superconducting order parameter on site i. There are large spatial fluctuations of Δ_i that are due precisely to critical states. Figure 38 shows the profile of the OP as a function of the site number. One sees here the characteristic multifractal properties reflected in the variations of the order parameter. Fitting the average curve obtained by changing the phason angle parameter ϕ, one sees that the OP decays as a power law in the distance from the N-S interface (Rai, Haas, and Jagannathan, 2020). The power, which varies with t_A/t_B, is expected to depend on both the exponent of the density of states and the averaged fractal dimensions of the wave functions near the Fermi energy, here taken to be at $E = 0$.

Along with the other states, edge modes contribute to the induced order parameter on each site. In fact, if one cycles through chains as a function of the phason angle parameter ϕ in Eq. (11), the induced order parameter Δ_i at a given site oscillates and the periods are simply the topological numbers of gaps close to the Fermi energy (Rai, Haas, and Jagannathan, 2019). This is seen in Fig. 39, which shows the variations of the OP at the midpoint of the chain as a function of the phason angle ϕ. Two different chains are shown to emphasize that the basic periods do not change when going from smaller to larger systems: only additional periods appear. The left panel of Fig. 39 shows the power spectrum of the oscillations and the periods that are present in the curve of Δ_{mid}. One sees the periods 4, 17, 9, 21, and 6: these correspond precisely to the $\mathbf{q}$ values of the largest gaps near the Fermi energy, in this case those situated in the band center, $E_F = 0$.

IX. GENERALIZED FIBONACCI MODELS

A. Phonon models

Phonon modes in a quasiperiodic chain can be studied by considering the set of equations

$$H\psi_n = K_{n-1}\psi_{n-1} + K_n\psi_{n+1} - (K_{n-1} + K_n)\psi_n = E\psi_n, \tag{75}$$

where ψ_n denotes the displacement of atom n of mass m with respect to its equilibrium position and the couplings K_n can take one of two values K_A or K_B. One can consider, alternatively, another version of the model in which the masses m can vary and the couplings are constant. The operator H generalizes the discretized Laplacian operator, and its eigenvalues yield the frequencies of phonon modes. The phonon problem is tackled using methods that we have already seen for the closely related electron problem (Kohmoto, Kadanoff, and Tang, 1983; Ostlund *et al.*, 1983; Lu, Odagaki, and Birman, 1986; Luck and Petritis, 1986; Nori and Rodriguez, 1986; Ashraff and Stinchcombe, 1989). The trace map equation is the same as in the electron problem, namely, Eq. (25), and the same kind of analysis applies. The spectrum of energies E has a Cantor-set structure, as seen in Fig. 40 [from Luck and Petritis (1986)], which shows the IDOS versus energy (these quantities are denoted in the figure by H and z).

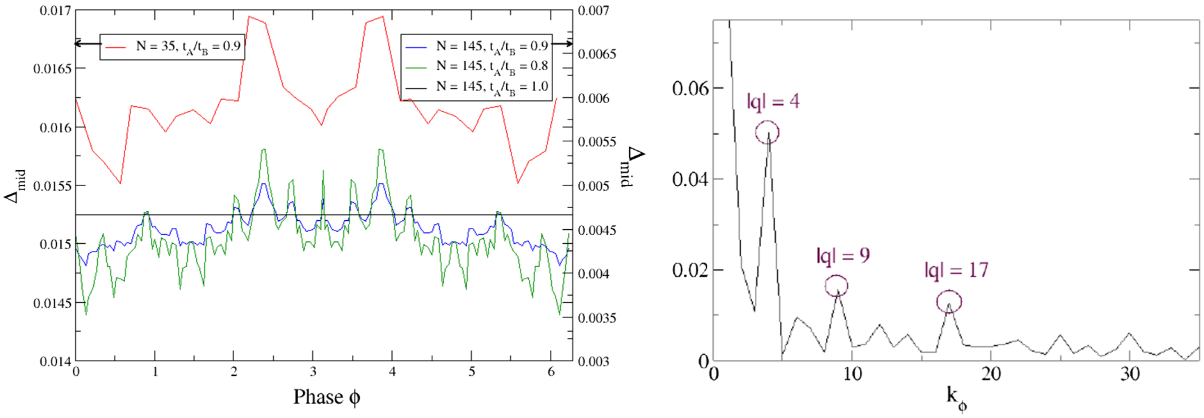

FIG. 39. Left panel: superconducting order parameter $\Delta(\mathrm{mid})$ at the midpoint of a Fibonacci chain vs the phason angle ϕ showing oscillations. Right panel: Fourier spectrum of the other plot, with the main periods showing the peaks at values equal to topological labels $\mathbf{q}$. From Rai, Haas, and Jagannathan, 2019.

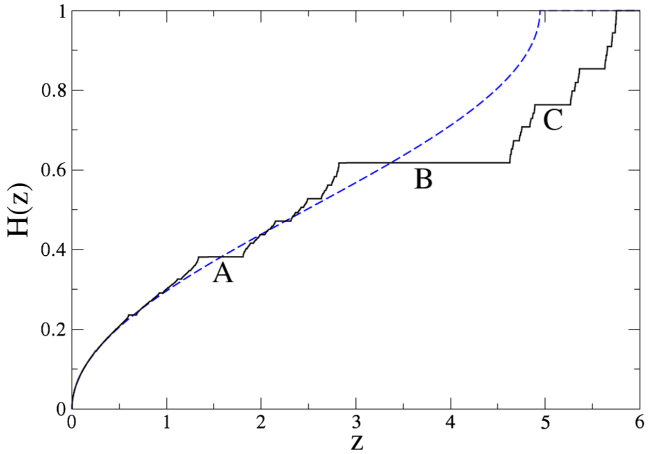

FIG. 40. Integrated phonon density of states (IDOS) $H(z)$ vs the eigenvalues z of the Laplacian operator on the Fibonacci chain for a coupling ratio 0.5. The three main plateaus are labeled A, B, and C. The dashed line represents the IDOS for the periodic system based on the average lattice, showing the similarity of the two curves for small z. From Luck and Petritis, 1986.

In contrast to the electronic case, for phonons the scaling is nonuniform as a function of energy, and gaps become small as E tends to zero. At the lowest frequencies, the integrated density of states, which is plotted in Fig. 40, looks almost indistinguishable from that of a periodic chain where the coupling is given by the appropriately defined average value of the two Fibonacci couplings. Like the periodic chain, the IDOS has a van Hove singularity, IDOS $\sim \sqrt{E}$, for small E. This behavior seems to indicate at first glance that the long wavelength Goldstone modes are robust with respect to the quasiperiodic modulation. However, Luck and Petritis (1986) presented a rigorous argument to show that the spectrum does not have any absolutely continuous component, even for a frequency tending to zero.

The gap labeling theorem is seen to hold, as expected, and the letters A, B, and C indicate three important gaps with gap labels given by the three smallest Fibonacci numbers (Luck and Petritis, 1986). The IDOS at these plateaus are given by $H_k = 1 - \omega^k$ for $k = 1, 2,$ and 3, where ω is the inverse of the golden mean. Luck and Petritis (1986) showed that the upper edge of the spectrum is described by a new six cycle $a \to -b \to -a \to b \to -a \to -b$. This observation was then used to show that, close to the upper edge, the quantity $1 - N(E)$, where N is the IDOS, has a power law modulated by log-periodic oscillations. Ashraff and Stinchcombe (1989) computed the dynamic structure factor for the Fibonacci chain. Quantum diffusion properties in this model have been studied (Kohmoto and Banavar, 1986; Lifshitz and Even-Dar Mandel, 2011) and found to share electronic properties of multifractal structure and log-periodic oscillations. For a more detailed discussion on phonon modes in Fibonacci quasicrystals, see Janssen, Chapuis, and de Boissieu (2018).

B. Mixed Fibonacci models

The term mixed models is used to denote a general member of the family of models in Eq. (12), where diagonal and off-diagonal quasiperiodic modulations are both present. These are relevant for experiments, as real systems can be expected to have both forms of quasiperiodicity.

Many of the techniques, including the powerful transfer matrix analysis, can be extended to mixed models. Maciá and Domínguez-Adame (1996, 1997) considered a mixed model in which the A and B sites have on-site energies of α or β following a Fibonacci sequence. The hopping amplitudes are assumed to have two possible values, $t_{AB} = t_{BA}$ or $t_{AA} = \gamma t_{AB}$. The initial step consists of defining the basic transfer matrices. Choosing, without loss of generality, units such that $\beta = -\alpha$ and $t_{AB} = 1$, one obtains four different transfer matrices in this model as follows:

$$X = \begin{bmatrix} (E+\alpha) & -1 \\ 1 & 0 \end{bmatrix}, \qquad Y = \begin{bmatrix} (E-\alpha)/\gamma & -1/\gamma \\ 1 & 0 \end{bmatrix},$$
$$W = \begin{bmatrix} (E-\alpha) & -\gamma \\ 1 & 0 \end{bmatrix}, \qquad Z = \begin{bmatrix} (E-\alpha) & -1 \\ 1 & 0 \end{bmatrix}. \qquad (76)$$

Maciá and Domínguez-Adame showed that after renormalization the global transfer matrix in this model has a structure identical to that of the Fibonacci sequence for the diagonal model [Eq. (22)]. This can be seen by defining blocks of sites via $T_A = ZYX$ and $T_B = WX$. They showed that in finite chains the energies of certain transparent states, i.e., with transmission coefficients of unity, are of the form

$$E(k) = \pm\sqrt{\alpha^2 + 4\cos^2(k\pi/N)}, \qquad (77)$$

where $|\alpha| \leq 2$ and k is an integer such that $N\tau = k\pi$, with $k = 0, 1, \ldots$. The states with energies $E(k)$ were confirmed as being extended states via a multifractal analysis.

For this set of models one can determine the resonance energy E_* (for which the two elementary transfer matrices of the chain commute) as a function of the parameters. Figure 41, adapted from Maciá (2017), shows the transmission coefficient $T_N(E_*)$ plotted as a function of resonance energy E_* versus the hopping amplitude γ with fixed diagonal term

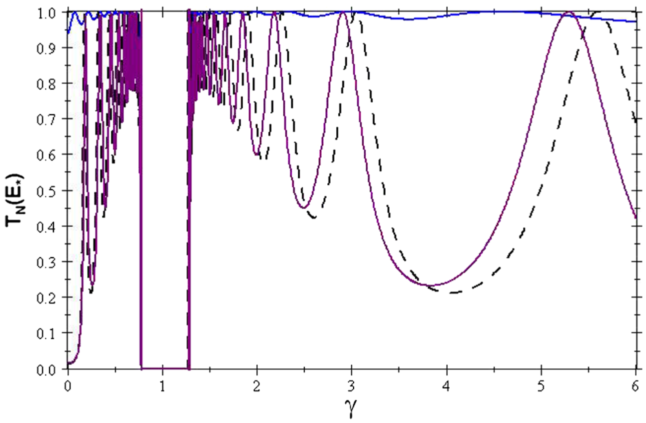

FIG. 41. Transmission coefficients at resonance energies E_* plotted vs γ (see the text for definitions) for several mixed models. The Fibonacci case is shown as a dashed line. The purple and blue curves represent the silver mean and period-doubling models, respectively. Adapted from Maciá, 2017.

strength 1/2 (both in units of t_{AB}) for three different models. The dashed line represents results for the Fibonacci model for $N = 41$ atoms, while the blue and purple lines correspond to silver mean quasicrystal and the period-doubling cases, respectively. One sees that transparent states occur throughout the spectrum.

Sire and Mosseri (1990) investigated a model for approximant chains in which the hopping takes one of two values (t_A or t_B) depending on the Fibonacci sequence. The on-site potentials whose values depend on the nature of bonds to the left and right were taken to be $V_{AA} = -\lambda/2$ and $V_{AB} = V_{AB} = \lambda/2$. The model thus has two parameters λ and ρ. By considering nth generation approximant chains, Sire and Mosseri showed that there are gap closings and quasiextended states for two different families of solutions. In particular, they showed that as $n \to \infty$ there are Bloch-type extended wave functions that can be described in terms of a wave vector $k \in (0, \pi)$. The energies of such states are distributed throughout the band, with the band edges corresponding to $k = 0$ and $k = \pi$. Similar conclusions as to the existence of such extended Bloch-type states were reached by Kumar and Ananthakrishna (1987) and Kumar (2017). Extended states with periodic envelopes may exist in mixed systems even in certain disordered cases, as reported by Huang and Gong (1998).

C. Interference and flux-dependent phenomena

Transmission properties of chains of Aharonov-Bohm rings of two different sizes, and connected in a Fibonacci sequence, have been studied (Chakrabarti, Römer, and Schreiber, 2003). The transport properties now become flux dependent. It was observed that transmission decreases as a power law in the number of rings and that there are resonant states for specific flux values. A RG analysis using the Landauer formalism and the trace map method shows that the transmission coefficient possesses a self-similar structure (Nomata and Horie, 2007).

X. OTHER QUASIPERIODIC CHAINS

Related models of particular interest include a class of aperiodic 1D chains that can be obtained by generalizing the substitution rules that we introduced in Sec. II.A. Higher-dimensional lattices are now described.

A. Aperiodic substitutional chains

Although we have focused on a single quasiperiodic system described by the golden mean τ, many of the methods used are generalizable to other irrational numbers. The nature of the irrational number (algebraic or not) is of primary importance to the geometric properties and, as a consequence, for the electronic properties as well. As we have discussed, quasicrystals are a special class of structures based on Pisot numbers. The so-called metallic means that are solutions of the equation $x^2 - nx - 1 = 0$ ($n = 1, 2, \ldots$) belong in this category. Of this series, the two best studied members are the gold ($n = 1$) and silver ($n = 2$) mean quasicrystals, with the latter also called the octonacci chain. These chains, which have inflation properties and electronic structures analogous to those of the Fibonacci chain, were reviewed by Yuan *et al.* (2000) and Thiem and Schreiber (2011, 2012, 2013). A study of the multifractal exponents for the central $E = 0$ state for metallic mean chains was done by Macé *et al.* (2017). Energy spectra of generalized Fibonacci-type quasilattices having self-similar as well as quasiperiodic structure were studied by Fu *et al.* (1997). A gap labeling theorem is shown to exist in these cases.

Some well-known aperiodic, but not quasiperiodic, systems that can be obtained using substitution rules are the Thue-Morse, period-doubling, and Rudin-Shapiro sequences. See Maciá (2005) for a discussion of their electronic properties.

B. Products of chains

The 1D chain can be used as the basis for extensions to arbitrary dimensions d. Taking $d = 2$, the direct product $C_n \times C_n$ of two Fibonacci approximants aligned along the x and y axes forms a 2D lattice of squares and rectangles (Lifshitz, 2002). As can be seen in Fig. 42(a), its connectivity is that of the square lattice. The energy spectrum and wave functions for tight-binding models on these direct product lattices have been studied. In the pure-hopping vertex model, electrons can hop along the two directions with amplitudes t_A and t_B. The Hamiltonian is separable into two independent Fibonacci chain problems. The energies are the sum of two 1D energies $E_{ij} = E_i + E_j$, and the corresponding wave functions given by the product $\psi_{ij}(x, y) = \psi_i(x)\psi_j(y)$, where E_i and ψ_i are solutions to the 1D problem. The properties of the spectrum depend on the value of ρ. The spectrum of the $d = 2$ product lattice is purely singular continuous for $\rho < \rho_1$, where $\rho_1 \approx 0.6$ in the product lattice. For $\rho > \rho_1$, the spectrum has a continuous part (Sire, 1989; Mandel and Lifshitz, 2008; Thiem and Schreiber, 2013).

The labyrinth model (Sire, Remi, and Sadoc, 1989), a 2D variant based on the direct product of chains [see Fig. 42(b)], also has properties derivable from the 1D solutions. The generalized dimensions describing multifractal properties of wave functions in d-dimensional product lattices were investigated by Yuan *et al.* (2000) and Thiem and Schreiber (2011). The exponents in d dimensions are simply proportional to the 1D exponents, $D_q^{\psi,d} = dD_q^{\psi,1}$. Dynamical exponents have

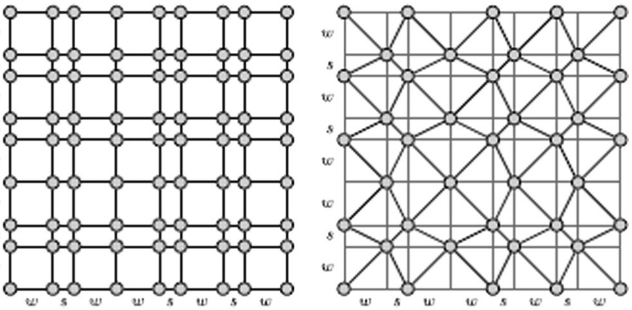

FIG. 42. Schemas of 2D product lattices hosting two different types of hopping models. Left panel: direct product Hamiltonian with t_A (long bonds) and t_B (short bonds). Right panel: labyrinth model (hopping along one of the diagonals of each plaquette). From Thiem and Schreiber, 2013.

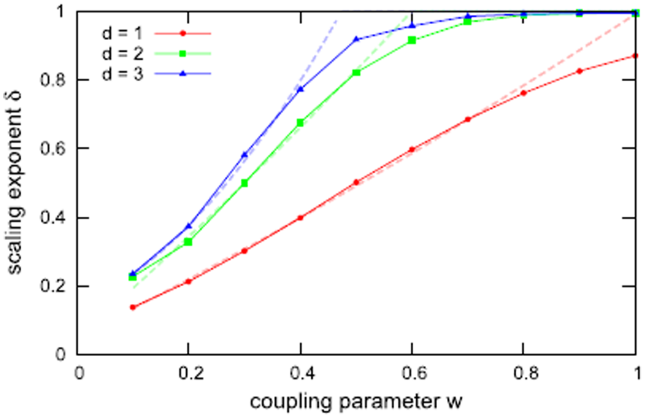

FIG. 43. Autocorrelation function exponent δ as a function of the strength of quasiperiodic modulation (the variable $w = t_A/t_B$ corresponds to ρ in our review) for product lattices of dimensions 1, 2, and 3. From Thiem and Schreiber, 2013.

been computed for these lattices (Zhong and Mosseri, 1995; Thiem and Schreiber, 2012). The return probability exponent shows a d dependence ($\gamma^d = d\gamma^{(1)}$). The diffusion exponent β is expected according to theory to be constant as the dimensionality d increases and this is indeed found numerically, as seen in Fig. 28. The autocorrelation function exponent δ depends on the dimensionality, and for higher d it increases faster as a function of the modulation strength parameter $w = t_A/t_B$, as seen in Fig. 43. A complete account of the electronic properties of such d-dimensional generalizations was given by Thiem and Schreiber (2013).

d-dimensional tilings.—The spatial connectivity of product lattice systems is simple in that they have an underlying average periodic structure: d-dimensional hypercubic lattices. The electronic properties of such product lattices are seen to be "inherited" from the parent chains. The situation is different for other quasiperiodic tilings. For 2D and 3D tilings such as the Penrose tiling, spectra and wave functions remain difficult to compute analytically, with the exception of the ground state (Macé *et al.*, 2017). As for the Fibonacci quasicrystal, nontrivial topological properties are to be expected in these higher-dimensional cases. The possibility of higher order topological insulators based on the Penrose and octagonal tilings was discussed by Fulga, Pikulin, and Loring (2016) and Chen *et al.* (2020).

XI. INTERACTIONS AND QUASIPERIODICITY

The topic of interacting quasiperiodic systems requires a separate review. This section is restricted to outlines of some of the main contributions, along with a nonexhaustive list of references.

The effects of quasiperiodic perturbations in interacting fermionic chains was investigated by Vidal, Mouhanna, and Giamarchi (1999, 2001) for continuum models using a renormalization group. Considering, in particular, the case of metallic mean chains, they found that there was a metal-insulator transition (Vidal, Mouhanna, and Giamarchi, 2001) for repulsive interactions. Hiramoto (1990) did a Hartree-Fock analysis to study the effect of the weak interaction U. The study showed that the singular continuous single-particle spectrum persists in the presence of interactions, in contrast to the critical Harper model, where the singular continuous behavior is destroyed by U.

In a study of the Hubbard model on a Fibonacci chain by weak-coupling renormalization group and density matrix renormalization group methods, Hida (2001) showed that, for the diagonal Fibonacci model, weak Coulomb repulsion is irrelevant in the sense of RG and the system will behave as a free Fibonacci chain. For strong Coulomb repulsion the system becomes a Mott insulator and, in the spin sector, can be modeled in terms of a uniform Heisenberg antiferromagnetic chain. For the off-diagonal case, he obtained a Mott insulator with a low energy sector that could be described in terms of a Fibonacci antiferromagnetic Heisenberg chain. Gupta, Sil, and Bhattacharyya (2005) studied the dc electrical conductivity for half filling, using Hartree-Fock mean field theory, to see the interplay of interactions and quasiperiodicity. They concluded that, while each of these factors taken individually tend to decrease the conductivity, there may be an enhancement of the conductivity due to the competition between them.

The evolution of multifractality in an interacting fermion chain was studied by Macé, Laflorencie, and Alet (2019). Contrary to naive expectations, they found that adding repulsive interactions did not lead to enhanced delocalization. Figure 44 shows the half chain von Neumann entropy plotted against time for different strengths of the quasiperiodic potential (controlled by a parameter h, with $h = 0$ the periodic case and $h = 1$ the strongly quasiperiodic chain). For a periodic chain (the black curve in Fig. 44), the entanglement entropy grows as a power law in the time $S(t) \sim t^{1/z}$. The exponent z increases as the strength of the quasiperiodicity h is increased. This further confirms that the free Fibonacci chain is intermediate between the Bloch-type delocalized state and an Anderson localized state from the point of view of its transport properties. One also sees log-periodic oscillations superposed on the power-law behavior that are especially visible in the strong quasiperiodic limit (yellow curve).

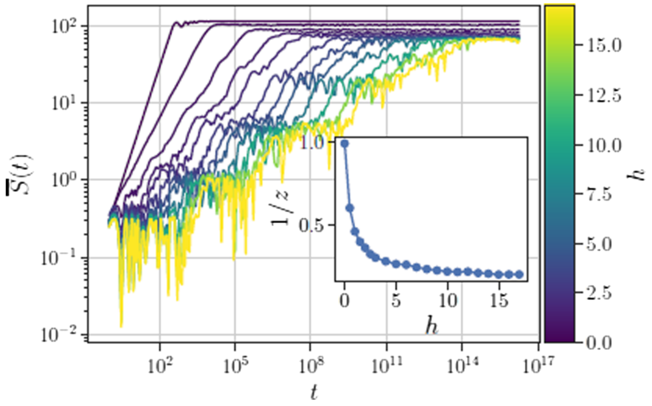

FIG. 44. Entanglement entropy as a function of time for different values of the strength of quasiperiodic modulation h (black curve, periodic chain; yellow (light gray) chain, strongly quasiperiodic chain). Inset: dependence of the power z on h. From Macé, Laflorencie, and Alet, 2019.

A. Heisenberg and XY chains

The properties of spin chains with Fibonacci couplings have been investigated using a number of methods. Hida analyzed the spin $1/2$ Heisenberg model using the density matrix renormalization group finding that quasiperiodic modulations are relevant in this case, and that the ground state is in a different universality class than that of the XY chain (or free particle) problem (Hida, 1999; Hermisson, 2000). The entanglement entropy S of aperiodic critical chains was studied by Iglói, Juhász, and Zimborás (2007). For these chains, the half chain entanglement increases as $S \sim (c/3)\ln_2 L + cst$, where L is the chain length and c is the central charge (0.5 in the periodic case). They found that for Fibonacci XY chains the quasiperiodic modulation is marginal in that the central charge c in this case is nonuniversal and depends on $\rho = J_A/J_B$ (the ratio of spin-spin couplings). For Fibonacci Heisenberg chains, the quasiperiodicity is strongly relevant and the prefactor is given by $c(0) \approx 0.8$.

B. Anomalous diffusion properties

Settino *et al.* (2020) studied dynamics in interacting aperiodic many body systems, including the FC. They showed that, for the on-site Fibonacci model, the singular continuous spectrum for the noninteracting problem remains and induces an anomalous dynamics. Lo Gullo *et al.* (2017) studied aperiodic discrete time quantum walk problems, which are relevant in quantum computing and which could be realized using optical fibers (Nguyen *et al.*, 2020). They computed the energy spectra and the spreading of an initially localized wave packet for different cases, finding in the case of Fibonacci and Thue-Morse chains that the system is superdiffusive, whereas for the Rudin-Shapiro chain, another substitutional chain, it is strongly subdiffusive. They proposed that the different dynamics are linked to the nature of the spectra in the two cases: singular continuous in the former, discrete in the latter. Density-density correlations at infinite temperature have been investigated using the dynamical quantum typicality approach (Chiaracane *et al.*, 2021). This allows one to study the evolution of dynamical properties of the Fibonacci model as interaction strength is ramped up, as well as the crossover to a MBL state.

C. Many body localization

The issue of many body localization due to quasiperiodic potentials was raised by Iyer *et al.* (2013) and Khemani, Sheng, and Huse (2017). They asked whether the MBL transitions are different in the presence of quasiperiodic potentials relative to random potentials, and if so in what ways. The MBL transition in the quasiperiodic AAH model, which can be experimentally realized in interacting boson and fermion cold atom systems, has been studied and shown to lead to a new type of "nonrandom" universality class (Khemani, Sheng, and Huse, 2017). It is interesting to ask whether there are any significant differences between many body localization in AAH and that in Fibonacci chains. Details of the transition were discussed by Macé, Laflorencie, and Alet (2019) and Varma and Žnidarič (2019).

XII. EXPERIMENTAL SYSTEMS

Fibonacci sequences occur naturally in 3D icosahedral quasicrystals and also in dodecagonal quasicrystals. These are structures that are based on the golden mean. Figure 45(a), which shows a STM image of copper adatoms deposited on an icosahedral AlPdMn quasicrystal (Ledieu *et al.*, 2004), provides a good illustration of this connection. As the height profile in Fig. 45(b) shows, the distances between columns represent a Fibonacci sequence. These rows of aperiodically spaced layers are coupled to the bulk, and the resulting Hamiltonians are likely to be fairly complicated. For experimental investigations of the 1D model, it is therefore useful to fabricate artificial systems in order to study the Fibonacci chain, and we now describe a few such systems.

The off-diagonal tight-binding Fibonacci model has been experimentally realized in a polaritonic gas in a quasi-1D cavity (Tanese *et al.*, 2014; Baboux *et al.*, 2017). Some of the theoretical predictions for the energies and the eigenmodes of this system were observed. The discrete scale invariance of the spectrum and the gap labeling theorem were thus

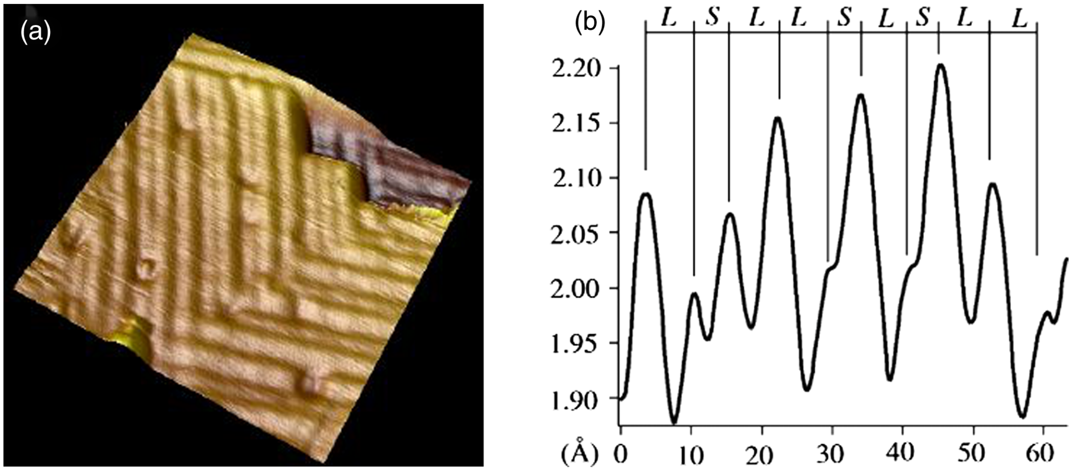

FIG. 45. (a) STM image of a 100×100 Å^2 zone of copper atoms deposited on the fivefold surface of i-AlPdMn. (b) Height profile between points marked with an X showing an alternating sequence of distances L (7.3 Å) and S (4.5 Å). From Ledieu *et al.*, 2004.

experimentally verified. The existence of gap states was checked and their spatial structure mapped out. Their topological winding numbers could be experimentally measured by varying the phason angle ϕ.

Optical waveguides fabricated using a femtosecond laser beam to inscribe quasiperiodic spatial modulation in a bulk glass were studied by Kraus *et al.* (2012). Injecting light into these waveguides allowed them to study propagating and localized modes, and to demonstrate the topologically protected edge modes predicted by theory. Topological pumping of photons was demonstrated by Verbin *et al.* (2015), who experimentally verified the topological equivalence between the Harper and Fibonacci models. Related subjects of recent investigations, which are outside the scope of this review, are higher order topological insulators using quasicrystals (Chen *et al.*, 2020) and topological quantum computation using Fibonacci anyon chains (Feiguin *et al.*, 2007; Chandran, Burnell, and Sondhi, 2020).

Merlin *et al.* (1985) and Bajema and Merlin (1987) fabricated semiconductor superlattices following a Fibonacci sequence and studied their properties using Raman spectroscopy. The samples were composed of two types of films: 27-nm-thick layers of GaAs and 43-nm-thick layers of GaAlAs (such that the ratio of thicknesses was close to the golden mean). These layers were piled on top of each other in a quasiperiodic sequence along the z direction. The Raman frequency shifts were compared for periodic and quasiperiodic structures. In addition to the acoustic phonons in this system, plasmon-polariton modes were argued to play an important role by Albuquerque and Cottam (2003), where their Raman cross sections for the samples were discussed. Hawrylak, Eliasson, and Quinn (1987) computed the plasmon spectrum for such superlattices, described its scaling properties, and explicitly computed the $f(\alpha)$ spectrum. For a wide-ranging discussion of photonic and phononic heterostructures, see the review by Steurer and Sutter-Widmer (2007).

A variety of photonic structures can be obtained by coupling single mode waveguides to form lattices through dynamical coupling or by using nonlinearities. It can be useful to consider these in terms of effective models in a higher-dimensional "synthetic space" in which the external parameters play the role of extra dimensions. These systems offer, in particular, a means to investigate the topological properties of the Su-Schreiffer-Heeger and AAH models (Yuan *et al.*, 2018) and leave open the possibility of extensions including the Fibonacci chain.

Metamaterials in the nanoscale also provide a wide array of possibilities for aperiodic structures. Optical transmission spectra of photonic band-gap Fibonacci quasiperiodic nanostructures composed of both positive (SiO_2) and negative refractive index materials were discussed by de Medeiros, Albuquerque, and Vasconselos (2007). In another direction, there are possibilities to make quasiperiodic sequences in 1D biomaterial (DNA-based) systems and study the consequences for transport (Albuquerque *et al.*, 2005).

Magnetic multilayers composed of Fe/Cr layers and studied by the magneto-optic Kerr effect and ferromagnetic resonance should display self-similar magnetization versus curves and interesting thermodynamic signatures (Bezerra, Albuquerque, and Cottam, 2001). Another promising system is composed of epitaxially grown layers of Fe and Au using ultrahigh-vacuum vapor deposition (Suwa *et al.*, 2017), which were theoretically predicted to have anomalous magnetoresistance (Machado *et al.*, 2012).

Fibonacci nanowire arrays were studied recently by Lisiecki *et al.* (2019), who discussed their magnonic properties and possible applications.

Quantum dots can be used to make artificial crystals and quasicrystals (Kouwenhoven *et al.*, 1990). They have already been used to study magnetotransport in a periodic crystal. It may therefore be possible to study transport in artificial Fibonacci chains made with quantum dots.

On a macroscopic length scale, microwave propagation in dielectric resonators has been used with success to simulate the tight-binding model for graphene (Bellec *et al.*, 2013). Preliminary work (Piéchon and Mortessagne, 2021) has shown that this may provide an extremely versatile system in which to study electronic properties of Fibonacci chains, including the effects of various forms of disorder or interactions.

Cold atoms in optical potentials constitute a particularly fertile ground to realize quasiperiodic models and study their properties under controlled conditions. A number of recent theoretical studies have thus looked at generalizations of the tight-binding models that are relevant to cold atom experiments. The discrete-valued Fibonacci potential is more difficult to realize experimentally than that in the Harper model, which can be realized by applying an incommensurate laser potential (Fallani *et al.*, 2007; Lye *et al.*, 2007). Recently, however, Singh *et al.* (2015) proposed a means of realizing generalized Fibonacci models on chains based on the cut-and-project method in a 2D optical lattice. If realized, this would provide opportunities to experimentally study multifractal states and probe the multiscale dynamics in the Fibonacci quasicrystal. An interesting direction discussed by Sagi and Nussinov (2016) concerns emergent quasiperiodic structures in interacting systems. They showed that fractional quantum Hall systems for irrational filling fractions can result in quasiperiodic electronic configurations that include, in one dimension, the case of an emergent Fibonacci ordering. They argued that such emergent quasicrystals could be realized with ultracold Rydberg atoms on optical lattices. Such structures, although not expected to be stable under disorder or quantum or thermal fluctuations, could nevertheless persist on intermediate length scales in the form of "quasicrystalline puddles."

XIII. SUMMARY AND OUTLOOK

We have introduced some of the main concepts and techniques relevant to 1D Fibonacci tight-binding Hamiltonians. This class of model is important from a fundamental viewpoint in its own right, and also as a starting point for understanding higher-dimensional quasicrystals. The topological characteristics of the 1D models arising from their "hidden dimension" can be generalized to higher-dimensional quasicrystals. Thus, just as the Fibonacci chain has topological properties inherited from a parent 2D system, certain 2D quasicrystals have been shown to have topological invariants corresponding to a 4D quantum Hall system (Kraus, Ringel, and Zilberberg, 2013) with associated edge modes that are symmetry protected.

Interpolating between the AAH and Fibonacci models offers us the possibility of realizing topological pumps, as in the optical waveguide systems of Verbin *et al.* (2015). More recently it was shown that polaritonic quasicrystals also allow this type of tunability (Goblot *et al.*, 2020). For these systems one can control localization-delocalization transitions for specific bands, suggesting the possibility of their use in selective bandpass filters.

In addition to these phenomena related to edge modes, recent work shows that bulk characteristics can also display the winding number (Rai *et al.*, 2021). When the chemical potential is chosen to lie within one of the spectral gaps, the charge density is an oscillating function and the number of oscillations is given by the gap label.

One of the distinctive characteristics of the quasicrystal is the existence of multifractalities as a function of the energy, the space coordinates, and the temporal correlations. We have discussed these properties, along with explicit calculations for specific examples. We have mentioned a few consequences of these multifractal states for physical properties: transport, disorder induced localization and delocalization, and the proximity effect. Critical states persist in higher-dimensional models. Note that there is an exact solution for ground states that is a 2D analog of the $E = 0$ solution on the FC that was discussed here (Kalugin and Katz, 2014; Macé *et al.*, 2017).

The Fibonacci family of models is interesting from the point of view of applications as well: in electronic devices or for their mechanical properties. Although we have focused here on electronic properties, but there are many interesting and closely related problems for electromagnetic wave modes in aperiodic media. The unique optical reflectivity properties of aperiodic multilayers suggest applications as perfect mirrors with omnidirectional reflectivity for all polarizations of incident light over a wide range of wavelengths (Axel and Peyrière, 2010), and more generally in nanodevices (Steurer and Sutter-Widmer, 2007; Maciá, 2012). The experimental possibilities of creating phononic systems suggest their use in thermal and acoustic shields or acoustic lenses, for example. In superconductors, the critical currents versus the field of quasiperiodically spaced pinned vortices were computed by Misko, Savel'ev, and Nori (2006) with a view to applications, and it was observed that for a 1D Fibonacci vortex array, the critical currents have a self-similar structure. More speculatively, one can conceive of applications on a larger scale suggested by some of the properties discussed here. The large number of spectral gaps generically present in this family of models suggests the possibility of dissipating ocean waves and even reflecting tsunamis on the shoreline using quasiperiodic arrays of scatterers. Seismic barriers against propagating Rayleigh waves (surface seismic modes) using, for example, quasiperiodic trenches are another interesting possibility.

The models discussed here provide a useful framework for understanding 1D quasiperiodic systems. Many questions still remain, however. The multifractal dynamical properties of quasiperiodic chains remain to be elucidated in more detail both theoretically and by experiment. The effects of interactions and their interplay with quasiperiodicity present an important problem requiring more investigation. The extension to higher-dimensional quasicrystals poses a major challenge. As far as understanding and controlling physical properties of quasicrystals is concerned, we have only scratched the surface.

ACKNOWLEDGMENTS

I gratefully acknowledge many valuable discussions over the years with Michel Duneau, Pavel Kalugin, Jean-Marc Luck, Nicolas Macé, and Frédéric Piéchon.

REFERENCES

Abanov, A. G., J. C. Talstra, and P. B. Wiegmann, 1998, Phys. Rev. Lett. **81**, 2112.

Abe, S., and H. Hiramoto, 1987, Phys. Rev. A **36**, 5349.

Albuquerque, E., and M. Cottam, 2003, Phys. Rep. **376**, 225.

Albuquerque, E. L., M. S. Vasconcelos, M. L. Lyra, and F. A. B. F. de Moura, 2005, Phys. Rev. E **71**, 021910.

Ashraff, J. A., and R. B. Stinchcombe, 1989, Phys. Rev. B **39**, 2670.

Aubry, S., and G. André, 1980, Ann. Isr. Phys. Soc. **3**, 18.

Axel, F., and J. Peyrière, 2010, J. Phys. A **44**, 035005.

Baake, M., and U. Grimm, 2013, *Aperiodic Order: A Mathematical Invitation* , Encyclopedia of Mathematics and Its Applications Vol. 1 (Cambridge University Press, Cambridge, England).

Baake, M., and U. Grimm, **2019**, J. Stat. Mech. 054003.

Baake, M., U. Grimm, and D. Joseph, 1993, Int. J. Mod. Phys. B **07**, 1527.

Baake, M., N. Priebe Frank, U. Grimm, and A. E. Robinson, 2019, Stud. Math. **247**, 109.

Baboux, F., E. Levy, A. Lemaître, C. Gómez, E. Galopin, L. Le Gratiet, I. Sagnes, A. Amo, J. Bloch, and E. Akkermans, 2017, Phys. Rev. B **95**, 161114.

Bajema, K., and R. Merlin, 1987, Phys. Rev. B **36**, 4555.

Barache, D., and J.-M. Luck, 1994, Phys. Rev. B **49**, 15004.

Beenakker, C. W. J., 1997, Rev. Mod. Phys. **69**, 731.

Bellec, M., U. Kuhl, G. Montambaux, and F. Mortessagne, 2013, Phys. Rev. B **88**, 115437.

Bellissard, J., A. Bovier, and J.-M. Ghez, 1992, Rev. Math. Phys. **04**, 1.

Bellissard, J., B. Iochum, E. Scoppola, and D. Testard, 1989, Commun. Math. Phys. **125**, 527.

Ben-Abraham, S. I., and A. Quandt, 2007, Acta Crystallogr. Sect. A **63**, 177.

Bezerra, C., E. Albuquerque, and M. Cottam, 2001, Physica (Amsterdam) **301A**, 341.

Chakrabarti, A., R. A. Römer, and M. Schreiber, 2003, Phys. Rev. B **68**, 195417.

Chandran, A., F. J. Burnell, and S. L. Sondhi, 2020, Phys. Rev. B **101**, 075104.

Chen, R., C.-Z. Chen, J.-H. Gao, B. Zhou, and D.-H. Xu, 2020, Phys. Rev. Lett. **124**, 036803.

Chiaracane, C., F. Pietracaprina, A. Purkayastha, and J. Goold, 2021, Phys. Rev. B **103**, 184205.

Damanik, D., 2006, Philos. Mag. **86**, 883.

Damanik, D., M. Embree, and A. Gorodetski, 2015, in *Mathematics of Aperiodic Order*, Progress in Mathematical Physics Vol. 309, edited by J. Kellendonk, D. Lenz, and J. Savinien (Birkhäuser, Boston), p. 307.

Damanik, D., A. Gorodetski, and W. Yessen, 2016, Invent. Math. **206**, 629.

Damanik, D., and S. Tcheremchantsev, 2007, J. Am. Math. Soc. **20**, 799.

Dareau, A., E. Levy, M. B. Aguilera, R. Bouganne, E. Akkermans, F. Gerbier, and J. Beugnon, 2017, Phys. Rev. Lett. **119**, 215304.

Das Sarma, S., and X. C. Xie, 1988, Phys. Rev. B **37**, 1097.

Delyon, F., Y.-E. Lévy, and B. Souillard, 1985, Phys. Rev. Lett. **55**, 618.

de Medeiros, F., E. Albuquerque, and M. Vasconselos, 2007, Surf. Sci. **601**, 4492.

Derrida, B., C. Itzykson, and J.-M. Luck, 1984, Commun. Math. Phys. **94**, 115.

Economou, E. N., and C. M. Soukoulis, 1981, Phys. Rev. Lett. **46**, 618.

Evangelou, S., 1987, J. Phys. C **20**, L295.

Evangelou, S., and D. Katsanos, 1993, J. Phys. A **26**, L1243.

Fallani, L., J. E. Lye, V. Guarrera, C. Fort, and M. Inguscio, 2007, Phys. Rev. Lett. **98**, 130404.

Feiguin, A., S. Trebst, A. W. W. Ludwig, M. Troyer, A. Kitaev, Z. Wang, and M. H. Freedman, 2007, Phys. Rev. Lett. **98**, 160409.

Fu, X., Y. Liu, P. Zhou, and W. Sritrakool, 1997, Phys. Rev. B **55**, 2882.

Fujiwara, T., M. Kohmoto, and T. Tokihiro, 1989, Phys. Rev. B **40**, 7413.

Fulga, I. C., D. I. Pikulin, and T. A. Loring, 2016, Phys. Rev. Lett. **116**, 257002.

Ganeshan, S., J. H. Pixley, and S. Das Sarma, 2015, Phys. Rev. Lett. **114**, 146601.

Gluzman, S., and D. Sornette, 2002, Phys. Rev. E **65**, 036142.

Goblot, V., *et al.*, 2020, Nat. Phys. **16**, 832.

Godrèche, C., 1990, in *Number Theory and Physics*, edited by J.-M. Luck, P. Moussa, and M. Waldschmidt (Springer-Verlag, Heidelberg), p. 86.

Godrèche, C., and J.-M. Luck, 1992, Phys. Rev. B **45**, 176.

Gordon, A. Y., S. Jitomirskaya, Y. Last, and B. Simon, 1997, Acta Math. **178**, 169.

Grimm, U., and M. Schreiber, 2003, in *Quasicrystals: Structure and Physical Properties*, edited by H. Trebin (Springer, Heidelberg).

Guarneri, I., 1993, Europhys. Lett. **21**, 729.

Gupta, S., S. Sil, and B. Bhattacharyya, 2005, Physica (Amsterdam) **355B**, 299.

Halsey, T., M. Jensen, L. Kadanoff, I. Procaccia, and B. I. Shraiman, 1986, Phys. Rev. A **33**, 1141.

Harper, P., 1955, Proc. Phys. Soc. London Sect. A **68**, 874.

Hawrylak, P., G. Eliasson, and J. J. Quinn, 1987, Phys. Rev. B **36**, 6501.

Hermisson, J., 2000, J. Phys. A **33**, 57.

Hida, K., 1999, J. Phys. Soc. Jpn. **68**, 3177.

Hida, K., 2001, Phys. Rev. Lett. **86**, 1331.

Hiramoto, H., 1990, J. Phys. Soc. Jpn. **59**, 811.

Hiramoto, H., and M. Kohmoto, 1989, Phys. Rev. B **40**, 8225.

Hiramoto, H., and M. Kohmoto, 1992, Int. J. Mod. Phys. B **06**, 281.

Huang, D., and D. Huang, 2004, Phys. Rev. B **70**, 205124.

Huang, H., and F. Liu, 2018, Phys. Rev. Lett. **121**, 126401.

Huang, H., and F. Liu, 2019, Phys. Rev. B **100**, 085119.

Huang, X., and C. Gong, 1998, Phys. Rev. B **58**, 739.

Iglói, F., R. Juhász, and Z. Zimborás, 2007, Europhys. Lett. **79**, 37001.

International Union of Crystallography, 1992, Acta Crystallogr. Sect. A **48**, 928.

Inui, M., S. A. Trugman, and E. Abrahams, 1994, Phys. Rev. B **49**, 3190.

Iochum, B., and D. Testard, 1991, J. Stat. Phys. **65**, 715.

Iyer, S., V. Oganesyan, G. Refael, and D. A. Huse, 2013, Phys. Rev. B **87**, 134202.

Jagannathan, A., P. Jeena, and M. Tarzia, 2019, Phys. Rev. B **99**, 054203.

Jagannathan, A., and M. Tarzia, 2020, Eur. Phys. J. B **93**, 46.

Janssen, T., G. Chapuis, and M. de Boissieu, 2018, *Aperiodic Crystals* (Oxford University Press, New York), Chap. 4.

Kalugin, P., and A. Katz, 2014, J. Phys. A **47**, 315206.

Kalugin, P. A., A. Yu. Kitaev, and L. S. Levitov, 1986, Zh. Eksp. Teor. Fiz. **91**, 692 [Sov. Phys. JETP **64**, 410 (1986)].

Ketzmerick, R., K. Kruse, S. Kraut, and T. Geisel, 1997, Phys. Rev. Lett. **79**, 1959.

Ketzmerick, R., G. Petschel, and T. Geisel, 1992, Phys. Rev. Lett. **69**, 695.

Khemani, V., D. N. Sheng, and D. A. Huse, 2017, Phys. Rev. Lett. **119**, 075702.

Kohmoto, M., and J. Banavar, 1986, Phys. Rev. B **34**, 563.

Kohmoto, M., L. P. Kadanoff, and C. Tang, 1983, Phys. Rev. Lett. **50**, 1870.

Kohmoto, M., and Y. Oono, 1984, Phys. Lett. **102A**, 145.

Kohmoto, M., B. Sutherland, and C. Tang, 1987, Phys. Rev. B **35**, 1020.

Kohn, W., 1964, Phys. Rev. **133**, A171.

Kouwenhoven, L. P., F. W. J. Hekking, B. J. van Wees, C. J. P. M. Harmans, C. E. Timmering, and C. T. Foxon, 1990, Phys. Rev. Lett. **65**, 361.

Kraus, Y. E., Y. Lahini, Z. Ringel, M. Verbin, and O. Zilberberg, 2012, Phys. Rev. Lett. **109**, 106402.

Kraus, Y. E., Z. Ringel, and O. Zilberberg, 2013, Phys. Rev. Lett. **111**, 226401.

Kraus, Y. E., and O. Zilberberg, 2012, Phys. Rev. Lett. **109**, 116404.

Kumar, V., 2017, J. Phys. Conf. Ser. **809**, 012023.

Kumar, V., and G. Ananthakrishna, 1987, Phys. Rev. Lett. **59**, 1476.

Ledieu, J., J. T. Hoeft, D. E. Reid, J. A. Smerdon, R. D. Diehl, T. A. Lograsso, A. R. Ross, and R. McGrath, 2004, Phys. Rev. Lett. **92**, 135507.

Levitov, L., 1989, J. Phys. (Paris) **50**, 707.

Lifshitz, R., 2002, J. Alloys Compd. **342**, 186.

Lifshitz, R., and S. Even-Dar Mandel, 2011, Philos. Mag. **91**, 2792.

Lisiecki, F., *et al.*, 2019, Phys. Rev. Applied **11**, 054061.

Liu, F., S. Ghosh, and Y. D. Chong, 2015, Phys. Rev. B **91**, 014108.

Liu, Y., and R. Riklund, 1987, Phys. Rev. B **35**, 6034.

Lo Gullo, N., C. V. Ambarish, T. Busch, L. Dell'Anna, and C. M. Chandrashekar, 2017, Phys. Rev. E **96**, 012111.

Lu, J. P., T. Odagaki, and J. L. Birman, 1986, Phys. Rev. B **33**, 4809.

Luck, J.-M., 1989, Phys. Rev. B **39**, 5834.

Luck, J.-M., 1993, Europhys. Lett. **24**, 359.

Luck, J.-M., and D. Petritis, 1986, J. Stat. Phys. **42**, 289.

Lye, J. E., L. Fallani, C. Fort, V. Guarrera, M. Modugno, D. S. Wiersma, and M. Inguscio, 2007, Phys. Rev. A **75**, 061603.

Macé, N., A. Jagannathan, P. Kalugin, R. Mosseri, and F. Piéchon, 2017, Phys. Rev. B **96**, 045138.

Macé, N., A. Jagannathan, and F. Piéchon, 2016, Phys. Rev. B **93**, 205153.

Macé, N., A. Jagannathan, and F. Piéchon, 2017, J. Phys. Conf. Ser. **809**, 012023.

Macé, N., N. Laflorencie, and F. Alet, 2019, SciPost Phys. **6**, 050.

Machado, L. D., C. G. Bezerra, M. A. Correa, C. Chesman, J. E. Pearson, and A. Hoffmann, 2012, Phys. Rev. B **85**, 224416.

Maciá, E., 2005, Rep. Prog. Phys. **69**, 397.

Maciá, E., 2012, Rep. Prog. Phys. **75**, 036502.

Maciá, E., 2017, Ann. Phys. (Berlin) **529**, 1700079.

Maciá, E., and F. Domínguez-Adame, 1996, Phys. Rev. Lett. **76**, 2957.

Maciá, E., and F. Domínguez-Adame, 1997, Phys. Rev. Lett. **79**, 5301.

Mandel, S. E.-D., and R. Lifshitz, 2008, Philos. Mag. **88**, 2261.

Mayou, D., C. Berger, F. Cyrot-Lackmann, T. Klein, and P. Lanco, 1993, Phys. Rev. Lett. **70**, 3915.

Merlin, R., K. Bajema, R. Clarke, F. Y. Juang, and P. K. Bhattacharya, 1985, Phys. Rev. Lett. **55**, 1768.

Misko, V. R., S. Savel'ev, and F. Nori, 2006, Phys. Rev. B **74**, 024522.

Nauenberg, M., 1975, J. Math. Phys. (N.Y.) **16**, 703.

Naumis, G. G., 1999, Phys. Rev. B **59**, 11315.

Naumis, G. G., and J. L. Aragón, 1996, Phys. Rev. B **54**, 15079.

Nguyen, D., T. Nguyen, R. Khrapko, D. A. Nolan, and N. F. Borrelli, 2020, Sci. Rep. **10**, 7156.

Niu, Q., and F. Nori, 1986, Phys. Rev. Lett. **57**, 2057.

Niu, Q., and F. Nori, 1990, Phys. Rev. B **42**, 10329.

Nomata, A., and S. Horie, 2007, Phys. Rev. B **75**, 115130.

Nori, F., and J. P. Rodriguez, 1986, Phys. Rev. B **34**, 2207.

Ostlund, S., and R. Pandit, 1984, Phys. Rev. B **29**, 1394.

Ostlund, S., R. Pandit, D. Rand, H. J. Schellnhuber, and E. D. Siggia, 1983, Phys. Rev. Lett. **50**, 1873.

Piéchon, F., 1996, Phys. Rev. Lett. **76**, 4372.

Piéchon, F., M. Benakli, and A. Jagannathan, 1995, Phys. Rev. Lett. **74**, 5248.

Piéchon, F., and F. Mortessagne, 2021 (private communication).

Rai, G., S. Haas, and A. Jagannathan, 2019, Phys. Rev. B **100**, 165121.

Rai, G., S. Haas, and A. Jagannathan, 2020, Phys. Rev. B **102**, 134211.

Rai, G., H. Schlömer, C. Matsumura, S. Haas, and A. Jagannathan, 2021, arXiv:2106.12654.

Röntgen, M., C. V. Morfonios, R. Wang, L. Dal Negro, and P. Schmelcher, 2019, Phys. Rev. B **99**, 214201.

Rüdinger, A., and F. Piéchon, 1998, J. Phys. A **31**, 155.

Rüdinger, A., and C. Sire, 1996, J. Phys. A **29**, 3537.

Sagi, E., and Z. Nussinov, 2016, Phys. Rev. B **94**, 035131.

Sánchez, V., L. A. Pérez, R. Oviedo-Roa, and C. Wang, 2001, Phys. Rev. B **64**, 174205.

Sánchez, V., and C. Wang, 2004, Phys. Rev. B **70**, 144207.

Settino, J., N. W. Talarico, F. Cosco, F. Plastina, S. Maniscalco, and N. Lo Gullo, 2020, Phys. Rev. B **101**, 144303.

Shechtman, D., I. Blech, D. Gratias, and J. W. Cahn, 1984, Phys. Rev. Lett. **53**, 1951.

Singh, K., K. Saha, S. A. Parameswaran, and D. M. Weld, 2015, Phys. Rev. A **92**, 063426.

Sire, C., 1989, Europhys. Lett. **10**, 483.

Sire, C., and R. Mosseri, 1989, J. Phys. (Paris) **50**, 3447.

Sire, C., and R. Mosseri, 1990, J. Phys. (Paris) **51**, 1569.

Sire, C., M. Remi, and J. Sadoc, 1989, J. Phys. (Paris) **50**, 3463.

Steurer, W., and D. Sutter-Widmer, 2007, J. Phys. D **40**, R229.

Sutherland, B., and M. Kohmoto, 1987, Phys. Rev. B **36**, 5877.

Süto, A., 1989, J. Stat. Phys. **56**, 525.

Suwa, T., S. Tomita, N. Hosoito, and H. Yanagi, 2017, Materials **10**, 1209.

Tanese, D., E. Gurevich, F. Baboux, T. Jacquemin, A. Lemaître, E. Galopin, I. Sagnes, A. Amo, J. Bloch, and E. Akkermans, 2014, Phys. Rev. Lett. **112**, 146404.

Tang, C., and M. Kohmoto, 1986, Phys. Rev. B **34**, 2041.

Theodorou, G., and M. H. Cohen, 1976, Phys. Rev. B **13**, 4597.

Thiem, S., 2015, Philos. Mag. **95**, 1233.

Thiem, S., and M. Schreiber, 2011, Eur. Phys. J. B **83**, 415.

Thiem, S., and M. Schreiber, 2012, Phys. Rev. B **85**, 224205.

Thiem, S., and M. Schreiber, 2013, J. Phys. Condens. Matter **25**, 075503.

Thiem, S., M. Schreiber, and U. Grimm, 2009, Phys. Rev. B **80**, 214203.

Torquato, S., 2018, Phys. Rep. **745**, 1.

Varma, V. K., S. Pilati, and V. E. Kravtsov, 2016, Phys. Rev. B **94**, 214204.

Varma, V. K., and M. Žnidarič, 2019, Phys. Rev. B **100**, 085105.

Velhinho, M. T., and I. R. Pimentel, 2000, Phys. Rev. B **61**, 1043.

Verbin, M., O. Zilberberg, Y. E. Kraus, Y. Lahini, and Y. Silberberg, 2013, Phys. Rev. Lett. **110**, 076403.

Verbin, M., O. Zilberberg, Y. Lahini, Y. E. Kraus, and Y. Silberberg, 2015, Phys. Rev. B **91**, 064201.

Vidal, J., D. Mouhanna, and T. Giamarchi, 1999, Phys. Rev. Lett. **83**, 3908.

Vidal, J., D. Mouhanna, and T. Giamarchi, 2001, Phys. Rev. B **65**, 014201.

Yuan, H. Q., U. Grimm, P. Repetowicz, and M. Schreiber, 2000, Phys. Rev. B **62**, 15569.

Yuan, L., Q. Lin, M. Xiao, and S. Fan, 2018, Optica **5**, 1396.

Zheng, W. M., 1987, Phys. Rev. A **35**, 1467.

Zhong, J., J. Bellissard, and R. Mosseri, 1995, J. Phys. Condens. Matter **7**, 3507.

Zhong, J., and R. Mosseri, 1995, J. Phys. Condens. Matter **7**, 8383.